

**Studies on Plasma Etching Process of Low Dielectrics  
for Fine Pattern Profile Control with Less Damage**

**Hiroshi YAMAMOTO**

**Studies on Plasma Etching Process of Low Dielectrics  
for Fine Pattern Profile Control with Less Damage**

**Hiroshi YAMAMOTO**

2012

Nagoya University

Department of Electrical Engineering and Computer Science

## **Chapter 1 Introduction**

1.1 Scope for Future Scale Integrated Circuits .....	1
1.1.1 Multi-Layered Structure .....	3
1.1.2 Resistance-Capacitance (RC) Delay .....	4
1.2 Interlayer Film with Low Dielectric Constant .....	8
1.3 Plasma Processing for Low- $k$ Dielectrics .....	12
1.3.1 Fine Pattern Profile of Low- $k$ Organic Materials .....	13
1.3.2 Plasma Damage on Porous Low- $k$ Materials .....	15
1.3.3 Smart Plasma Etching Process .....	17
1.4 Purposes and Construction of This Thesis .....	20
1.5 References .....	21

## **Chapter 2 Plasma Diagnostic Techniques and Film Characterization Methods**

2.1 Introduction .....	25
2.2 Vacuum Ultra-Violet Absorption Spectroscopy (VUVAS) .....	26
2.2.1 Theory of Absorption Spectroscopy .....	26
2.2.2 Measurements of Absolute Densities of Atomic H and N Radicals with Micro-discharge Hollow Cathode Lamp .....	29
2.3 Optical Emission Spectroscopy (OES) .....	32
2.4 Microwave Interferometer .....	37
2.5 Spectroscopic Ellipsometry .....	39
2.6 Fourier Transform Infrared Spectroscopy (FTIR) .....	46
2.7 X-Ray Photoelectron Spectroscopy (XPS) .....	50
2.8 Substrate Temperature Measurement System .....	54

## Contents

2.9 Secondary Ion Mass Spectrometry (SIMS) .....	57
2.10 References .....	60

### **Chapter 3    Precise Control of Etched Feature Profile of Low-*k* Organic Films Based on Control of Radical Densities and Substrate Temperature**

3.1 Introduction .....	63
3.2 Experimental Details .....	65
3.3 Results and Discussion .....	68
3.3.1 Etch Rate and Electron Density .....	68
3.3.2 Densities of Radicals in H <sub>2</sub> /N <sub>2</sub> Plasmas .....	71
3.3.3 Substrate Temperatures .....	73
3.3.4 Etch Rates for Low- <i>k</i> Organic Film .....	75
3.3.5 Etched Feature Profile .....	78
3.3.6 Etch Process with a Temporal Control of Radical Density .....	81
3.3.7 X-ray Photoelectron Spectroscopy Analyses on Etched Surface .....	83
3.4 Conclusion .....	91
3.5 References .....	92

## **Chapter 4 Investigation of Effect of Remained Fluorocarbon Layer and Air Exposure after Plasma Exposure on Low- $k$ Porous SiOCH Film**

4.1 Introduction .....	95
4.2 Experimental Details .....	96
4.3 Results and Discussion .....	99
4.3.1 Ashing rate .....	99
4.3.2 Modification by Air Exposure after Plasma Exposure .....	100
4.3.3 Effect of Remained CF Layer on Porous SiOCH Films .....	103
4.3.4 Temperature Dependence .....	109
4.3.5 Plasma Diagnostics .....	111
4.4 Conclusion .....	113
4.5 References .....	114

## **Chapter 5 H<sub>2</sub>/N<sub>2</sub> Plasma Damage on Low- $k$ Porous SiOCH Film Evaluated by *In Situ* Film Characterization and Plasma Diagnostics**

5.1 Introduction .....	117
5.2 Experimental Details .....	118
5.3 Results and Discussion .....	122
5.3.1 Roles for Ions, Radicals, and Light Radiation Analyzed by <i>In Situ</i> Film Characterization .....	122
5.3.2 Roles for Ions, Radicals, and Light Radiation Analyzed by <i>Ex Situ</i> Film Characterization .....	144

## Contents

5.3.3 Modification of Si-O-Si Structure in Porous SiOCH films by Ions, Radicals, and Light radiation .....	147
5.3.4 H <sub>2</sub> /N <sub>2</sub> Plasma Damage Mechanism of Porous SiOCH Films.....	150
5.4 Conclusion .....	159
5.5 References .....	161

## **Chapter 6      Conclusions and Future Works**

6.1 Conclusion of Present Research .....	163
6.2 Scopes for Future Works .....	165
 <b>Acknowledgements</b> .....	 169
<b>List of Papers</b> .....	172

## **Chapter 1                      Introduction**

### **1.1 Trend in Future Scale Integrated Circuits**

The semiconductor industry has developed by the rapid pace of improvement of cost, speed, and power in its products for more than four decades. Most of improvements have been accomplished principally by the industry's ability to exponentially decrease the minimum feature sizes used to fabricate integrated circuits. The most frequently cited trend is in integration level, which is usually expressed as Moore's Law (that is, the number of components per chip doubles roughly every 24 months). The most significant trend is the decreasing cost-per-function, which has led to significant improvements in economic productivity and overall quality of life through proliferation of computers, communication, and other industrial and consumer electronics. All of these improvement trends, sometimes called "scaling" trends, have been enabled by large R&D investments. First dynamic random access memory (DRAM) developed in 1970 was 1 Kbit in capacity, 1 Gbit DRAM was developed in 1998. A microprocessor (MPU) developed in Intel Corporation in 1971 consisted of about 2,300 transistors, and was operating at 108 kHz of clock frequency. On the other hand, Pentium(R) 4 processor™ developed in 2001 consisted of 55 million transistors, and was operating at 2.2 GHz of clock frequency. Recently, Intel Corporation has commercialized the 45nm Intel® Core™ i7 Processor in 2009, formerly known as Nehalem. This is a complex system on a chip with multiple functional units and multiple interfaces, including four cores, transistors of 731 million, and 8MB of cache size and operating at frequency higher than 3.6 GHz [1].

Table 1.1 shows the interconnect technology requirement for MPU and DRAM, which International Technology Roadmap for Semiconductors (ITRS) showed [2]. The wafer diameter has become larger for enhancing the device yield and cost-effective

products. The density of interconnect in a chip has increased. For this purpose, the interconnecting technology is getting more complicated.

Table 1.1 Interconnect technology requirements

Year of Production	2010	2011	2012	2013	2014	2015	2016	2017	2018	2019
MPU/ASIC Metal 1 $\frac{1}{2}$ Pitch (nm)(contacted)	45	38	32	27	24	21	19	17	15	13
DRAM $\frac{1}{2}$ Pitch (nm)(contacted)	45	40	36	32	28	25	23	20	18	16
Wafer diameter	300	300	450	450	450	450	450	450	450	450
Total interconnect length (m/cm <sup>2</sup> )	2222	2643	3143	3737	4195	4709	5285	5933	6659	7475

In commercial way, almost all semiconductor electronic devices are made on inorganic materials (basically silicon). Recently, organic materials have been introduced to electronic devices such as mechanically flexible computers and displays [3-4]. The flexible electronic devices have begun to make significant inroads into the commercial world. Organic semiconductors on flexible substrates have been known [5]. But achieving electronic properties comparable to those on inorganic materials such as silicon or glass requires high-quality crystals [6], and these cannot easily be made in the necessary thin-film form by the vapor-deposition methods and etching techniques typically used in microelectronics fabrication. In other words, the advance in flexible electronics stems from the ability to deposit or etch films on a variety of low-cost substrates such as plastic or metal foils.



### 1.1.1 Multi-Layered Structure

The most common element of integrated circuit (IC) for MPU and memory in personal computers are the complementary metal-oxide-semiconductor (CMOS). A cross section of the basic structure of CMOS multilevel wiring is shown in Fig. 1.1 [7]. Traditional CMOSs have been based on aluminum (Al) conductor and silicon oxide ( $\text{SiO}_2$ ) dielectric as interlayer insulating film. The  $\text{SiO}_2$  layer is deposited by a chemical vapor deposition (CVD) process and the planarization of interlayer insulating film by chemical mechanical polishing (CMP) has accelerated miniaturization. Layered aluminum (Al) alloy films are deposited by sputtering and patterned by plasma etching. The tungsten (W) plug is formed by CVD followed by etchback or CMP process. During the IC manufacturing, the photolithography and plasma etching for via pattern and metal lead pattern, titanium nitride (TiN) conductor deposition, and photoresist strip are also performed. Plasmas are used for etching and film deposition in ULSI processes.

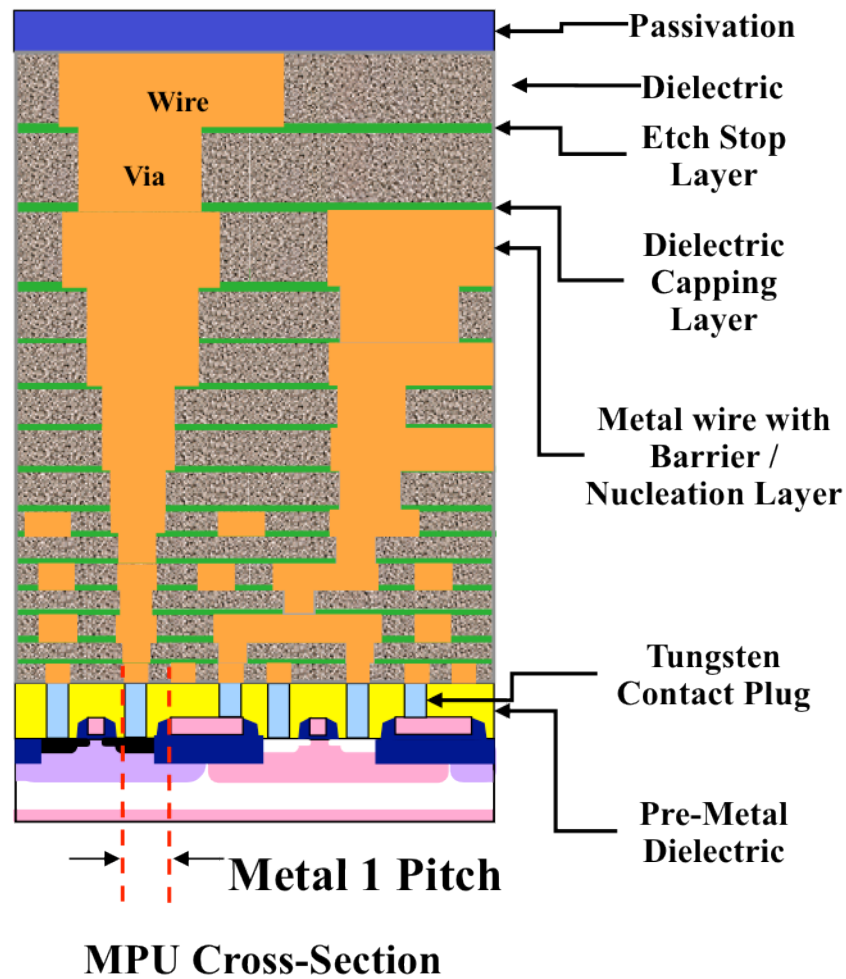


Fig. 1.1 Cross section of CMOS LSI multilevel wiring structure.

### 1.1.2 Resistance-Capacitance (RC) Delay

One of important problems for microelectronics today is unacceptable delay of electric signal propagation through metal interconnects by the resistance ( $R$ ) in the metal lines and the capacitance ( $C$ ) between adjacent metal lines. In advanced logic devices, the number of interlayer dielectrics has increased. This multilevel interconnection process requires several kilometers of metal in one chip. Figure 1.2

shows a total signal delay plotted against technology node [8]. The total signal delay is determined by the sum of gate and interconnect delays. The gate delay decreases monotonously due to the reduction of gate length. As the technology generation decreases down to 0.25  $\mu\text{m}$ , the delay component from the transistor gates dominates, and the total signal delay decreases monotonously. However, below 0.25  $\mu\text{m}$  generation, the interconnection delay dominates the total signal delay in ULSI, and total signal delay increases exponentially. The interconnect delay  $\tau$  is related to the product of wiring resistance  $R$  and parasitic capacitance  $C$  as

$$\tau \propto R \times C . \quad (1.1)$$

The resistance of wiring metals and the parasitic capacitance of interlayer dielectrics must be reduced to improve signal transmission rate. In order to reduce the wiring and capacitance, low electric resistivity metals and interlayer films with lower dielectric constants (low- $k$ ) are required. Aluminum (Al) and Al alloys have been used traditionally as interconnecting materials. Three elements exhibit lower resistivity than Al: gold (Au), silver (Ag) and copper (Cu). Among them, Au has the highest resistivity. Although Ag has the lowest resistivity, it has the poor electromigration resistance as well as an agglomeration problem. Cu offers good mechanical and electrical properties. The resistivity of Cu is about 40% less than that of Al. The self-diffusivity of Cu is also the smallest among the four elements, resulting in improved reliability. The viewpoint of cost also support Cu, Cu is cheaper than Au and Ag. Therefore, Cu is the most adapting material for deep submicron interconnects. Another of the effective methods to reduce wiring capacitance is the introduction of interlayer material with low- $k$ . The capacitance exists between interconnect wirings as shown in Fig. 1.3.

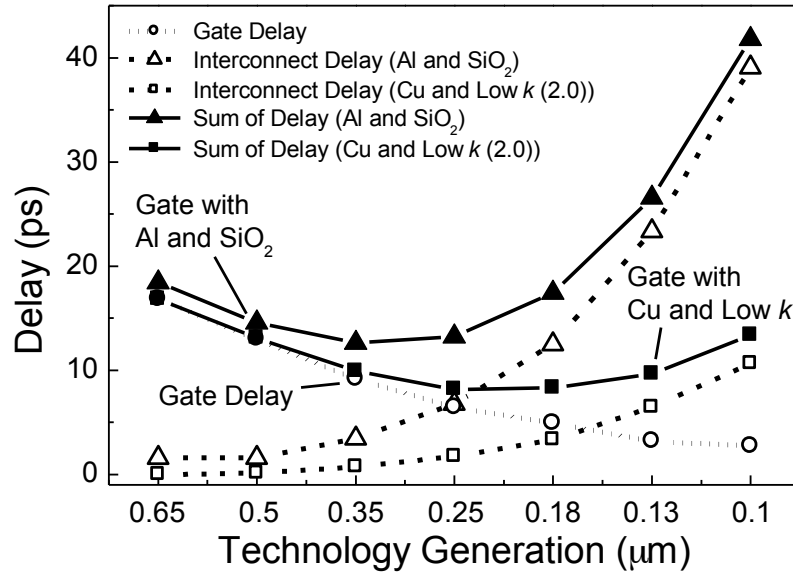
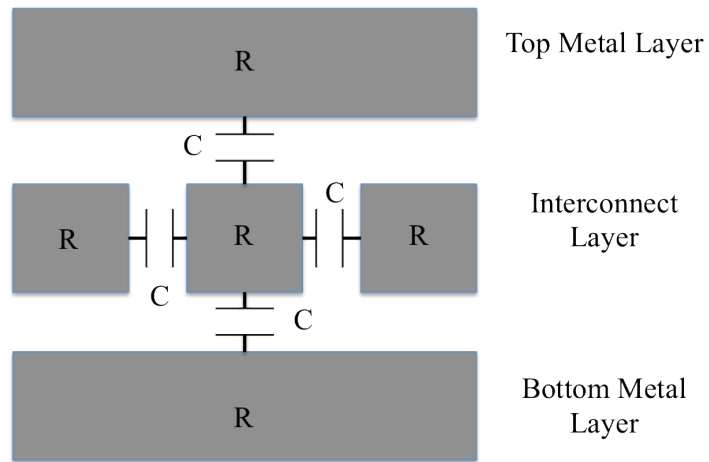


Fig. 1.2 Propagation delay plotted against technology node [7].



R: Resistance of wiring pattern

C: Capacitance between metal layers

Fig. 1.3 Model of wiring resistance and parasitic capacitance.

The signals in ULSI are transmitted with charging and discharging these capacitances. Therefore, the signal transmission rate becomes lower with the increase of  $C$  by the advance of miniaturization and integration. Electric capacitance  $C$  is given by

$$C = \epsilon_0 k_e \frac{S_C}{d}, \quad (1.2)$$

where  $S_C$  is the area of electrode,  $d$  is the distance between electrodes, and  $\epsilon_0$  and  $k$  are the permittivity of vacuum and the relative dielectric constant, respectively. Based on the scaling law,  $C$  decreases to  $1/k_s$ , since  $S_C$  and  $d$  decreases to  $1/k_s^2$  and  $1/k_s$ , respectively. However, the interconnection delay ( $R \times C$ ) as Eq. (1.1) does not change, since  $R$  ( $\approx \rho l / S_R$ ) increases to  $k_s$ . Where  $S_R$  and  $l$  are the area and length of wiring, respectively, and  $\rho$  is the electric conductivity. Therefore, in order to reduce parasitic capacitance, the reduction dielectric constant  $k_e$  by replacing interlayer dielectric material is effective.

The improvement of chip performance will be greater when Cu is combined with low- $k$  dielectrics. As shown in Fig. 1.2, it is possible to decrease the total signal delay to about quarter by adopting Cu/low- $k$  dielectric as compared with traditional Al/SiO<sub>2</sub> ( $k = 4.0$ ) interconnects at the 0.1  $\mu\text{m}$  generation node.

## 1.2 Interlayer Film with Low Dielectric Constant

The dielectric constants of interlayer are required lower than 4.0 since that of  $\text{SiO}_2$ , which is traditionally used, is 3.9 – 4.1. Transition timing and decreased maximum bulk  $k$  range are shown in Fig. 1.4 [2]. The dielectric constant of interlayer has decreased gradually lower than expected. ITRS expects this tendency keep going and the dielectric constant of 2.0 will be required in 2016. Any process change in semiconductor industry is difficult, however, choosing a new dielectric material has been an exercise in trying to find a low- $k$  dielectric film with electrical thermal and mechanical properties comparable to or better than those of  $\text{SiO}_2$ . Low- $k$  materials are required to have many properties. Several of the more important properties of a dielectric are good thermal stability, good adhesion, etch and strip resistance, commercial availability and low cost of production [9,10].

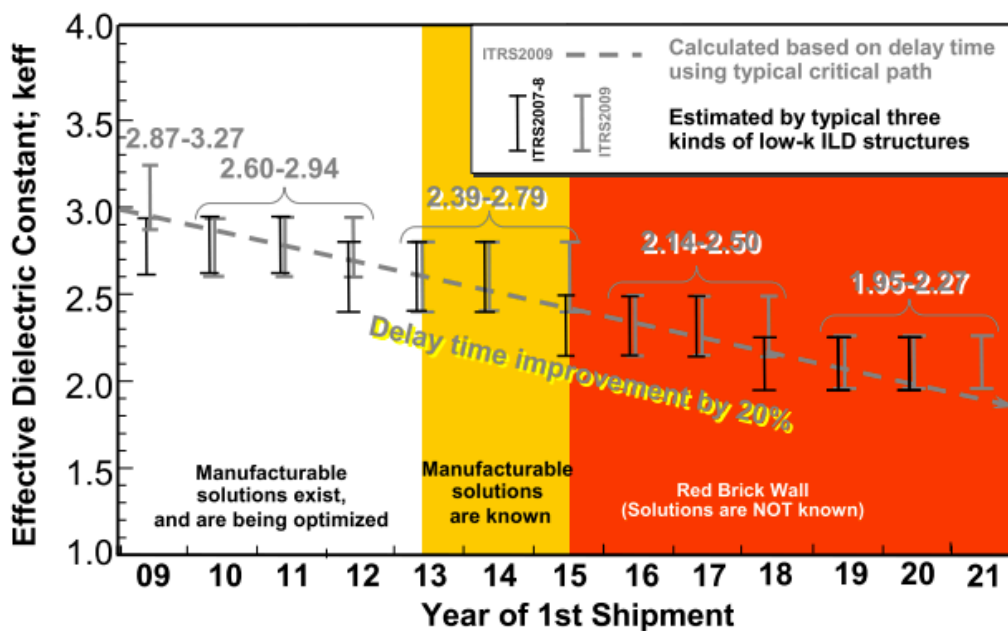


Fig. 1.4 Transition timing and decreased maximum bulk  $k$  range [2].

Table 1.2 Dielectric material candidates

	<b>Materials</b>	<b>Application</b>	<b><i>k</i> value</b>
Inorganic Material	SiO <sub>2</sub>	CVD	3.9 - 4.5
	Fluorosilicate Glass (FSG)	CVD	3.2 – 4.0
	Hydrogen Silsesquioxane (HSQ)	Spin-On	3.1 – 3.4
Hybrid Material	Black Diamond™	CVD	2.7 – 3.3
	SiOCH	CVD	2.6 – 2.9
	Methyl Silsesquioxane (MSQ)	Spin-On	2.6 – 2.8
Organic Material	Benzocyclobutene (BCB)	Spin-On	2.6 – 2.7
	B-staged Polymer (SiLK™)	Spin-On	2.6 – 2.7
	Poly (arylen ether) (FLARE™)	Spin-On	2.6 – 2.8
	Amorphous Fluorocarbon Film (a-C:F)	CVD	2.3

However, finding those with the required chemical, mechanical, electrical and thermal properties to be used in IC applications is more difficult. Table 1.2 provides a list of recognized dielectric material candidates. Low-*k* materials have been proposed through various kinds of processes such as plasma-enhanced chemical vapor deposition (PECVD) and spin-on-glass (SOG) techniques [11]. The dielectric properties of films are influenced by their chemical compositions and structures such as packing density and porosity. The candidates for low-*k* materials are classified into three groups: (1) inorganic films such as fluorinated silicon oxide (SiOF) [12-15] and porous silica, (2) hybrid materials composed of organic and inorganic components such as methylsilsesquioxane (MSQ) [16], SiOCH film [17], and (3) organic polymers such as FLARE™[18], SiLK™[9], benzocyclobutene [19], and amorphous fluorocarbon film

(a-C:F) [20,21]. Many kinds of insulating films with relatively low dielectric constant were proposed as an alternative to conventional interlayer insulating dielectric film of SiO<sub>2</sub>.

The etching of low- $k$  organic films can be performed without employing perfluorocarbon gases. Therefore, the adoption of low- $k$  organic films has the advantage of reducing the emission of perfluorocarbon gases of high global warming potential (GWP). For this reason, some low- $k$  organic films are used as interlayer insulation films at the present time. The development of high-performance interconnection technologies including the etching of low- $k$  films has also improved device performance.

Generally, inorganic materials have better thermal, mechanical stability and film adhesion during integration processing. However, these materials have higher dielectric constants and more moisture absorption than organic materials. The significant reduction of dielectric constant below 2.5 would be realized by introducing porous structure in the film such as porous SiOCH film [22-24]. Nevertheless, these materials have the poor mechanical strength and easily absorb moisture that increases the dielectric constant. Many problems which must be improved are left in order to introduce these materials into a semiconductor process. Hybrid materials have attracted much attention due to their higher thermal and mechanical stability than organic materials. Among these materials, SiLK™ and the porous SiOCH film are considered to be adaptive materials for the interlayer low- $k$  film. On top of that, these materials can be introduced to hybrid dual-damascene process, which is used to create the multi-level, high-density metal interconnections [25,26]. Fig. 1.3 shows schematic cross sections of the dual-damascene fabrication process for the hybrid interlayer dielectric structure. This process has following advantages: (a) etch stop layer can be removed, (b) less number of processes (around 30% less), (c) low cost. Sample structures of organic low- $k$  material and porous SiOCH film are shown in Fig. 1.4 (a) and (b).



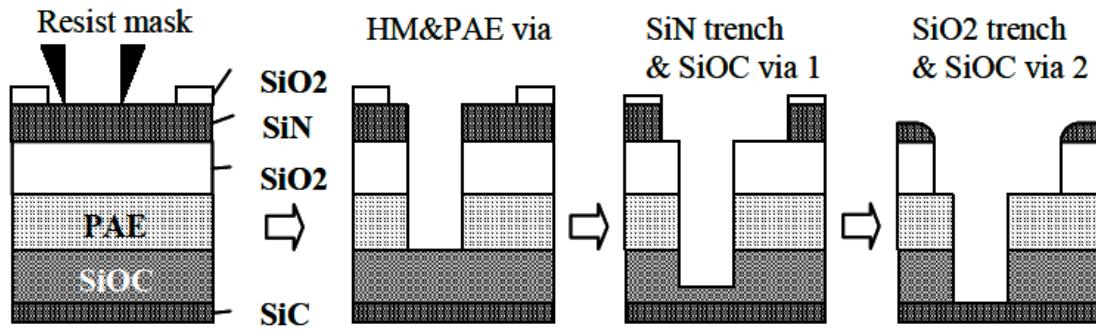
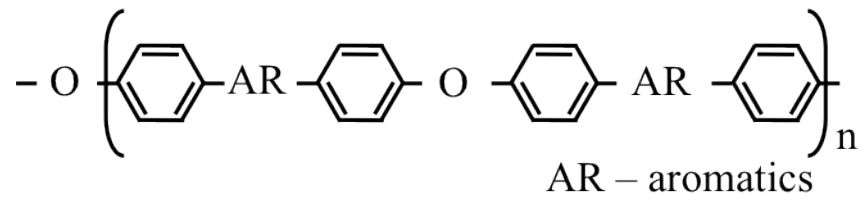


Fig. 1.3 Schematic diagram of hybrid dual-damascene fabrication process [21].

(a)



(b)

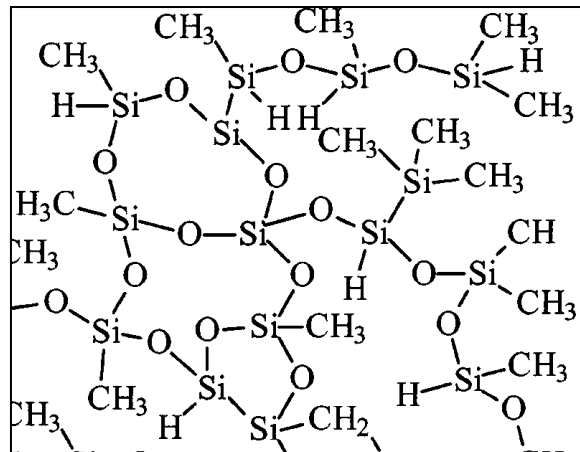


Fig. 1.4 Sample structure of (a) organic low- $k$  material (FLARE™) [15] and (b) hybrid low- $k$  material (porous SiOCH) [23].

### 1.3 Plasma Processing for Low- $k$ Dielectrics

Plasma processing such as etching and photoresist stripping (ashing) are essential components for semiconductor fabrication. The process can be chemically selective, removing one type of material while leaving other materials unaffected, and can be anisotropic, removing material at the bottom of a trench while leaving the same material on the sidewalls unaffected. These plasma processing systems are employed in industry for fabrication of integrated circuits and electronic devices. The primary goal of etch process is to precisely transfer the features on mask material into the exposed underlying material. The ash process should be achieved for removing photoresist mask without severe damage on the target material. These processes should be performed with the control of the sidewalls of the etched feature and the degree of undercutting. In addition to this capability, plasma processes require high selectivity to the mask and silicon substrate, controllability of shape of target material, dimension accuracy, high etching rate, uniformity, and causing low damage on the target material [27].

Plasma etching has basic requirements, the generation of radicals, ions and acceleration of the ions to target material. Once the ions reach the target, the ions can either physically or chemically remove atoms from the substrate [28,29]. The radicals diffuse thermally onto the wafer surface since they are electrically neutral. While the ions are accelerated perpendicularly to the wafer surface by a sheath field and then bombard the wafer surface. In common case of the plasma etching, the ion bombardment on the wafer is enhanced by applying an RF bias power to wafer as shown in Fig. 1.5. The radicals and ions reached the wafer react on the surface. The etching reactions add byproducts to the plasma. The byproducts are exhausted together with other products from the plasma by a pump system. These processes proceed by reactions between a wafer surface and gas species in the plasma [30]. Therefore, internal plasma parameters (electron density, electron temperature, substrate

temperature, radical and ion density etc.) are closely connected with the process performance [31,32].

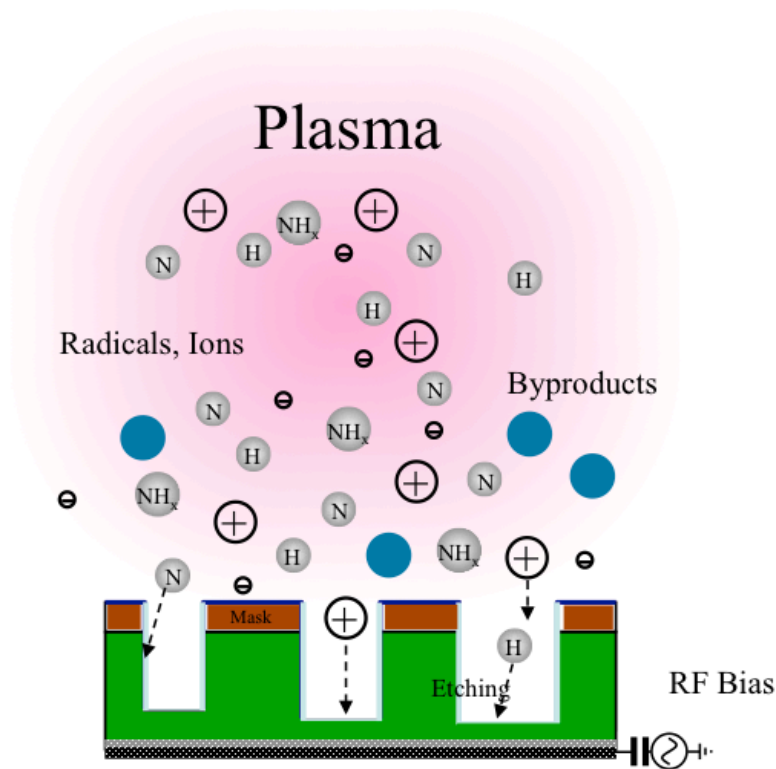


Fig. 1.5 Schematic diagram of etching process in case of low- $k$  film employing  $H_2/N_2$  gas chemistry.

### 1.3.1 Fine Pattern Profile of Low- $k$ Organic Materials

It is clear that a series of difficult process integration steps must be successfully completed, especially when low- $k$  materials are utilized. Difficulty in control of feature profile is noticeable in organic material etching process because organic materials have mechanical and chemical instability compared with inorganic or hybrid materials as shown in Fig. 1.6. Side etching, which causes bowing and microtrenching, occurs easily

on low- $k$  organic film [32-36]. On top of that, since ongoing trend in the semiconductor industry has been a need to fabricate integrated circuits with more transistors on a smaller area and acceptable error is less than 10%, a process with a few nm order precise etching of low- $k$  material will be required in near future.

In general, plasma processes are controlled by adjusting external parameters such as gas pressure, discharge power, and mixture ratio of gases. However, in these processes, it is difficult to obtain the reproducibility of etching characteristics by employing different types of etching equipment since plasma characteristics vary with mechanical variations, such as the type of plasma source and reactor size. The etching of low- $k$  organic films should be carried out with control of internal plasma parameters. If one applies the knowledge obtained about etching properties to the development of various apparatus, external parameters such as plasma excitation power input and gas pressure will be incoherent with other apparatus. Conversely, the information compiled with internal plasma parameters is extremely useful, and etching performance can be expressed uniquely and independently of the type of apparatus used. Thus, we focused on compiling etch properties with respect to internal parameters and investigated an etch mechanism for realizing highly precise control of the profiles of etch features in low- $k$  organic films. Precise control of etched feature profile of low- $k$  organic films will be discussed in Chapter 3.

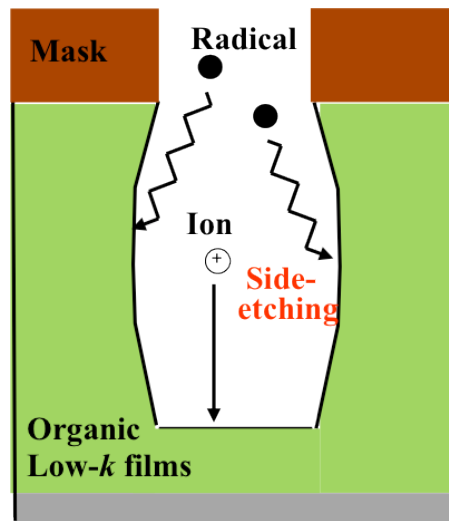


Fig. 1.6 Schematic diagram of side etching on low- $k$  organic film.

### 1.3.2 Plasma Damage on Porous Low- $k$ Materials

Porosity in low- $k$  materials brings in serious issues since the main integration difficulties with such materials are their sensitivity to plasma exposures leading to a change of the film structural properties as shown in Fig. 1.7. The device performance and reliability of the porous low- $k$  materials are degraded when they are exposed to plasma processes such as etching and ashing during microfabrication [37]. Since film modification is usually observed during an ash plasma process, a process with highly precise etching of porous low- $k$  material and low damage resist stripping process are required.  $O_2$  based ash plasmas tend to oxidize the porous SiOCH films converting the top layer into a hydrophilic  $SiO_2$ -like material generating a strong increase of the dielectric constant [38-41]. In order to reduce this type of damage, several research groups have investigated the damage generation mechanism and attempted to prevent degradation [42-48]. Posseme *et al.* have investigated effect of remote  $H_2/Ar$ ,  $NH_3$  plasmas and revealed that  $NxHy$ ,  $H$ , and  $N$  radicals react with SiOCH matrix leading to

the modification and increase of dielectric constant is mainly attributed to the moisture uptake [49]. On top of that, effect of light radiation in region of vacuum ultra-violet (VUV) and ultra-violet (UV) in plasma etching process have been pointed out [50-54].

However, the degradation mechanism of porous low- $k$  films induced by plasma processes has been investigated only by *ex situ* experiments. Inferences drawn from such experiments assume that surface modification caused by exposure to air after plasma processes is negligible compared with that caused by plasma exposure. However, we thought the effect of air exposure after plasma process should be investigated. On top of that, plasma species also should be considered to understand plasma damage mechanism, therefore, we investigated the plasma ashing damage mechanism on porous SiOCH films based on *in situ* film analysis and plasma diagnostics in Chapter 4 and 5.

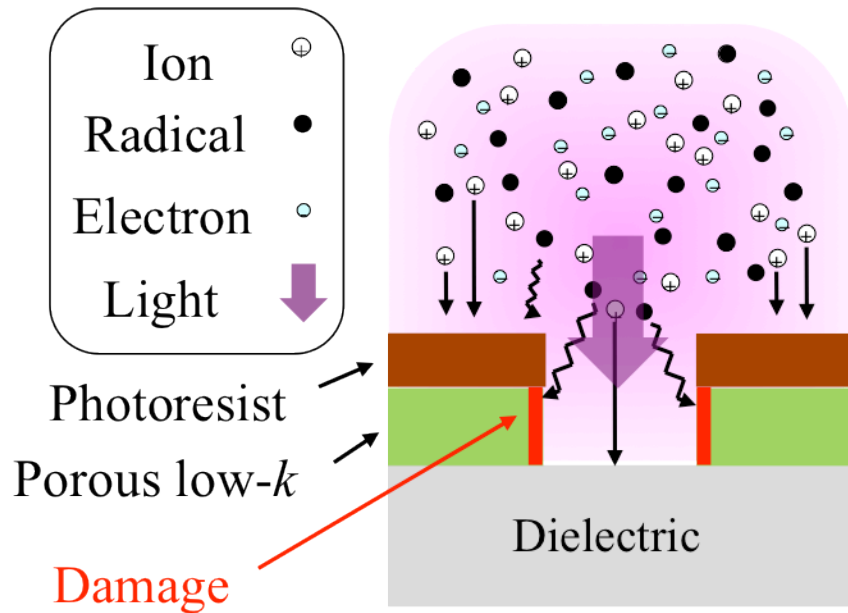


Fig. 1.7 Schematic diagram of plasma damage on porous low- $k$  film during ash process.

### 1.3.3 Smart Plasma Etching Process

In order to understand chemical reaction between plasma and target materials and realize highly precise etching, it is necessary to carry out the monitoring of the internal plasma parameters and *in situ* film characterization. We have constructed a smart plasma process system based on *in situ* film characterization and plasma diagnostics and substrate temperature measurement system as shown in Fig. 1.8. The system can control radical densities in a plasma and substrate temperature based on collected data. Plasma processing should be performed based on the internal plasma parameters. On top of that, information on etching properties defined by the internal plasma parameters is very useful and applicable to obtain high etching performance in various etching apparatus.

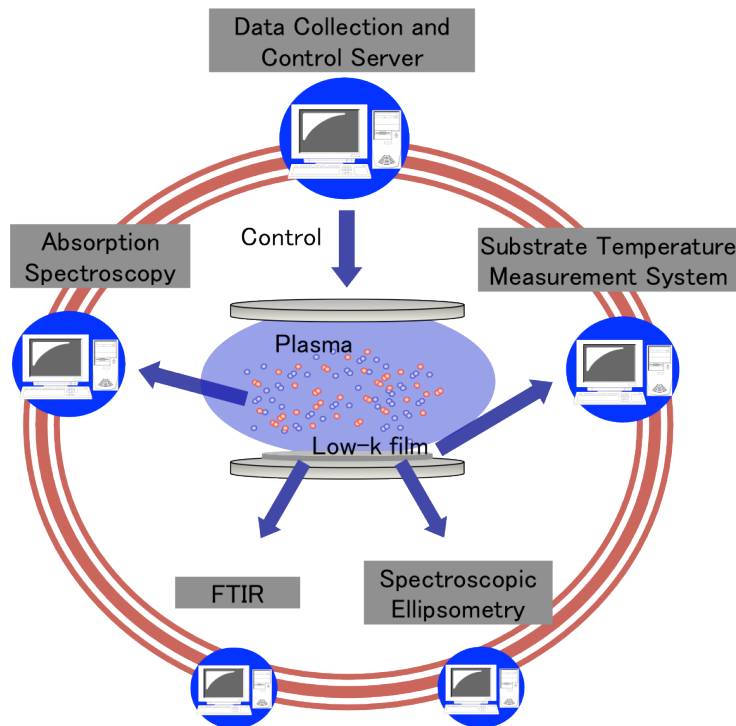


Fig. 1.8 Schematic diagram of smart etching system.

### 1.4 Purposes and Construction of This Thesis

The goal of this study is to understand plasma modification mechanism of the low- $k$  materials and to realize highly precise and damage less processing of the low- $k$  materials. In order to perform these processes, the measurement of hydrogen and nitrogen densities using vacuum ultra-violet absorption spectroscopy (VUVAS) technique was applied to diagnostic of process plasma. The highly precise etching of low- $k$  organic film was performed by controlling internal plasma parameter. Moreover, in order to clarify the etching mechanism of low- $k$  organic film, *in situ* film characterizations were performed. The composition of this thesis is as follows:

In Chapter 2, theories of plasma diagnostics such as VUVAS and microwave Interferometer were described. Theories of film characterization technique such as spectroscopic ellipsometry, X-ray photoelectron spectroscopy (XPS) and a Fourier transform infrared reflection absorption spectroscopy (FTIR-RAS) used as measurement methods of etched subsurface reactions were introduced.

In Chapter 3, a precise etching process for low- $k$  organic films by hydrogen and nitrogen mixture gases plasma was developed by control of densities of hydrogen and nitrogen radicals based on real-time measurement of Si substrate temperature. H and N radical densities were monitored nearby the sidewall of reactor by a vacuum ultraviolet absorption spectroscopy and the temperature was monitored by an optical fiber-type low-coherence interferometer. Based on results of surface analyses of X-ray photoelectron spectroscopy, etched profiles were effectively determined by the chemical component of protection layers on the sidewall of etched pattern that was influenced by the ratio of H/(H+N) and the substrate temperature. As the etching feature is evolved, the ratio of radical density needed to be controlled temporally to maintain vertical profiles according to the change of substrate temperature.

In Chapter 4, the effect of remained fluorocarbon layer and air exposure after



plasma exposure on porous low- $k$  SiOCH film were investigated. Refractive index, thickness in porous SiOCH film were investigated during plasma treatment and subsequent air exposure. On top of that, plasma analysis such as VUVAS was performed. The film characterization and plasma analysis revealed the plasma damage mechanism of porous low- $k$  SiOCH films.

In Chapter 5, the modification of porous low- $k$  SiOCH films by ashing plasma irradiation and subsequent exposure to air was investigated by *in situ* characterization. Porous blanket SiOCH film surfaces were treated by a  $H_2$  or  $H_2/N_2$  plasmas. The impact of ions, radicals, and vacuum ultraviolet radiation on the porous SiOCH films was investigated using *in situ* bulk analysis techniques such as spectroscopic ellipsometry and Fourier-transform infrared spectroscopy and *ex situ* film characterization techniques such as dynamic secondary ion mass spectrometry (dynamic SIMS) and X-ray photoelectron spectroscopy.

Finally, the results in the present study were summarized and future works was described in the Chapter 6.

## 1.5 References

- [1] R. Kumar and G. Hinton, “A Family of 45nm IA Processors,” ISSCC Dig. Tech. Papers, Paper 3.2, Feb. 2009.
- [2] Intern. Technol. Roadmap for Semicond. (Semicond. Indust. Associat., 2009).
- [3] A. Aviram, and M. Ratner, Chem. Phys. Lett. **29**, 277 (1974).
- [4] C. Joachim, J. Gimzewski, and A. Aviram, Nature **408**, 541 (2000).
- [5] C. K. Chiang, C. R. Fincher, Jr., Y. W. Park, A. J. Heeger, H. Shirakawa, E. J. Louis, S. C. Gau, and Alan G. MacDiarmid, Phys. Rev. Lett. **39**, 1098 (1977).
- [6] J. H. Schön, S. Berg, Ch. Kloc, and B. Batlogg, Science **287**, 1022 (2000).
- [7] R. H. Havemann, and J. A. Hutchby, Proceedings of the IEEE, **89**, 586 (2001).
- [8] M. Bohr and Y. A. Elmansy: IEEE Trans. Electron Devices **45**, 620 (1998).
- [9] M. R. Baklanov, S. Vanhaelemeersch, H. Bender, and K. Maex, J. Vac. Sci. Technol. B **17**, 372 (1999).
- [10] G. S. Oehrlein, T. E. F. M. Standaert, and P. J. Matsuo, in Solid State Technology; Vol. May 2000 (2000), p. 125.
- [11] C. H. Ting and T. E. Seidel: in Low Dielectric Constant Materials-Synthesis and Applications in Microelectronics, edited by T. M. Lu, S. P. Murarka, T.-S. Kuan, and C. H. Ting, Mater. Res. Soc. Proc. No. 381 (Materials Research Society, Pittsburgh, PA, 1995), pp. 3-17.
- [12] T. Homma, R. Yamaguchi, and Y. Murao: J. Electrochem. Soc., **140**, 687 (1993).
- [13] T. Usami, K. Shimokawa, and M. Yoshimaru: Jpn. J. Appl. Phys., **33**, 408 (1994).
- [14] J. C. Alonso, E. Pichardo, L. Rodríguez-Fernandez, C. Cheang-Wong, and A. Ortiz, J. Vac. Sci. Technol. A **19**, 507 (2001).
- [15] B. P. Gorman, R. A. Orzco-Teran, J. A. Roepsch, H. Dong, and D. W. Mueller, Appl. Phys. Lett. **79**, 4010 (2001).

- [16] A. T. Kohl, R. Mimna, R. Shick, L. Rhodes, Z. L. Wang, and P. A. Kohl: *Electrochem. Solid-State Lett.* **2**, 77 (1999).
- [17] Y. H. Kim, S. K. Lee, H. and J. Kim, *J. Vac. Sci. Technol. A* **18**, 1216 (2000).
- [18] K. S. Lau, E. Brouk, T. A. Chen, B.A. Korolev. P. E. Schilling, and H. W. Thompson: in *Proc. 14<sup>th</sup> Int. Conf. VLSI Multilevel Interconnection*. (1997) pp. 577.
- [19] S. A. Vitale, H. Chae, and H. H. Sawin, *J. Vac. Sci. Technol. A* **18**, 2770 (2000).
- [20] L. M. Han, R. B. Timmons, W. W. Lee, Y. Chen, and Z. Hu, *J. Appl. Phys.*, **84**, 439 (1998).
- [21] B. Cruden, K. Chu, K. Gleason, and H. Sawin, *J. Electrochem. Soc.* **146**, 4590 (1999).
- [22] E. V. Besien, M. Pantouvaki, L. Zhao, D. D. Roest, M. R. Baklanov, Z. Tőkei, and G. Beyer, *Microelectronic Engineering* 10-12 (2011).
- [23] S. M. Gates, D. Neumayer, M. H. Sherwood, A. Grill, X. Wang, and M. Sankarapandian, *Journal of Applied Physics* **101**, 094103 (2007).
- [24] A. Grill and D. Neumayer, *Journal of Applied Physics* **94**, 6697 (2003).
- [25] Wolf, *Silicon Processing for the VLSI Era*, (Lattice, Sunset Beach, CA, 2004 hybrid damas
- [26] R. Kanamura, Y. Ohoka M. Fukasawa, K. Tabuchi, K. Nagahata, S. Shibuki, M. Muramatsu, H. Miyajima, T. Usui, A. Kajita, H. Shibata, and S. Kadomura, 2003 *Symposium on VLSI Technology Digest of Technical Papers*, pp.107 (Kyoto, Japan, 2003).
- [27] M. A. Lieberman and A. J. Lichtenberg. “Principles of plasma discharges and materials processing”. (John Wiley & Sons, Inc., New York, 1994).
- [28] O. Joubert, G. S. Oehrlein and Y. Zhang: *J. Vac. Sci. Technol. A* **12**, 658 (1994).
- [29] O. Joubert, G. S. Oehrlein and Y. Zhang: *J. Vac. Sci. Technol. A* **12**, 665 (1994).
- [30] T. Namura, H. Okada, Y. Naitoh, Y. Todokoro and M. Inoue: *Jpn. J. Appl. Phys.*, **29**, 2251 (1990).

- [31] C. S. Moon, K. Takeda, M. Sekine, Y. Setsuhara, M. Shiratani, and M. Hori, J. Appl. Phys. **107**, 113310 (2010).
- [32] H. Nagai, S. Takashima, M. Hiramatsu, M. Hori, and T. Goto, J. Appl. Phys. **91** (2002) 2615.
- [33] M. Fukasawa, T. Hasegawa, S. Hirano, and S. Kadomura, in Proceedings of Symposium on Dry Process, Waseda University, Tokyo, Japan (1998) pp. 175.
- [34] M. Fukasawa, T. Tatsumi, T. Hasegawa, S. Hirano, K. Miyata, and S. Kadomura, in Proceedings of Symposium on Dry Process, Waseda University, Tokyo, Japan (1999) pp. 221.
- [35] Y. Morikawa, S. Yasunami, W. Chan, T. Hayashi, and T. Uchida, J. Vac. Sci. Technol. A **19** (2001) 1747.
- [36] H. Nagai, M. Hiramatsu, M. Hori, and T. Goto, J. Appl. Phys., **94**, 1362 (2003).
- [37] K. Yonekura, S. Sakamori, K. Goto, M. Matsuura, N. Fujiwara, and M. Yoneda, J. Vac. Sci. Technol. B **22**, 548 (2004).
- [38] D. Shamiryan, M. R. Baklanov, S. Vanhaelemeersch, and K. Maex, J. Vac. Sci. Technol. B **20**, 1923 (2002).
- [39] O. Louveau, C. Bourlot, A. Marfoure, I. Kalinovski, J. Su, G. H. Hills, and D. Louis, Microelectron. Eng. **73**, 351 (2004).
- [40] E. Ryan *et al.*, Mater. Res. Soc. Symp. Proc. 766 (2003).
- [41] G. Beyer, A. Satta, J. Schumacher, K. Maex, W. Besling, O. Kipela, H. Sprey, and G. Tempel, Microelectron. Eng. **64**, 233 (2002).
- [42] K. Maex, M. R. Baklanov, D. Shamiryan, F. Iacopi, S. H. Brongersma, and Z. S. Yanovitskaya, J. Appl. Phys. **93**, 8793 (2003).
- [43] H. Cui, R. J. Carter, D. L. Moore, H. G. Peng, D. W. Gidley, and P. A. Burke, J. Appl. Phys. **97**, 113302 (2005).
- [44] J. Bao, H. Shi, J. Liu, H. Huang, P. S. Ho, M. D. Goodner, M. Moinpour, and G. M. Kloster, J. Vac. Sci. Technol. B **26**, 219 (2008).

- [45] X. Hua, M. Kuo, G. S. Oehrlein, P. Lazzeri, E. Lacob, M. Andrlé, C. K. Inoki, T. S. Kuan, P. Jiang, and W. Wu, *J. Vac. Sci. Technol. B* **24**, 1238 (2006).
- [46] S. Uchida, S. Takashima, M. Hori, M. Fukasawa, K. Ohshima, K. Nagahata, and T. Tatsumi, *J. Appl. Phys.* **103**, 073303 (2008).
- [47] S. Xu, C. Qin, L. Diao, D. Gilbert, L. Hou, A. Wiesnoski, E. Busch, R. McGowan, B. White, and F. Weber, *J. Vac. Sci. Technol. B* **25**, 156 (2007).
- [48] M. A. Worsley, S. F. Bent, S. M. Gates, N. C. Fuller, W. Volksen, M. Steen, and T. Dalton, *J. Vac. Sci. Technol. B* **23**, 395 (2005).
- [49] N. Posseme, T. Chevolleau, T. David, M. Darnon, O. Louveau, and O. Joubert, *J. Vac. Sci. Technol. B* **25**, 1928 (2007).
- [50] B. Jinnai, T. Nozawa, and S. Samukawa, *J. Vac. Sci. Technol. B* **26**, 1926 (2008).
- [51] V. Danilov, H. E. Wagner, and J. Meichsner. *Plasma Process. Polym.* **8**, 1059 (2011).
- [52] M. R. Baklanov, L. Zhao, E. V. Besien, and M. Pantouvaki, *Microelectronic Engineering* **88**, 990-993 (2011).
- [53] K. Takeda, Y. Miyawaki, S. Takashima, M. Fukasawa, K. Oshima, K. Nagahata, T. Tatsumi, and M. Hori, *J. Appl. Phys.* **109**, 033303 (2011).
- [54] S. Uchida, S. Takashima, M. Hori, and M. Fukasawa, *Jpn. J. Appl. Phys.* **47**, 3621 (2008).



## **Chapter 2      Plasma   Diagnostic   Techniques   and   Film Characterization Methods**

### **2.1 Introduction**

Plasma processing has been used for the manufacturing of microelectronic devices. With progression of the miniaturization of semiconductor devices, the more accurate etching processes, the more high selectivity, and the less damage processes have been required. Approaches to understand plasma etch process are categorized to plasma diagnostic and surface characterization.

In this Chapter, the experimental systems, diagnostic techniques of plasma and analysis method for subsurface reactions are described. Vacuum ultra-violet absorption spectroscopy (VUVAS) was used for measurement of radical densities in plasma. In order to obtain information of the composition on the sample surface, XPS was employed. The reactions of radical in bulk film were investigated by FTIR. On the basis of analysis resulting from these measurements, it could be expected to realize the development of sophisticated plasma nano-technology for the next generation process.

## 2.2 Vacuum Ultra-Violet Absorption Spectroscopy (VUVAS)

### 2.2.1 Theory of Absorption Spectroscopy

Optical measurement techniques, such as absorption spectroscopy, OES, etc. are very powerful for detecting the behaviors of activated species without the disturbance of process plasmas. Recently, these techniques have employed the light in the optical range between vacuum ultraviolet (VUV) and infrared (IR) for probing atomic and molecular radicals. If the parallel light from a source passes through an absorption cell, such as plasma, the intensity of the transmitted light is given as follows [1],

$$I(\nu) = I_0(\nu) \exp[-k(\nu)L], \quad (2.1)$$

where  $\nu$  is the frequency,  $I(\nu)$  and  $I_0(\nu)$  are the intensities of the transmitting light and the incident light, respectively.  $L$  is the absorption path length, and  $k(\nu)$  is the absorption coefficient as a function of frequency  $\nu$ .

The broadening of the absorption coefficient, that is, the broadening of the absorption line-profile is due to the causes as follows,

- (1) Natural broadening due to the finite lifetime of the excited state.
- (2) Doppler effect broadening due to the motions of the atoms.
- (3) Lorentz broadening due to collisions with foreign gases.
- (4) Holtsmark broadening due to collisions with other absorption atoms of the same kind.
- (5) Stark effect broadening due to collisions with electrons and ions.



However, in this study the Doppler broadening and Lorentz broadening are negligible, because the density of the electron and absorbing atoms of the same kind should be low.

Here, we consider that a parallel beam of the light of frequency  $\nu$  passed through a layer of atoms bounded by the planes at the length of  $dL$ . Suppose there are  $N_l$  normal atoms per  $\text{cm}^3$  of which  $dN_l$  are capable of absorbing the frequency range between  $\nu$  and  $\nu+d\nu$ , and  $N_u$  excited atoms of which  $dN_u$  are capable of emitting this frequency range. Neglecting the effect of spontaneous re-emission in view of the fact that it takes place in all direction, the decrease in energy of the beam is given by

$$-[I(\nu)]d\nu = dN_l dL \rho(\nu) B_{lu} h\nu - dN_u dL \rho(\nu) B_{ul} h\nu, \quad (2.2)$$

where  $B_{lu}$  and  $B_{ul}$  are Einstein B coefficient from ground state  $l$  to excited state  $u$  and from  $l$  to  $u$ , respectively.  $h$  is Planck's constant, and  $\rho(\nu)$  is the radiation energy density given by  $I(\nu)=c\rho(\nu)$ , ( $c$ : light velocity). Rewriting Eq. (2.2), we obtain

$$-\frac{1}{I(\nu)} \frac{d[I(\nu)]}{dL} d\nu = \frac{h\nu}{c} (B_{lu} dN_l - B_{ul} dN_u), \quad (2.3)$$

Recognizing that the left-hand term is  $k(\nu)d\nu$  as defined by Eq. (2-1), Eq. (2-3) becomes

$$k(\nu)d\nu = \frac{h\nu}{c} (B_{lu} dN_l - B_{ul} dN_u) \quad (2.4)$$

And integrating over the whole absorption line, neglecting the slight variation in  $\nu$  throughout the line,

$$\int k(\nu) d\nu = \frac{h\nu_0}{c} (B_{lu}N_l - B_{ul}N_u), \quad (2.5)$$

where  $\nu_0$  is the frequency at the center of the line. Here we use the Einstein A coefficient.

$$\begin{aligned} \int k(\nu) d\nu &= \frac{c^2}{8\pi\nu_0^2} \frac{g_u}{g_l} AN_l \left(1 - \frac{g_l N_u}{g_u N_l}\right) \\ &\cong \frac{c^2}{8\pi\nu_0^2} \frac{g_u}{g_l} AN_l \quad (N_u \ll N_l), \end{aligned} \quad (2.6)$$

where  $g_l$  and  $g_u$  are the statical weights of the lower and upper level, respectively. Therefore, by measuring  $I_0(\nu)$  and  $I(\nu)$ ,  $k(\nu)$  is decided and we can estimate the density  $N_l$ .

When the light source is incoherent light such as lamp, the intensity of measured light is the integrated value over the frequency

$$\begin{aligned} I_0 &= \int e_0 f_0(\nu) d\nu, \\ I_a &= \int e_0 f_0(\nu) \{1 - \exp[-k_0 f_a(\nu)L]\} d\nu, \end{aligned} \quad (2.7)$$

where  $I_0$  and  $I_a$  are the intensities of the incident light and the absorption, respectively,  $f_0(\nu)$  is the emission line-profile function for the light source,  $e_0$  is the emission intensity of the light source at a center frequency of  $f_0(\nu)$ ,  $f_a(\nu)$  is the absorption line-profile

function, and  $k_0$  is the absorption coefficient at the center frequency of  $f_a(\nu)$ . The intensity of absorbed light  $A(k_0L)$  is given by the following equation.

$$A(k_0L) = 1 - \frac{I_a}{I_0} = \frac{\int f_0(\nu) \{1 - \exp[-k_0 f_a(\nu)L]\} d\nu}{\int f_0(\nu) d\nu}. \quad (2.8)$$

From  $A(k_0L)$  obtained by measurement,  $k_0$  is determined by assuming the line-profile function  $f_0(\nu)$  and  $f_a(\nu)$ . Then, the number density of state  $l$ ,  $N_l$ , is estimated by using Eq. (2.6) as

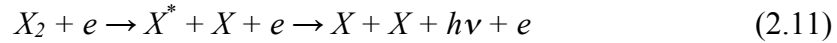
$$N_l = \frac{8\pi\nu_0^2}{c^2} \frac{g_l}{g_u} \frac{1}{A} k_0 \int f_a(\nu) d\nu. \quad (2.9)$$

### 2.2.2 Measurements of Absolute Densities of Atomic H and N Radicals with Micro-Discharge Hollow Cathode Lamp (MHCL)

Recently, our research group has developed the measurement system of absolute densities of atomic H [2], N [3] and O [4] radicals in the ground state using the VUVAS with micro-discharge hollow cathode lamp (MHCL) as a light source. Transition lines used for measuring the absolute densities of H, N and O radicals are Lyman  $\alpha$  at 121.6 nm,  $^4P_{5/2} - ^4S_{3/2}^0$ ,  $^4P_{3/2} - ^4S_{3/2}^0$  and  $^4P_{1/2} - ^4S_{3/2}^0$  at 120.0 nm and  $^3S^0 - 2p^4\ ^3P_2$  at 130.217 nm,  $3s\ ^3S^0 - 2p^4\ ^3P_1$  130.487 nm and  $3s\ ^3S^0 - 2p^4\ ^3P_0$  130.604 nm, respectively. Each emission of these transition lines can be obtained by the H<sub>2</sub>, N<sub>2</sub> and O<sub>2</sub> plasma, respectively. However, these emissions are caused by two major processes [5-7]. One is the direct excitation of ground state atomic radicals by the electron impact.



, where  $X$  is the atomic radical of interest,  $X^*$  is  $X$  atoms in the excited state. The other is the dissociative excitation of ground state of  $X_2$  by the electron impact.



Reaction (2.10) is responsible for the production of slow excited  $X^*$  atoms. Reaction (2.11) can produce fast excited  $X$  atoms which produce a large Doppler broadening. Therefore, the structure of the atomic radical emission line profile consists of a two-component velocity distribution arising from two different excitation processes as shown in Eqs. (2.10) and (2.11). It is difficult to estimate the emission line profile, which involves a two-component velocity distribution. In the view of problem above in the measurement of absolute atomic radical density, we have developed a high pressure MHCL as a light source for VUVAS. The specific merits of the MHCL we expect are as follows,

- (1) The emission line profile will not involve a large Doppler shift due to the fast excited atomic radical arising from dissociative excitation of molecules, since they should be thermalized before they emit light.
- (2) The size of the hollow cathode is as small as 0.1 mm diameter, resulting in a high current density in the cathode, which is favorable for attaining a high dissociation degree of molecules and obtaining spectrally pure atomic radical emission.
- (3) A point-source-like emission from a micro-hollow can be efficiently coupled to the entrance slit of a monochromator using an appropriate lens system.
- (4) The lamp is compact and is operated with an inexpensive dc power source.

## Chapter 2

The cathode and anode consist of a plate with 0.5 mm thickness with a through-hole hollow of 0.1 mm in diameter. Helium (250 sccm) and helium gas containing a small amount of  $H_2$  and  $N_2$  gas (5 sccm) were used. The MHCL was operated at a total pressure of 0.1 MPa.

### 2.3 Optical Emission Spectroscopy (OES)

Many optical emissions originating from excited species (e.g. atomic and molecular radicals) are generally observed in the plasma. Specific species is identified by the photon energy of the optical emission. Excited species are generated by various processes such as electron collision, dissociation, impact of other excited species, photon absorption, etc. Generally, excitation by electron impact frequently occurs in the plasma. Electron impact excitation of the ground state is given by



where  $X$  is the species of interest. De-excitation is followed by the emission of a photon from the excited state as,



The intensity of the optical emission due to the transition from an excited state to the ground state is given by

$$I_x \propto n_e n_X \int \sigma_X(\varepsilon) \nu(\varepsilon) f_e(\varepsilon) d\varepsilon = k_{eX} n_e n_X, \quad (2.14)$$

where  $n_e$  is the electron density,  $n_X$  is the concentration of  $X$ ,  $\sigma_X(\varepsilon)$  is the collision cross section for the electron impact excitation of  $X$  as a function of electron energy  $\varepsilon$ ,  $\nu(\varepsilon)$  is the electron velocity and  $f_e(\varepsilon)$  is the electron energy distribution function (EEDF).  $k_{eX}(\varepsilon)$  is the excitation rate coefficient for  $X^*$  by the electron impact on  $X$ . Under the condition where  $k_{eX}$  and  $n_e$  are kept constant, the emission intensity is proportional to the

concentration of species. However, both of them are affected by the experimental conditions and are generally so difficult to be kept constant when external parameters, such as input power, working pressure, are varied in the plasma processing. Thereby, optical emission spectroscopy (OES) technique is widely used as a monitoring tool in various plasma processes. Moreover, in order to compare those emission intensities with the concentration of species, it is necessary to assume that emissions from excited states chosen are proportional to the concentration of the same species in the ground state. Therefore, the special technique such as actinometric optical emission spectroscopy (AOES) is frequently applied to estimate relative concentration of species in the ground state [8-14].

Optical emission spectra are generally measured by using a spectrometer. Usually, a monochromator with a photomultiplier tube (PMT) and multi-channel spectrometer with a charged coupled device (CCD) array are used. In a monochromator the light intensity is detected through the exit slit by PMT, as shown in Fig. 2.1(a). On the other hand, in a multi-channel spectrometer the light intensity is detected by each pixel of CCD, as shown in Fig. 2.1(b). The advantage of the multi-channel spectrometer is that it can measure a wide range (several ten nm) of wavelength simultaneously; however, the defect of the multi-channel spectrometer is that the resolution is restricted by the size of the pixel of CCD. The resolution of spectrometer sometimes limits the accuracy of measurements.

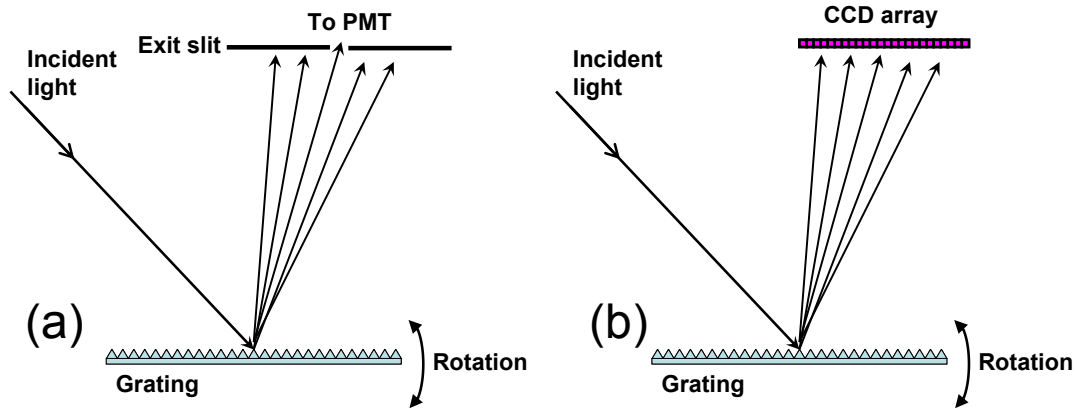


Fig. 2.1 The schematic illustration of (a) monochromator and (b) multi-channel spectrometer.

A spectral line measured by a spectrometer has a certain width. The full width at half maximum (FWHM) of the spectral line is determined by various factors such as natural broadening, Doppler broadening, pressure broadening, Stark broadening, and instrumental broadening (instrumental function). The natural broadening giving a Lorentzian line shape, however, is generally very small and negligible. Doppler broadening depends on the temperature of the species of interest. Doppler broadening gives a Gaussian line shape as,

$$f_D(\nu) = \exp \left[ - \left\{ 2\sqrt{\ln 2} \frac{(\nu - \nu_0)}{\Delta \nu_D} \right\}^2 \right], \quad (2.15)$$

with

$$\Delta \nu_D = \frac{2\nu_0}{c} \sqrt{\frac{2RT \ln 2}{M}}. \quad (2.16)$$



## Chapter 2

Where  $\Delta\nu_D$  is the FWHM of the Doppler broadening,  $\nu_0$  is the center frequency,  $c$  is the velocity of light,  $R$  is the gas constant,  $T$  is the gas temperature,  $M$  is the mass number. Pressure broadening depends on pressure around the species of the interest gives a Lorentzian function as,

$$f_P(\nu) = \frac{\Delta\nu_P}{2 \left\{ 4(\nu - \nu_0)^2 + \left( \frac{\Delta\nu_P}{2} \right)^2 \right\}}, \quad (2.17)$$

with

$$\Delta\nu_P = \frac{1}{\pi} z = \frac{1}{\pi} \cdot n \cdot \sigma \cdot \sqrt{\frac{8RT}{\pi\mu}}, \quad (2.18)$$

where  $\nu_P$  is the FWHM of the pressure broadening,  $z$  is the collision frequency,  $n$  is the concentration of the species,  $\sigma$  is the collision cross section,  $\mu$  is the reduced mass. Stark broadening depends on the electric field caused by charged particles such as electrons and ions. Therefore, the electron density can be derived from the Stark width. The instrumental broadening depends on the performance of the spectrometer used in the experiment. In order to determine the instrumental function, a light source such as a low-pressure mercury lamp is generally used, which gives enough sharp spectral lines compared to the instrumental function. The actual spectrum is determined from the convolution of the various broadening mechanisms. The convolution of Gaussian and Lorentzian functions results in a Voigt profile. Voigt function is given by,

$$f_V(\nu) = \frac{a}{\pi} \int \frac{\exp(-y^2)}{a^2 + (\omega + y)^2} dy, \quad (2.19)$$

with

$$a = \frac{\Delta\nu_L}{\Delta\nu_G} \sqrt{\ln 2}, \quad (2.20)$$

and

$$\omega = \frac{2(\nu - \nu_0) \sqrt{\ln 2}}{\Delta\nu_G}, \quad (2.21)$$

where  $\Delta\nu_L$  is the FWHM of the Lorentz broadening,  $\Delta\nu_G$  is the FWHM of the Gaussian broadening.

## 2.4 Microwave Interferometer

Microwave interferometer, the most common wave diagnostics technique, has been used to measure plasma density by propagation measurement. Spatial resolution inferior to probe measurement such as Langmuir probe, however, time response is faster and the propagation measurement does not disturb plasmas. The principle of its use is that change in phase shift across a region with and without plasma can be measured. This in turn can be related to the change in propagation constant and hence to the plasma frequency.

Since the propagation constant of a wave is dependent on the plasma frequency of electron is given by

$$\omega_{pe} = \sqrt{\frac{e^2 n_e}{\epsilon_0 m_e}} \quad (2.22)$$

propagation measurement have been used to measure plasma density. Here,  $e$ ,  $n_e$ ,  $m_e$ , and  $\epsilon_0$  are charge of electron ( $1.6 \times 10^{-19}$  C), electron density, mass of electron ( $9.1 \times 10^{-31}$  kg), and permittivity (or dielectric function) of a plasma ( $8.854 \times 10^{-12}$  F/m), respectively. The change in phase shift is given by

$$\Delta\phi = k_0 \int_0^l \left[ 1 - \frac{\omega_p^2(x)}{\omega^2} \right]^{1/2} dx - l \quad (2.23)$$

where  $k_0 = \omega/c$  is the free space propagation constant, and  $l$  is the wave propagates across a region of length. It is often possible to choose the diagnostics frequency sufficiently high compared to plasma frequency that square root can be expanded. The free space part of the phase shift the conveniently cancels leaving

$$\Delta\phi \approx k_0 \int_0^l \frac{\omega_p^2(x)}{2\omega^2} dx = \frac{k_0 e^2}{2\varepsilon_0 m \omega^2} \int_0^l n(x) dx \quad (2.24)$$

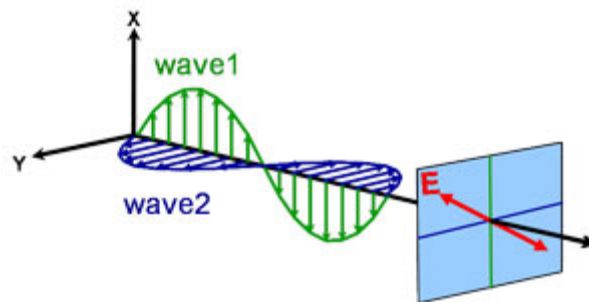
In this approximation, we see that the line integral of the density can be directly measured in term of a phase shift [15].

## 2.5 Spectroscopic Ellipsometry [16]

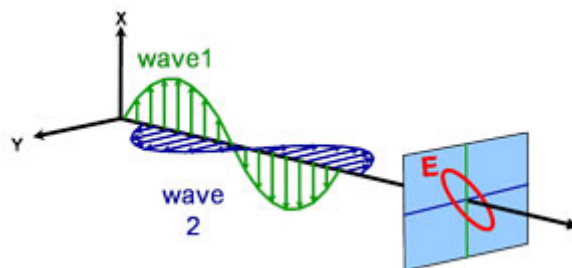
Ellipsometry is a truly powerful technique of interest and use to physicists, chemists, electrochemists, electrical and chemical engineers. Ellipsometry measures a change in polarization as light reflects or transmits from a material structure. The polarization change is represented as an amplitude ratio,  $\Psi$ , and the phase difference,  $\Delta$ . The measured response depends on optical properties and thickness of individual materials. Thus, ellipsometry is primarily used to determine film thickness and optical constants. However, it is also applied to characterize composition, crystallinity, roughness, doping concentration, and other material properties associated with a change in optical response. Since the 1960s, as ellipsometry developed to provide the sensitivity necessary to measure nanometer-scale layers used in microelectronics, interest in ellipsometry has grown steadily. Today, the range of its applications has spread to the basic research in physical sciences, semiconductor and data storage solutions, flat panel display, communication, biosensor, and optical coating industries.

Ellipsometry measures the interaction between light and material. Light can be described as an electromagnetic wave traveling through space. For purposes of ellipsometry, it is adequate to discuss the waves's electric field behavior in space and time, also known as polarization. The electric field of a wave is always orthogonal to the propagation direction. Therefore, a wave traveling along the z-direction can be described by its x- and y- components. When the light has completely random orientation and phase, it is considered unpolarized. For ellipsometry, however, we are interested in the kind of electric field that follows a specific path and traces out a distinct shape at any point. This is known as polarized light. When two orthogonal light waves are in-phase, the resulting light will be linearly polarized [Fig. 2.2(a)]. The relative amplitudes determine the resulting orientation. If the orthogonal waves are 90° out-of-phase and equal in amplitude, the resultant light is circularly polarized [Fig.

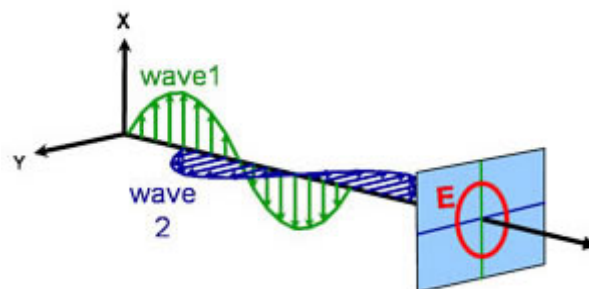
2.2(b)]. The most common polarization is “elliptical”, one that combines orthogonal waves of arbitrary amplitude and phase [Fig. 2.2(c)].



(a)



(b)



(c)

Fig. 2.2 Orthogonal waves combined to demonstrate polarization:

(a) linear, (b) circular and (c) elliptical.

Maxwell's equations must remain satisfied when light interacts with a material, which leads to boundary conditions at the interface. Incident light will reflect and refract at the interface, as shown in Fig. 2.3. The angle between the incident ray and sample normal ( $\phi_i$ ) will be equal to the reflected angle, ( $\phi_r$ ). Light entering the material is refracted at an angle ( $\phi_t$ ) given by:

$$n_0 \sin(\Phi_i) = n_i \sin(\Phi_t) \quad (2.25)$$

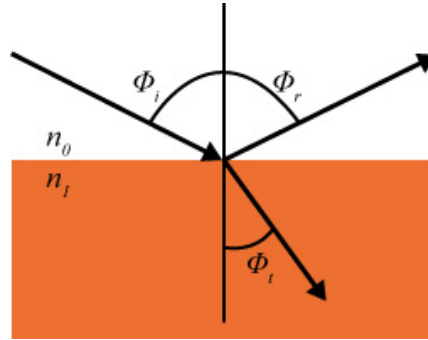


Fig. 2.3 Light reflects and refracts according to Snell's law

The same occurs at each interface where a portion of light reflects and the remainder transmits at the refracted angle. This is illustrated in Fig. 2.4. The boundary conditions provide different solutions for electric fields parallel and perpendicular to the sample surface. Therefore, light can be separated into orthogonal components with relation to the plane of incidence. Electric fields parallel and perpendicular to the plane of incidence are considered p- and s- polarized, respectively. These two components are independent and can be calculated separately. Fresnel described the amount of light reflected and transmitted at an interface between materials:

$$r_s = \left( \frac{E_{or}}{E_{0i}} \right)_s = \frac{n_i \cos(\Phi_i) - n_t \cos(\Phi_t)}{n_i \cos(\Phi_i) + n_t \cos(\Phi_t)} \quad (2.26)$$

$$r_p = \left( \frac{E_{or}}{E_{0i}} \right)_p = \frac{n_t \cos(\Phi_i) - n_i \cos(\Phi_t)}{n_i \cos(\Phi_t) + n_t \cos(\Phi_i)} \quad (2.27)$$

$$t_s = \left( \frac{E_{ot}}{E_{0i}} \right)_s = \frac{2n_i \cos(\Phi_i)}{n_i \cos(\Phi_i) + n_t \cos(\Phi_t)} \quad (2.28)$$

$$t_p = \left( \frac{E_{ot}}{E_{0i}} \right)_p = \frac{2n_i \cos(\Phi_i)}{n_i \cos(\Phi_t) + n_t \cos(\Phi_i)} \quad (2.29)$$

Thin film and multilayer structures involve multiple interfaces, with Fresnel reflection and transmission coefficients applicable at each. It is important to track the relative phase of each light component to determine correctly the overall reflected or transmitted beam. For this purpose, we define the film phase thickness as:

$$\beta = 2\pi \left( \frac{t_1}{\lambda} \right) n_1 \cos(\Phi_1) \quad (2.30)$$

The superposition of multiple light waves introduces interference that depends on the relative phase of each light wave. Figure 2.3 illustrates the combination of light waves in the reflected beam and their corresponding Fresnel calculations.



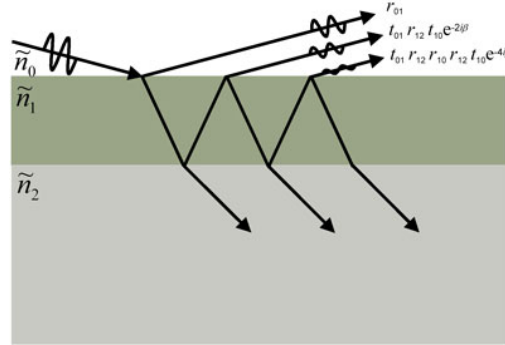


Fig. 2.4 Light reflects and refracts at each interface, which leads to multiple beams in a thin film. Interference between beams depends on relative phase and amplitude of the electric fields. Fresnel reflection and transmission coefficients can be used to calculate the response from each contributing beam.

Ellipsometry is primarily interested in how  $p$ - and  $s$ - components change upon reflection or transmission in relation to each other. In this manner, the reference beam is part of the experiment. A known polarization is reflected or transmitted from the sample and the output polarization is measured. The change in polarization is the ellipsometry measurement, commonly written as:

$$\rho = \tan(\psi) e^{i\Delta} \quad (2.31)$$

A sample ellipsometry measurement is shown in Fig. 2.5. The incident light is linear with both p- and s- components. The reflected light has undergone amplitude and phase changes for both p- and s- polarized light, and ellipsometry measures their changes.

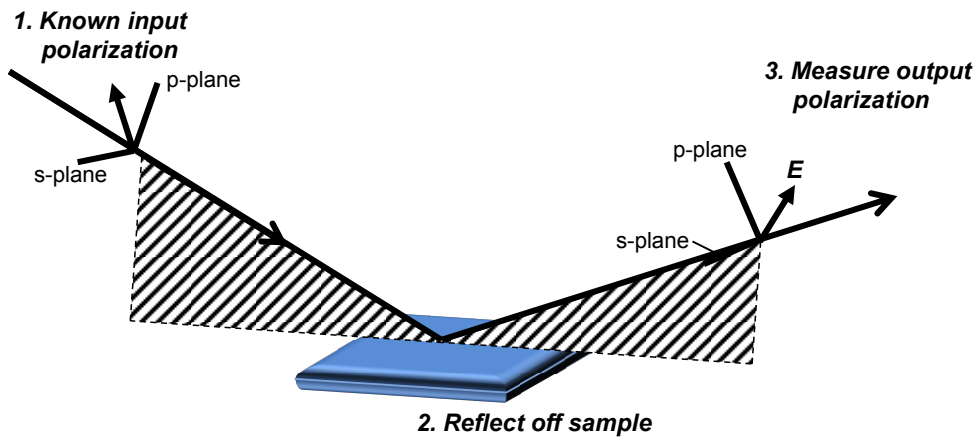


Fig. 2.5 Typical ellipsometry configuration, where linearly polarized light is reflected from the sample surface and the polarization change is measured to determine the sample response.

The film thickness is determined by interference between light reflecting from the surface and light traveling through the film. Depending on the relative phase of the rejoining light to the surface reflection, interference can be defined as constructive or destructive. The interference involves both amplitude and phase information. The phase information from  $\Delta$  is very sensitive to films down to sub-monolayer thickness. Ellipsometry is typically used for films whose thickness ranges from sub-nanometers to a few microns. As films become thicker than several tens of microns, interference oscillations become increasingly difficult to resolve, except with longer infrared wavelengths. Other characterization techniques are preferred in this case. Thickness measurements also require that a portion of the light travel through the entire film and return to the surface. If the material absorbs light, thickness measurements by optical instruments will be limited to thin, semi-opaque layers. This limitation can be circumvented by targeting measurements to a spectral region with lower absorption. For

## Chapter 2

example, an organic film may strongly absorb UV and IR light, but remain transparent at mid-visible wavelengths. For metals, which strongly absorb at all wavelengths, the maximum layer for thickness determination is typically about 100 nm.

## 2.6 Fourier Transform Infrared Spectroscopy (FTIR)

Fourier Transform Infrared Spectroscopy (FTIR) allows us to detect infrared (IR) absorption and reflection properties of materials [17-19]. FTIR is widely used to evaluate for a chemical bonding such as C-H, C-F, C-N, C-O, Si-CH<sub>3</sub>, Si-O-Si [20-24], and so on. The foundations of FTIR were laid in the latter part of the nineteenth century by Michelson [25], Raleigh [26], Rubens and Wood [27], von Baeyer [28], and others who recognized the relationship of an interferogram to its spectrum by a Fourier transformation. It was not until the advent of computers and the fast Fourier algorithm that interferometry began to be applied to spectroscopic measurements in the 1970s. FTIR is based on a Michelson interferometer, which consists of a beam splitter, a fixed mirror and a moving mirror (scanning mirror) [29]. Light from the source (see Fig. 2.6) is separated into two parts and then recombines at the beam splitter after reflection by the two mirrors as shown in Fig. 2.7. The transmission factor and the reflection coefficient of beam splitter are  $T_0$  and  $R_0$ , respectively. Light  $I_0$  (wave number  $\nu$ ) from the infrared source is collimated and directed onto a beam splitter. The light intensity reaching the detector is the sum of the two beams. In the case of  $L_1 = L_2$  ( $L_1$ : distance between beam splitter and fixed mirror  $M_1$ ,  $L_2$ : distance between beam splitter and fixed mirror  $M_2$ ), the light intensity of  $2I_0T_0R_0$ , enters the detector. When  $M_1$  is moved, the optical path lengths are unequal and an optical path difference  $\delta$  is introduced. If  $M_1$  is moved a distance, the retardation is  $\delta = 2x$  since the light has to travel an additional distance  $x$  to reach the mirror and the same distance to reach the beam splitter. The light intensity  $I_{\text{obs}}(x)$  reaching the detector depends on the value of  $x$  that can be described by the equation

$$I_{\text{obs}}(x) = 2R_0T_0I_0[1 + \cos(2\pi\nu x)]. \quad (2.32)$$

when  $R_0, T_0 = 0.5$ , Eq. (2.32) is

$$I_{obs}(x) = \frac{I_0}{2} [1 + \cos(2\pi\nu x)]. \quad (2.33)$$

Consider the light have the wave number  $\nu_1 - \nu_2$  and the intensity  $I_0(\nu)$ . When the source emits more than one frequency, Eq. (2.34) replaced by the integration

$$I_{obs}(x) = \int_{\nu_1}^{\nu_2} \frac{I_0(\nu)}{2} [1 + \cos(2\pi\nu x)] d\nu. \quad (2.34)$$

Direct current from the interference output signal of Eq. (2.34) is subtracted.

$$F(x) = \frac{1}{2} \int_{\nu_1}^{\nu_2} I_0(\nu) \cos(2\pi\nu x) d\nu. \quad (2.35)$$

Due to the path difference between the two beams, an interference pattern is generated. The output beam from interferometer is recorded as a function of path difference, and is called the interferogram (see Fig. 2.8). When Eq. (2.35) is generalize

$$F(x) = \int_{-\infty}^{\infty} I_0(\nu) \exp(2\pi x \nu i) d\nu. \quad (2.36)$$

The incident radiation  $I_0(\nu)$  is obtained by the Fourier transform of the interferogram actually measured.

$$I_0(x) = \frac{1}{2} \int_{-\infty}^{\infty} F(\nu) \exp(2\pi x \nu i) d\nu. \quad (2.37)$$

The IR spectrum can be obtained by calculating the Fourier transform of the interferogram.

There are two primary advantages to using FTIR as compared to a dispersive spectrometer, Fellgett's advantage (Multiplex advantage) and Jacquinot's advantage (Throughput advantage). Generally, the signal-to-noise ratio (SNR) is proportional to the number of scans or measurement time  $T$  ( $\text{SNR} \propto \sqrt{T}$ ). In a broadband spectrum, the number of spectral elements  $n$  between the frequency range  $\nu_1$  and  $\nu_2$  can be defined as  $n = (\nu_2 - \nu_1)/\Delta\nu$ . In a dispersive spectrometer, a particular spectral element is recorded in a time  $t$ , so that the total time required is  $T = nt$ . However, the FTIR spectrometer records information for all wavelengths in the spectrum simultaneously. During each scan, it records  $n$  times faster than a dispersive spectrometer with the same SNR. If the measurement time is the same, then the SNR will be increased by factor of  $\sqrt{n}$ . In a dispersive spectrometer the energy throughput is limited by the entrance and exit slits of the monochromator. Since the FTIR does not require slits, measurements at higher intensities are possible. To increase the resolution of a dispersive spectrometer, the slits must be narrowed. In an FTIR, resolution is increased by increasing mirror travel distance with no decrease in energy throughput.

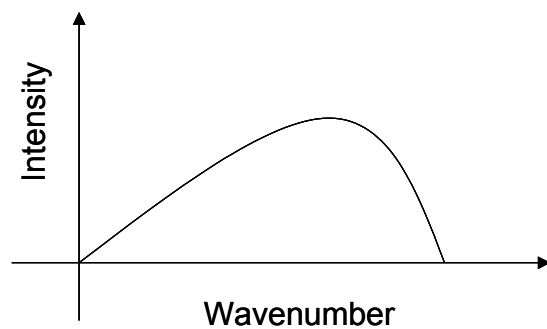


Fig. 2.6 Spectrum of light source.

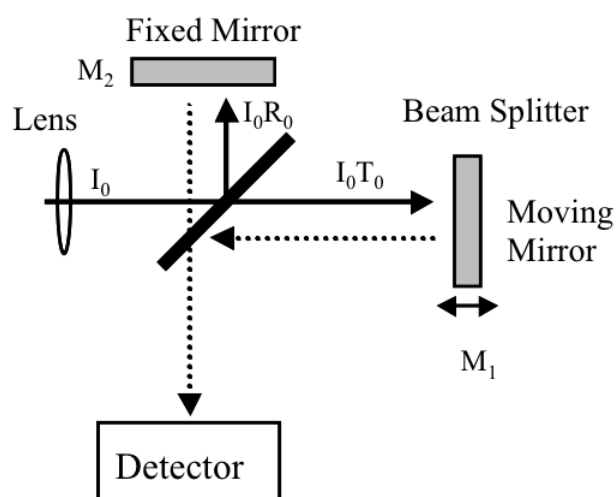


Fig. 2.7 Schematic diagram of FTIR.

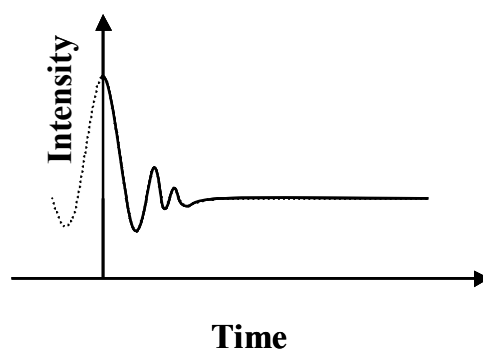


Fig. 2.8 Interferogram.

## 2.7 X-Ray Photoelectron Spectroscopy (XPS)

X-ray photoelectron spectroscopy (XPS) is currently the most widely used surface-analytical technique, and is therefore described here in more detail than any of the other techniques. At its inception by Seigbahn and coworkers [30], it was called ESCA (electron spectroscopy for chemical analysis), but the name ESCA is now considered too general, because many surface-electron spectroscopies exist, and the name given to each one must be precise. The name ESCA is, nevertheless, still used in many places, particularly in industrial laboratories and their publications. Briefly, the reasons for the popularity of XPS are the exceptional combination of compositional and chemical information that it provides, its ease of operation, and the ready availability of commercial equipment.

The surface to be analyzed is irradiated with soft X-ray photons. When a photon of energy  $h\nu$  interacts with an electron in a level X with the binding energy  $E_B$  ( $E_B$  is the energy  $E_K$  of the K-shell in Fig. 2.9), the entire photon energy is transferred to the electron, with the result that a photoelectron is ejected with the kinetic energy

$$E_{\text{kin}}(h\nu, X) = h\nu - E_B - \Phi_s \quad (2.38)$$

where  $\Phi_s$  is a small, almost constant, work function term.

Obviously,  $h\nu$  must be greater than  $E_B$ . The ejected electron term can come from a core level or from the occupied portion of the valence band, but in XPS most attention is focused on electrons in core levels. Because no two elements share the same set of electronic binding energies, measurement of the photoelectron kinetic energies enables elemental analysis. In addition, Eq. (2.38) indicates that any changes in  $E_B$  are reflected in  $E_{\text{kin}}$ , which means that changes in the chemical environment of an atom can be followed by monitoring changes in the photoelectron energies, leading to the provision



of chemical information. XPS can be used for analysis of all elements in the periodic table except hydrogen and helium.

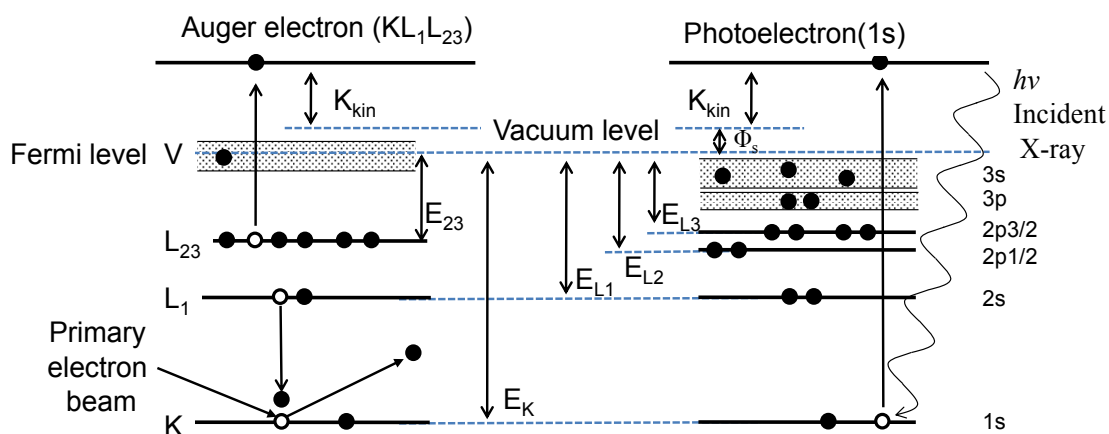


Fig. 2.9 Schematic diagram of electron emission processes in solids.

Left side: Auger process, right side: photoelectron process.

Electrons involved in the emission processes are indicated by open circles.

Although XPS is concerned principally with photoelectron and their kinetic energies, ejection of electron by other processes also occurs. An ejected photoelectron leaves behind a core hole in the atom. The sequence of events following the creation of the hole is shown schematically in Fig. 2.9 (right side). In the example, the hole has been created in the K-shell, giving rise to a photoelectron, the kinetic energy of which would be  $(h\nu - E_K)$ , and is filled by an electronic transition from the unresolved L<sub>23</sub> shell. The energy  $E_K - E_{L23}$  associated with the transition can then either be dissipated as a characteristic X-ray photon or given up to an electron in the same or a higher shell, shown in this example also as the L<sub>23</sub>. The second of these possibilities is called the Auger process after its discoverer [31], and the resulting ejected electron is called an

Auger electron and has kinetic energy given by:

$$E_{\text{kin}}(\text{KL}_1\text{L}_{23}) = E_K - E_{\text{L}_1} - E_{\text{L}_{23}} - E_{\text{inter}}(\text{L}_1\text{L}_{23}) + E_R - \Phi_s \quad (2.39)$$

Where  $E_{\text{kin}}(\text{KL}_1\text{L}_{23})$  is the interaction energy between the holes in the  $\text{L}_1$  and  $\text{L}_{23}$  shell and  $E_R$  is the sum of the intra-atomic relaxation energies. X-ray photon emission and Auger electron emission are obviously competing processes, but for the shallow core levels involved in XPS and AES the Auger process is for more likely.

Thus in all X-ray photoelectron spectra, features appear as a result of both photo-emission and Auger emission. In XPS, the Auger features can be useful but are not central to the technique, whereas in AES, Eq. (2.39) forms the basis of the technique. At this point the nomenclature used in XPS and AES should be explained. In XPS the spectroscopic notation is used, and in AES the X-ray notation. The two are equivalent, the different usage having arisen for historical reasons, but the differentiation is a convenient one. They are both based on the so-called  $j$ - $j$  coupling scheme describing the orbital motion of an electron around and atomic nucleus, in which the total angular momentum of an electron is found by summing vectorially the individual electron spin and angular momenta. Thus if  $l$  is the electronic angular momentum quantum number and  $s$  the electronic spin momentum quantum number, the total angular momentum for each electron given by  $j = l + s$ . Because  $l$  can take the values 0, 1, 2, 3, 4, ... and  $s = \pm 1/2$  clearly  $j = 1/2, 3/2, 5/2$  etc. The principal quantum number  $n$  can take values 1, 2, 3, , ... In spectroscopic notation, states with  $l = 0, 1, 2, 3, \dots$  are designated  $s, p, d, f, \dots$  respectively, and the letter is preceded by the number  $n$ ; the  $j$  values are then appended as suffixes. Therefore, one obtains  $1s, 2s, 2p_{1/2}, 2p_{3/2}$ .

In X-ray notation, states with  $n = 1, 2, 3, 4 \dots$  are designated K, L, M, N, ..., respectively, and states with various combinations of  $l = 0, 1, 2, 3, \dots$  and  $j = 1/2, 3/2, 5/2$  are appended as the suffixes 1, 2, 3, 4 ... In this way one arrives at K,  $\text{L}_1, \text{L}_2, \text{L}_3, \text{M}_1,$

M<sub>2</sub>, M<sub>3</sub>, etc. The equivalence of the two notations is set out in Table 1.

Table 1 Spectroscopic and X-ray notation.

<i>Quantum number</i>			<i>Spectroscopic state</i>	<i>X-ray state</i>
<i>n</i>	<i>l</i>	<i>j</i>		
1	0	1/2	1s	K
2	0	1/2	2s	L <sub>1</sub>
2	1	1/2	2p <sub>1/2</sub>	L <sub>2</sub>
2	1	3/2	2p <sub>3/2</sub>	L <sub>3</sub>
3	0	1/2	3s	M <sub>1</sub>
3	1	1/2	3p <sub>1/2</sub>	M <sub>2</sub>
3	1	3/2	3p <sub>3/2</sub>	M <sub>3</sub>
3	2	3/2	3d <sub>3/2</sub>	M <sub>4</sub>
3	2	5/2	3d <sub>5/2</sub>	M <sub>5</sub>
<i>etc.</i>	<i>etc.</i>	<i>etc.</i>	<i>etc.</i>	<i>etc.</i>

## 2.8 Substrate Temperature Measurement System

The substrate temperature was calculated from the change of optical thickness of Si wafer measured by an optical fiber-type low-coherence interferometer. Schematic diagram of temperature measurement system is shown in Fig. 2.10. The measurement system is based on a Michelson interferometer, which consists of a super luminescent diode (SLD), a reference mirror scanner, a fiber collimator, an optical fiber and so on. The SLD light is divided into two beams by the fiber coupler. One beam irradiates the substrate. The other beam goes to a scanning reference mirror. In the substrate, the SLD light is reflected on the substrate backside and surface. In the reference mirror scanner side, the reference-optical-path length is changed because the mirror is moved. The lights reflected at the substrate go back to the fiber coupler through the fiber collimator, and then interfered with the light reflected at the scanning reference mirror within the range of coherence length. The position of interferogram was changed by the thermal expansion and the change of refractive index with increasing the substrate temperature. The change of temperature was measured by the shift of the peak position of interferogram. By using this measurement system, we can measure the substrate temperature in the real time [32,33].

The optical-path length  $L$  of a certain substance is

$$L = n \cdot d \quad (2.40)$$

where  $n$  is the index of refraction and  $d$  is the thickness of the substance. The SLD used in this article has a 48 nm bandwidth at a central wavelength of 1.55  $\mu\text{m}$ . Under these conditions, the effect of group index on the interference signal was negligible small. Therefore, we can discuss the principle without the effect.

If the temperature of the substance varies from  $T$  to  $T + \Delta T$ , the index of

refraction and the thickness vary as follows.

$$d \rightarrow d(1 + \alpha\Delta T) \quad (2.41)$$

$$n \rightarrow n(1 + \beta\Delta T) \quad (2.42)$$

Where  $\alpha$  and  $\beta$  are the measures of thermal expansion and the temperature dependence of the refractive index, respectively.  $\alpha$  is independent of optical wavelength while  $\beta$  is dependent on it. The optical-path length  $L'$  of the substance under the temperature shift  $\Delta T$  is

$$\begin{aligned} L' &= n(1 + \beta\Delta T) \times d(1 + \alpha\Delta T) \\ &= n \cdot d \{1 + (\alpha + \beta)\Delta T\} \end{aligned} \quad (2.43)$$

The shift of optical-path length is given by

$$\begin{aligned} L - L' &= n\{1 + (\alpha + \beta)\Delta T\}d - n \cdot d \\ &\cong n \cdot d(\alpha + \beta)\Delta T \end{aligned} \quad (2.44)$$

If  $\alpha$ ,  $\beta$  and the initial optical-path length (that is,  $n \cdot d$ ) are known, we can obtain the temperature shift ( $\Delta T$ ) of the substance from Eq. (2.44). The  $\alpha$  and  $\beta$  of silicon, which is commonly used in SOIs, are well investigated experimentally. The  $\alpha$  and  $\beta$  of silicon, denoted by  $\alpha_{Si}$  and  $\beta_{Si}$ , are approximately expressed as

$$\begin{aligned} \alpha_{Si}(T) &\cong -7.06 \times 10^{-11} \times T^2 \\ &+ 6.83 \times 10^{-8} \times T + 2.38 \times 10^{-6} \end{aligned} \quad (2.45)$$

$$\begin{aligned} \beta_{Si}(T) &\cong -3.33 \times 10^{-11} \times T^2 \\ &+ 6.76 \times 10^{-8} \times T + 5.01 \times 10^{-5} \end{aligned} \quad (2.46)$$

The  $\alpha$  and  $\beta$  of the quartz ( $\alpha_{\text{SiO}_2}$ ,  $\beta_{\text{SiO}_2}$ ) used as an interlayer of SOI are not known experimentally; therefore, the  $\alpha_{\text{SiO}_2}$  and  $\beta_{\text{SiO}_2}$  were assumed to be constant.

$$\alpha_{\text{SiO}_2} = 5.0 \times 10^{-7} \quad (2.47)$$

$$\beta_{\text{SiO}_2} = 7.0 \times 10^{-6} \quad (2.48)$$

Using these values or the values derived from the optical path lengths measured at different known temperatures in advance, we can find the temperature shift of layers from Eq. (2.44).

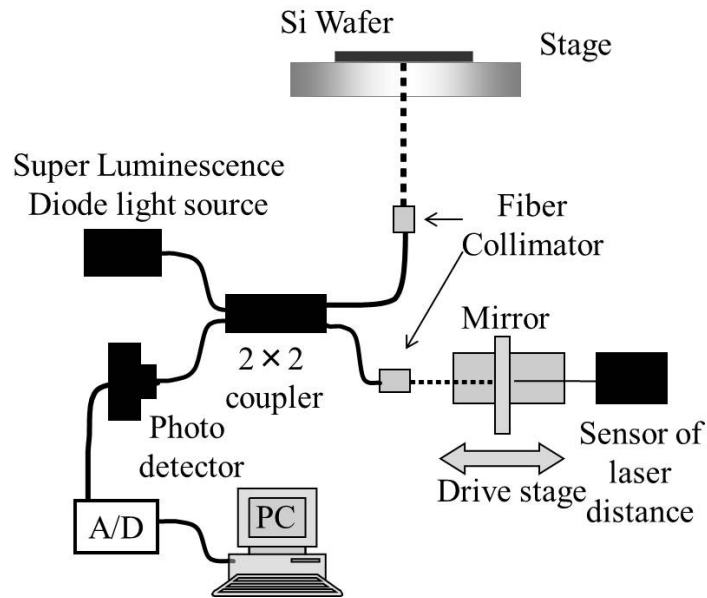


Fig. 2.10 Schematic diagram of temperature measurement system.

## 2.9 Secondary Ion Mass Spectrometry (SIMS)

Secondary ion mass spectrometry (SIMS), also known as ion microprobe and ion microscope, is a powerful technique used to analyze the composition of solid surfaces and thin films by sputtering the surface of the specimen with a focused primary ion beam and collecting and analyzing ejected secondary ions [29,34]. The technique is element specific and is capable of detecting all elements as well as isotopes and molecular species. Of all the beam techniques it is the most sensitive with detection limits for some elements in the  $10^{14}$  to  $10^{15}$  cm<sup>-3</sup> range if there is very little background interference signal. Lateral resolution is typically 100  $\mu$ m but can be as small as 0.5  $\mu$ m with depth resolution of 5 to 10 nm.

Destructive removal of target material from the sample is required to analyze the ejected materials by a mass analyzer. A primary ion beam impinges on the sample and atoms are sputtered or ejected from the sample. Most of the ejected atoms are neutral. Conventional SIMS cannot detect the neutral atoms, but some are positively or negatively charged. This fraction was estimated as around 1% of the total [35]. The mass/charge ratio of the ions is analyzed, detected as a mass spectrum, as a count, or displayed on a fluorescent screen. The detection of the mass/charge ratio can be problematic, since variation of complex molecules from during the sputtering process between the sputtered ions and light elements like H, C, O, and N typically found in SIMS vacuum systems. The mass spectrometer only recognizes the total mass/charge ratio and can mistake one ion for another.

Sputtering is a process in which incident ions lose their energy mainly by momentum transfer as they come to rest within the solid. In the process they displace atoms within the sample. Sputtering takes place when atoms near sample surface receive sufficient energy from the incident ion to be ejected from the sample. The escape depth of the sputtered atoms is generally a few monolayers for primary energies

of 10 to 20 keV typically used in SIMS. The primary ion loses its energy in the process and comes to rest tens of nm below the sample surface. Ion bombardment leads not only to sputtering, but also to ion implantation and lattice damage. The sputtering yield is the average number of atoms sputtered per incident primary ion. It depends on target material, its crystallographic orientation, and the nature, energy, and incidence angle of the primary ions. Selective or preferential sputtering can occur in multi-component or polycrystalline targets when the components have different sputtering yield. The component with lowest yield becomes enriched at the surface while that the highest yield becomes depleted. However, once equilibrium is reached, the sputtered materials leaving the surface has the same composition as the bulk material and preferential sputtering is not a problem in SIMS analysis.

The yield for SIMS measurements with  $\text{Cs}^+$ ,  $\text{O}_2^+$ ,  $\text{O}^-$ , and  $\text{Sr}^+$  ions of energy ranges from 1 to 20 keV. It is important to detect, we should choice primary ions because the secondary ion yield is significantly lower than the total yield, but can be influenced by the type of primary ion. Electronegative oxygen enhances species for electropositive elements which produce predominantly positive secondary ions. Electronegative elements have higher yields when sputtered with electropositive ions like  $\text{Cs}^+$ . The secondary ion yield for the elements varies over five to six order of magnitude.

SIMS has not only a wide variation in secondary ion yield among different elements, it also shows strong variations in the secondary ion yield from the same element in different samples or materials.

SIMS has measurement mode of two types, which are static and dynamic SIMS. For low incident ion beam current or low sputtering rate (approximately 0.1 nm per hour), a complete mass spectrum can be recorded for surface analysis of the outer 0.5 nm or so. This mode of operation is known as static SIMS. In dynamic SIMS, the intensity of one peak for one particular mass is recorded as a function of time as the



## Chapter 2

sample is sputtered at higher sputter rate (approximately 10  $\mu\text{m}$ ), depth profile. It is also possible to display the intensity of one peak as a two-dimensional image.

## 2.10 References

- [1] A. C. G. Mitchell and M. W. Zemansky, Resonance Radiation and Excited Atoms (Cambridge, London 1961).
- [2] S. Takashima, M. Hori, T. Goto, A. Kono, M. Ito and K. Yoneda, Appl. Phys. Lett. **75**, 3929 (1999).
- [3] S. Takashima, S. Arai, M. Hori, T. Goto, A. Kono, M. Ito, and K. Yoneda, J. Vac. Sci. Technol. A **19**, 599 (2001).
- [4] H. Nagai, M. Hiramatsu, M. Hori, and T. Goto, Rev. Sci. Instrum. **74**, 3453 (2003).
- [5] R. S. Freund, J. A. Schiavone, and D. F. Brader, J. Chem. Phys. **64**, 1122 (1976).
- [6] K. Ito, N. Oda, Y. Hatano, and T. Tsuoi, Chem. Phys. **21**, 203 (1977).
- [7] S. Djurovic and J. R. Roberts, J. Appl. Phys. **74**, 6558 (1993).
- [8] J. W. Corburn and M. Chen, J. Appl. Phys. **51**, 3134 (1980).
- [9] Y. Kawai, K. Sasaki, and K. Kadota, Jpn. J. Appl. Phys. **36**, L1261 (1997).
- [10] R. E. Walkup, K. L. Saenger, and G. S. Sewyn, J. Chem. Phys. **84**, 2668 (1986).
- [11] H. M Katsch, A. Tewes, E. Quandt, A. Goehlich, T. Kawetzki, and H. F. Dobe, J. Appl. Phys. **88**, 6232 (2000).
- [12] S. F. Durrant and M. A. B. Moraes, J. Vac. Sci. Technol. A, **13**, 2513 (1995).
- [13] S. F. Durrant and M. A. B. Moraes, J. Vac. Sci. Technol. A, **16**, 509 (1998).
- [14] A. Gicquel, M. Chenevier, Kh. Hassouni, A. Teserepi, and M. Dubus, J. Appl. Phys. **83**, 7504 (1998).
- [15] M. A. Lieberman and A. J. Lichtenberg: *Principles of Plasma Discharges and Materials Processing* (John Wiley & Sons, Inc. New York 1994).
- [16] H. Fujiwara, Spectroscopic Ellipsometry: Principles and Applications (Wiley, New York 2007).
- [17] P. R. Griffiths and J. A. de Haseth, Fourier Transform Infrared Spectrometry (Wiley, New York, 1986).

- [18] M. Nitschke, J. Meichsner, J. Appl. Polym. Sci., **65**, 381 (1997).
- [19] M. Tasumi, *FT-IR no kiso to jissai*, [Basic and Actually of FT-IR] (TOKYO KAGAKU DOZIN, Tokyo, 1998) [in Japanese]
- [20] Y. Gotoh, and S. Kajiura, Journal of Nuclear Materials, **266**, 1051 (1999).
- [21] J. Zhang, D. P. Wikinson, H. Wang, and Z. S. Liu, Electrochimica Acta, **50**, 4082 (2005).
- [22] J. Wei, J. Appl. Phys., **92**, 6525 (2002).
- [23] X. G. Li, K. L. Huang, S. Q. Liu, N. Tan, and L. Q. Chen, Trans. Nonferrous Met. Soc. China, **17**, 195 (2007).
- [24] A. Grill, V. Patel, K. P. Rodbell, E. Huang, M. R. Baklanov, K. P. Mogilnikov, M. Toney, and H. C. Kim, J. Appl. Phys. **94**, 3427 (2003).
- [25] A. A. Michelson, Phil. Mag., **31**, 256 (1891)
- [26] L. Raleigh, Phil. Mag., **34**, 407 (1892).
- [27] Rubens and Wood, Phil. Mag., **21**, 249 (1911).
- [28] Rubens and von Baeyer, Phil. Mag., **21**, 689 (1911).
- [29] D. K. Schroder, “*Semiconductor Materials and Device Characterization Third Edition*”, Wiley, New York, (2006).
- [30] K. Siegbahn, C. Nordling, A. Fahlman, R. Nordberg, K. Hamrin, J. Hedman, G. Johnsson, T. Bergmark, S.-E. Karisson, I. Lindgreen, B. Lindberg: ESCA: Atomic, Molecular, and Solid State Structure Studied by Means of Electron Spectroscopy. Almqvist and Wiksells, Uppsala 1967.
- [31] P. Auger, J. Phys. Radium **6**, 205 (1925).
- [32] K. Takeda, Y. Tomekawa, T. Shina, M. Ito, Y. Okamura, and N. Ishii, J. Appl. Phys. **43**, 7737 (2004).
- [33] C. Koshimizu, T. Ohta, T. Matsudo, S. Tuchitani, and M. Ito, Appl. Phys. Express **3**, 056201 (2010).
- [34] The Surface Science Society of Japan, “Niji ion sitsuryo bunseki hou [Secondary

Ion Mass Spectrometry]”, (Maruzen, Tokyo, 1999) [in Japanese].

[35] L. L. Thomson, Phil. Mag., **20**, 752 (1910).

## **Chapter 3      Precise Control of Etched Feature Profile of Low-*k* Organic Films Based on Control of Radical Densities and Substrate Temperature**

### **3.1 Introduction**

This Chapter describes control of feature profiles on plasma etch of organic films by a control of radical densities and real-time monitoring of substrate temperature.

In particular, the control of an etched pattern profile with an accuracy of approximately 5 nm must be achieved in the near future. It has been reported that high-density plasmas employing N<sub>2</sub>/H<sub>2</sub> gases have been used for etching low-*k* organic films without a large degradation in the film quality and etched profile. However, side etching, which causes bowing and microtrenching, occurs easily in low-*k* organic film [1-5].

In previous studies, the correlation among the behaviors of H and N radical densities and the etching characteristics of the low-*k* organic films was investigated. [4-9] From the results, it was found that H radicals are important etchant species for low-*k* organic film etching and N radicals were effective for the formation of protection layer on the sidewall of etched pattern against the etching due to H radicals. Moreover, it was clarified that etching characteristics of low-*k* organic film depend on H and N radical densities and the substrate temperature. The effect of ions on the low-*k* organic films have been proposed that NH<sub>x</sub><sup>+</sup> ions enhanced the etch rate and the modification of surfaces resulting in the formation of a CN layer that protects the organic film against chemical etching [3, 10-12].

In this Chapter, characteristics of the low-*k* organic films etching employing a 100 MHz excited capacitively coupled plasmas (CCP) reactor with a 2MHz biasing employing H<sub>2</sub> and N<sub>2</sub> mixture gases were investigated. In addition, H and N radical

densities were measured nearby the sidewall of reactor by the vacuum ultraviolet absorption spectroscopy (VUVAS) and the substrate temperature was monitored with high accuracy using a newly developed interferometer system during the plasma process for realizing the high precise process. We proposed a scheme to control a fine pattern profile of low- $k$  organic films precisely by controlling the radical density ratio temporally according to the change of the substrate temperature. We believe this technique can be applied for etching process of general organic materials also.

### 3.2 Experimental Details

Figure 3.1 shows a schematic diagram of 100 MHz CCP etcher with the VUVAS system and a substrate temperature measurement system. The 100 MHz CCP chamber was 300 mm in diameter. VHF (100 MHz) power was applied to an upper electrode that was 127 mm in diameter through a matching network and the 100 MHz CCP was generated in the chamber. The 2 MHz bias power was supplied to substrate which was 4 inches in diameter on a lower electrode. The gap between the upper electrode and the lower electrode was fixed to 35 mm. The process gases ( $H_2$  and  $N_2$ ) were fed from the upper electrode with a showerhead shape. A total pressure was maintained at 2.5 Pa during the plasma process. The Si wafer was placed on the lower electrode with an electrostatic chuck system. The lower electrode temperature was maintained by circulating coolant and filling of backside with helium. The low- $k$  organic films used in this study are SiLK™ (Dow Chemical), having a dielectric constant of 2.7, the good thermal stability (420 °C) and the good adhesion, as an low- $k$  organic film for the etching sample.

Information on the effects of H and N radicals in 100MHz CCP on the etching process of the low- $k$  organic film is useful for etching other low- $k$  organic films. In this study, we carried out H and N radical density measurements near the sidewall of the chamber to avoid disruption of the etching process. Vacuum ultraviolet (VUV) light from a microdischarge hollow-cathode lamp was absorbed by plasma while passing the sidewall of the chamber. The absorption length was 100 mm. VUV light was focused on the slit of a vacuum ultraviolet monochromator by a  $MgF_2$  lens and then detected by a photomultiplier tube. The signal was recorded with a digital oscilloscope and averaged using a personal computer. The transition line of the H atom used for the VUVAS measurement was a Lyman  $\alpha$  at 121.6 nm, and those of the N atom were  $^4P_{5/2}-^4S^0_{3/2}$ ,  $^4P_{3/2}-^4S^0_{3/2}$  and  $^4P_{1/2}-^4S^0_{3/2}$  at 120.0 nm of the N atom [13,14].

Substrate temperature was calculated from the change in the optical thickness of the Si wafer measured by an optical fiber-type low-coherence interferometer. The measurement system is based on a Michelson interferometer, which consists of a superluminescent diode (SLD), a reference mirror scanner, a fiber collimator, an optical fiber, and other components. SLD light is divided into two beams by the fiber coupler. One beam irradiates the substrate. The other beam goes to a scanning reference mirror. In the substrate, SLD light is reflected on the substrate back surface and front surface. On the reference mirror scanner side, the reference-optical-path length changes because the mirror is moved. Lights reflected at the substrate go back to the fiber coupler through the fiber collimator, interfering with the light reflected at the scanning reference mirror within the coherence length range. The position of the interferogram was changed by the thermal expansion and the change in refractive index of Si wafer with increasing substrate temperature. The change in temperature was measured from the shift in the peak position of the interferogram. By using the measurement system discussed here, we can measure substrate temperature in real time [15, 16].

Samples were prepared by the photolithographic patterning of Line/Space (65/65 nm) of SiO<sub>2</sub> hard mask on organic film. After etching of the hard mask, the photoresist films were remained because no ash-removal process was carried out. The patterned sample used in this experiment consists of SiO<sub>2</sub>/SiLK™/Si stacked structure. The thickness of the hard mask using SiO<sub>2</sub> was 125 nm and that of the organic film was 240 nm. Each etching time was set at 10 % over-etched time estimated from the etch rate. The etching profiles of the cross-section of the Line and Space pattern were observed using a scanning electron microscope (SEM, Hitachi, S-5200).

The surface analysis of the blanket low-*k* organic films by X-ray photoelectron spectroscopy (XPS, FISONS Escalab-220i) was carried out after the etch process of identical conditions for the patterned samples. XPS measurement was performed using Mg-*ka* radiation (1242.6 eV) with a scanning energy step of 0.1 eV. Chemical



compositions are obtained from the XPS profiles.

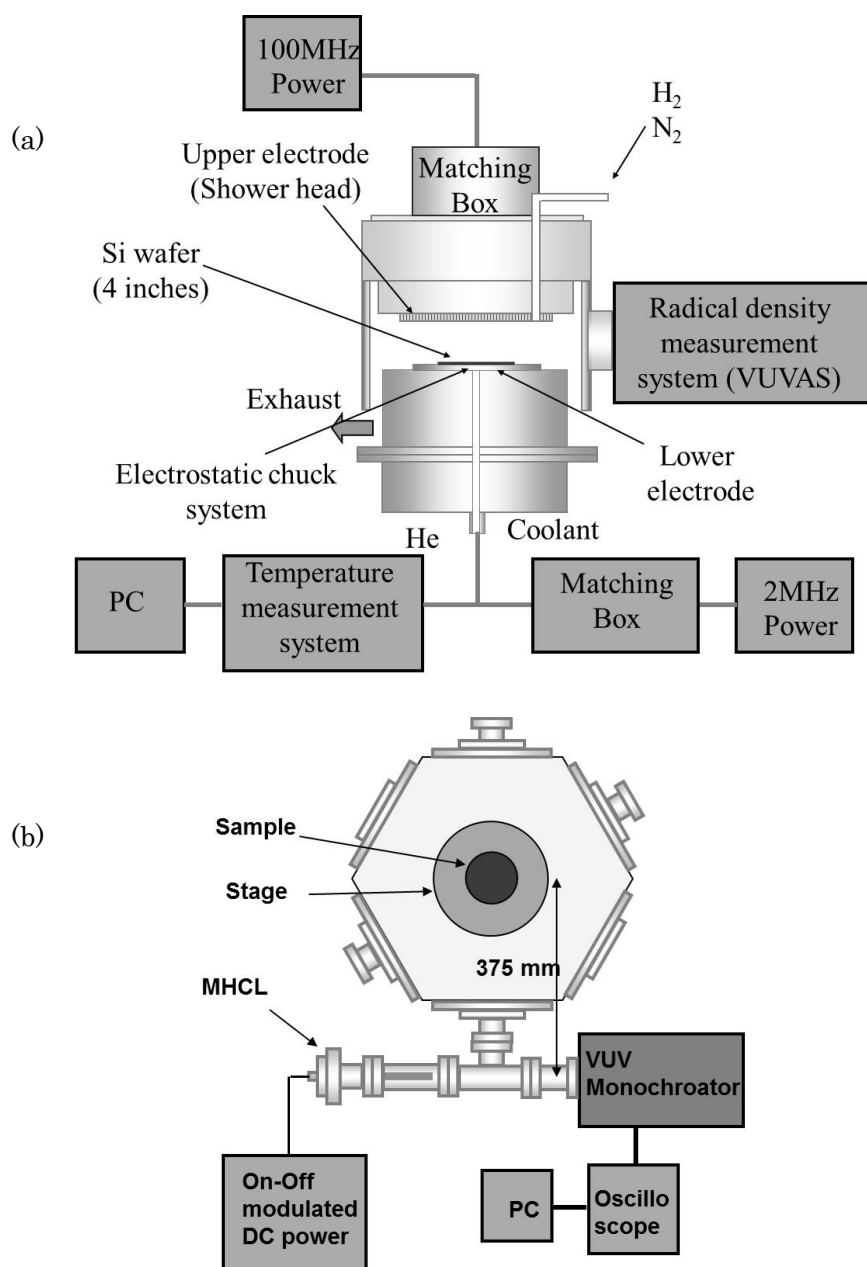


Fig. 3.1 Schematic diagram of (a) experimental setup: 100MHz/2MHz CCP etcher and (b) radical measurement system.

### 3.3 Results and Discussion

#### 3.3.1 Etch Rate and Electron Density

To clarify behaviors of etch rate and change of etched profiles, the plasma diagnostics were performed by a 35GHz microwave interferometer (NIHON-KOSHUHA, MPI-1035J) in H<sub>2</sub>/N<sub>2</sub> plasmas. Figure 3.2 shows etch rate and electron densities of the low-*k* organic film in N<sub>2</sub>/H<sub>2</sub> plasmas as functions of flow rate ratio of H<sub>2</sub>/(H<sub>2</sub>+N<sub>2</sub>). H<sub>2</sub>/N<sub>2</sub> plasmas were ignited in the CCP chamber at a substrate temperature of 20 °C, H<sub>2</sub> flow rate of 75 sccm, N<sub>2</sub> flow rate of 25 sccm, a total pressure of 2.5 pa, a VHF power of 450 W, and a self-bias voltage of -500 V. The electron density in the pure N<sub>2</sub> plasma was the highest. In the N<sub>2</sub>/H<sub>2</sub> plasmas, the electron density and the relative density of high-energy electrons were almost constant in spite of the change of flow rate ratio. The electron density drastically decreased in H<sub>2</sub> plasma. This might be due to the large total ionization cross section of N<sub>2</sub>, which is about 2.5 times larger than that of H<sub>2</sub> [5]. The etch rate had a maximum of 175 nm/min at H<sub>2</sub>/(H<sub>2</sub>+N<sub>2</sub>) = 75%. Figure 3.3 shows etch rate and electron densities of the low-*k* organic film in N<sub>2</sub>/H<sub>2</sub> plasmas as a function of 100 MHz power. The condition of plasma was a flow rate of H<sub>2</sub> of 75 sccm, a flow rate of N<sub>2</sub> of 25 sccm. The electron density and etch rate increased monotonically. Figure 3.4 shows etch rate and electron densities of the low-*k* organic film in H<sub>2</sub>/H<sub>2</sub> plasmas as a function of pressure. The electron densities were  $2.3 \times 10^{10} \text{ cm}^{-3}$  in the range 2.0 to 3.0 Pa. The electron density was low ( $2.3 \times 10^{10} \text{ cm}^{-3}$ ) at 1.5 Pa. the etch rate were 185 nm/min in the range 2.0 to 3.0 Pa. The change in etch rate was similar to that of electron density.

Quadruple mass spectroscopy has revealed the presence of other dominant ionic species, such as H<sup>+</sup>, H<sub>3</sub><sup>+</sup>, N<sup>+</sup>, NH<sub>2</sub><sup>+</sup>, NH<sub>3</sub><sup>+</sup>, NH<sub>4</sub><sup>+</sup>, N<sub>2</sub><sup>+</sup>, and N<sub>2</sub>H<sup>+</sup>, in similar H<sub>2</sub>/N<sub>2</sub> plasmas [4].

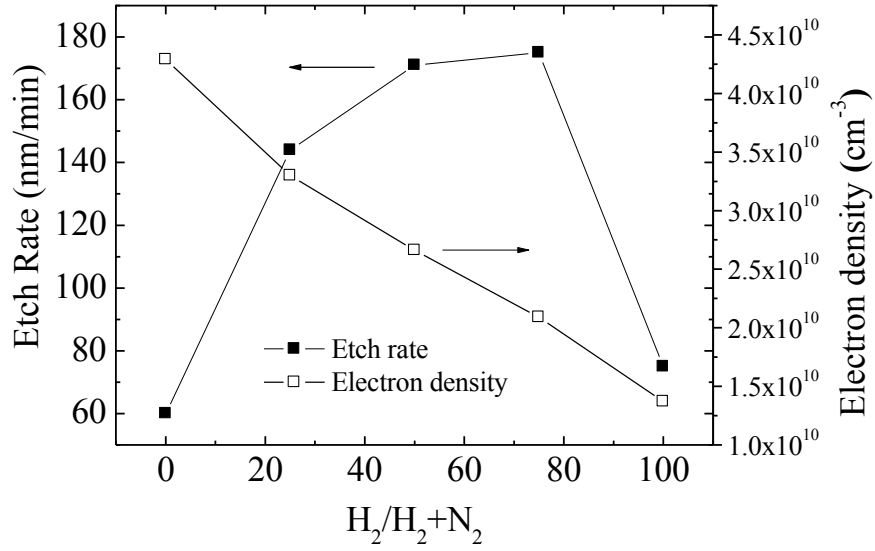


Fig. 3.2 Electron density and etch rate in  $H_2/N_2$  plasma as a function flow rate ratio of  $H_2/(H_2+N_2)$ .

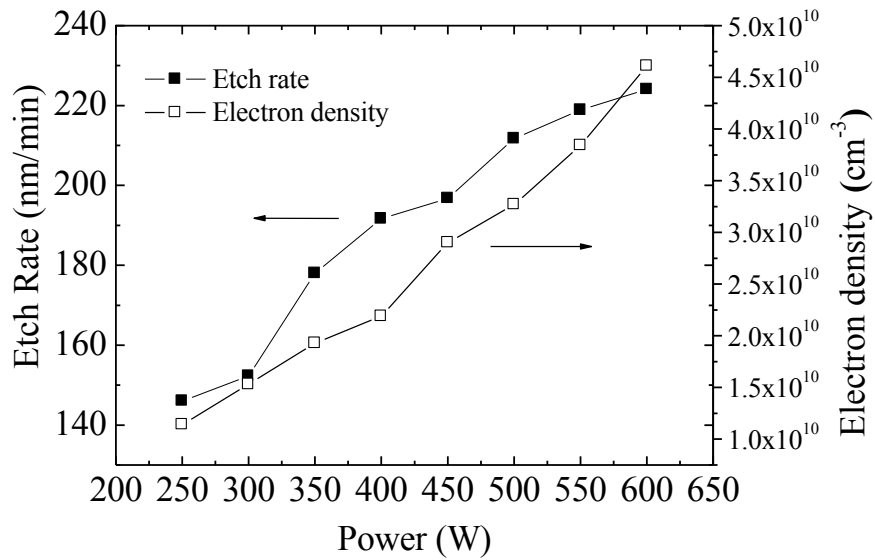


Fig. 3.3 Electron density and etch rate in  $H_2/N_2$  plasma as a function of VHF power.

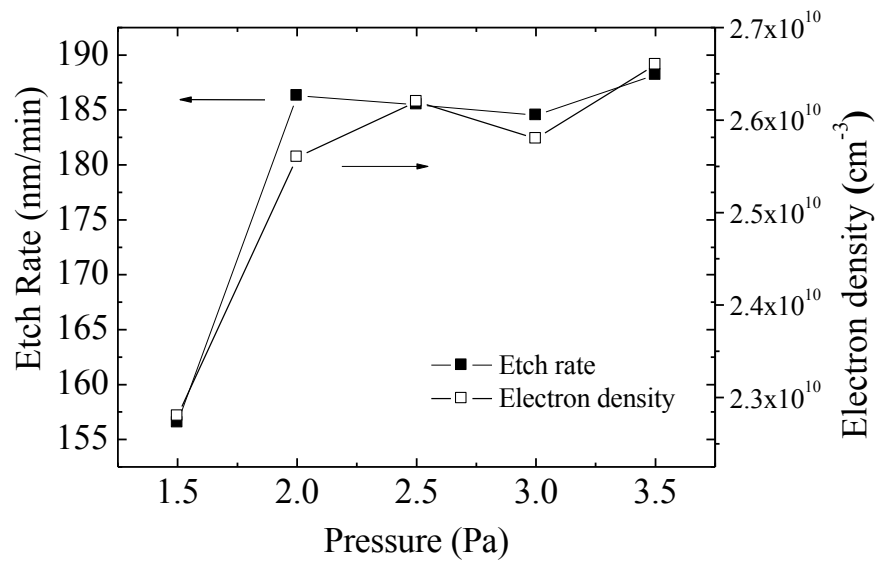


Fig. 3.4 Electron density and etch rate in H<sub>2</sub>/N<sub>2</sub> plasma as a function of pressure

### 3.3.2 Densities of Radicals in H<sub>2</sub>/N<sub>2</sub> Plasmas

Since previous studies in the inductively coupled plasma with 13.56MHz and ultrahigh frequency (UHF) 500MHz plasma showed that the etch rate and etched profiles could be controlled precisely by selecting the ratio of H and N radical densities and the substrate temperature, [4-6] H and N radical densities and substrate temperature were measured by VUVAS and a substrate temperature measurement system, respectively. H<sub>2</sub>/N<sub>2</sub> plasmas were ignited in the CCP chamber at a substrate temperature before igniting the plasma of 20 °C, a VHF power of 400 W, and a self-bias voltage of -500V. Figure 3.5 shows H and N radical densities as functions of flow rate ratio of H<sub>2</sub>/(H<sub>2</sub>+N<sub>2</sub>). H radical densities were estimated  $8.2 \times 10^{10} \text{ cm}^{-3}$  at H<sub>2</sub>/(H<sub>2</sub>+N<sub>2</sub>) = 10%. H radical densities increased with increasing the flow rate ratio of H<sub>2</sub>/(H<sub>2</sub>+N<sub>2</sub>) and reached the maximum of  $5.2 \times 10^{11} \text{ cm}^{-3}$  at H<sub>2</sub>/(H<sub>2</sub>+N<sub>2</sub>) = 75%, and then decreased near the pure H<sub>2</sub> plasma condition. With respect to this behavior of H density, the plasma density in nitrogen mixture plasma increased compared with that for pure hydrogen plasma. Nagai *et al.* reported that the dissociation of H<sub>2</sub> is enhanced by the addition of N<sub>2</sub> gas, since the total ionization cross section of N<sub>2</sub> is larger than that of H<sub>2</sub>, which leads to an increase in electron density [4]. On the other hand, N radical density was estimated  $2.0 \times 10^{11} \text{ cm}^{-3}$  at H<sub>2</sub>/(H<sub>2</sub>+N<sub>2</sub>) = 0%, and decreased with increasing the flow rate ratio of H<sub>2</sub>/(H<sub>2</sub>+N<sub>2</sub>).

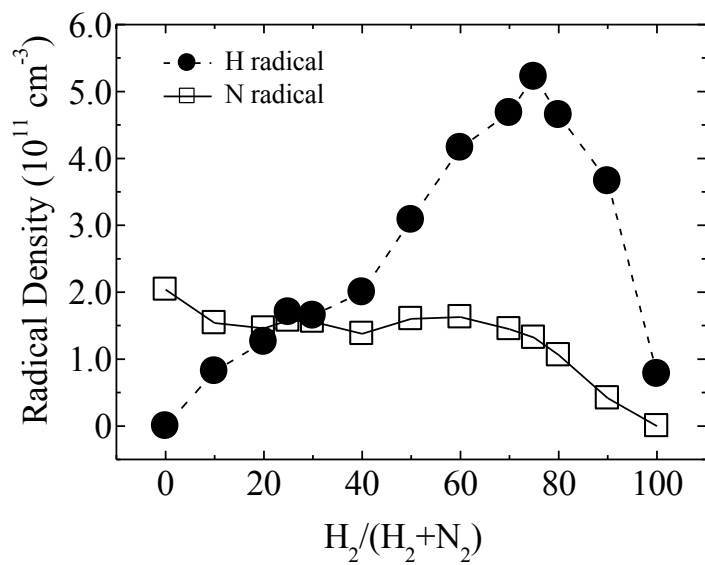


Fig. 3.5 H and N radical densities as a function of flow rate ratio  $H_2/(H_2+N_2)$ .

### 3.3.3 Substrate Temperatures

The substrate temperature was measured in real time using optical fiber-type low-coherence interferometer to investigate effects on the etched profile of low- $k$  organic films. Figure 3.6 shows the substrate temperature during the plasma process as a function of plasma exposure time for various ratios of H to N radical densities. The substrate temperature before the plasma exposure was 20 °C. It was found that substrate temperature increased rapidly immediately after the plasma discharge and then saturated. The amount of increase in substrate temperature by plasma exposure increased with increasing ratio of H/(H+N). When the ratio of H/(H+N) was 1.00, substrate temperature increased by more than 30 °C at 3 min exposure time, while it increased by approximately 20 °C when the ratio of H/(H+N) was 0. In the plasma of the H<sub>2</sub> and N<sub>2</sub> gas mixture, the higher the H<sub>2</sub> ratio, the higher the substrate temperature. It seemed that the difference in temperature between the gases caused a difference in substrate temperature.

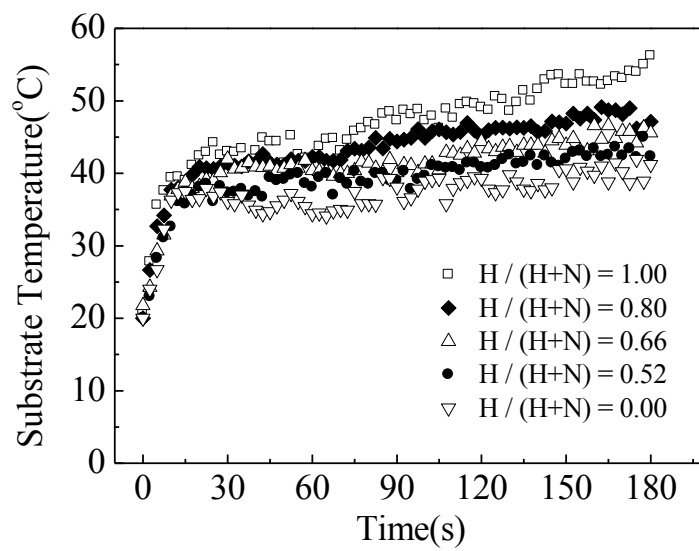


Fig. 3.6 Substrate temperature during various plasma processes as a function of plasma exposure time.



### 3.3.4 Etch Rates for Low- $k$ Organic Film

Low- $k$  organic film etching was performed at a total pressure of 2.0 Pa, a VHF power of 400 W, and a self-bias voltage of -500 V. Figures 3.7(a) and (b) show the etch rate of the organic film as functions of the H radical ratio of  $H/(H+N)$  at a substrate temperature of 24 °C and as a function of a substrate temperature at a ratio of  $H/(H+N) = 0.8$ , respectively. Substrate temperature was defined as the average substrate temperature after the saturation on the basis of the result in Fig. 3.6. The etch rate had a maximum of 175 nm/min at  $H/(H+N) = 0.8$ , as shown in Fig. 3.7(a). We note that this figure shows the etch rates when both VHF power and bias power were fixed at constant values, that is, only gas flow ratio was changed using mass-flow controllers. The larger ratio of hydrogen in the gas composition resulted in a low plasma density. Hence, the maximum etch rate was obtained at  $H/(H+N) = 0.8$ . Moreover, when the substrate temperature was 12 °C, the etch rate was 169 nm/min, and the etch rate increased to 196 nm/min with increasing the substrate temperature. As will be discussed later, since the hydrogen atom can spontaneously etch organic films, at higher densities of hydrogen atoms with  $H/(H+N) = 0.8$ , chemical reactions will predominate, i.e., a weak temperature dependence on etch rate will be observed. Figure 3.8 shows the amount of bowing of the organic film as a function of the substrate temperature at a ratio of  $H/(H+N) = 0.8$ . The amount of bowing is defined as the difference between the width at the highest bowing position or the most tapered position “B” and the width at the line at the top “A”, as shown in Fig. 3.8. (Note: To meet the requirements of the etch process, it is better to reduce the size of the trench bottom, B. Hence, if B is less than A, we always regard the data as the taper profile.) The amount of bowing slightly increased with increasing the substrate temperature. This change is important from the viewpoint of controlling the shape of sidewall.

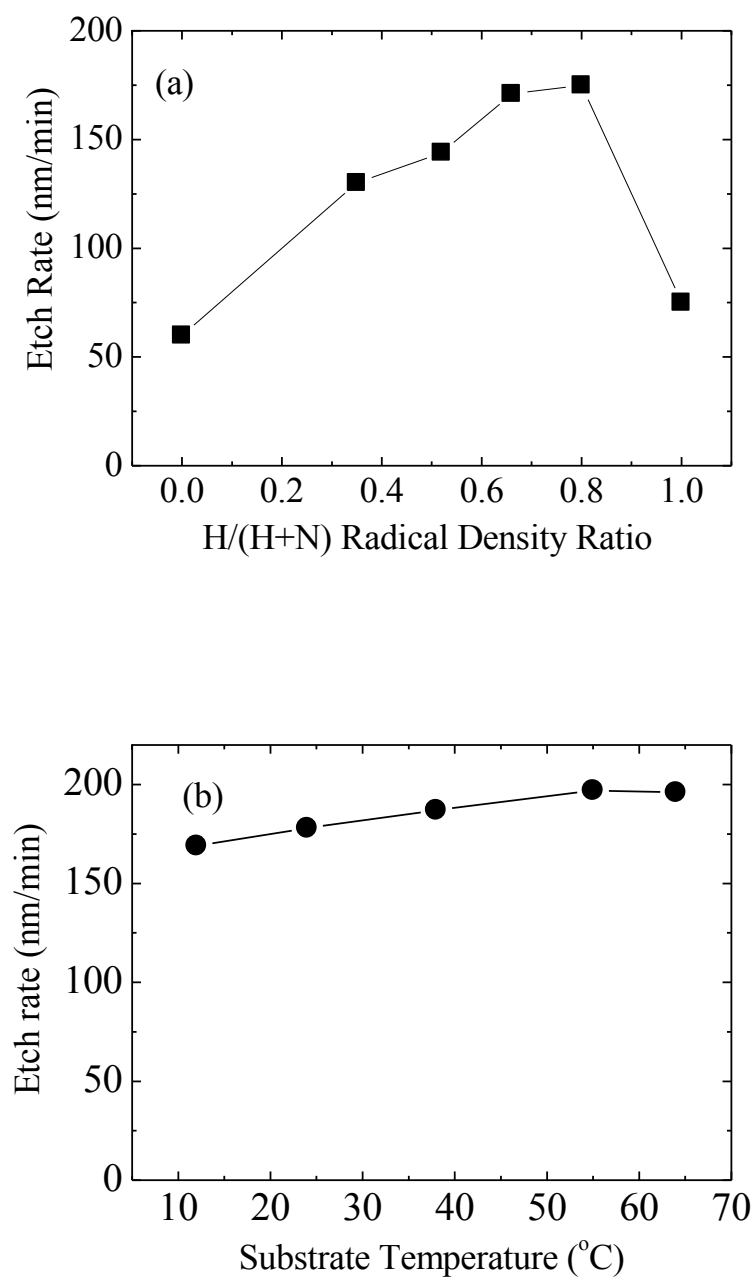


Fig. 3.7 Etch rate of organic film as functions of (a) H radical ratio of  $H/(H+N)$ , (b) substrate temperature.

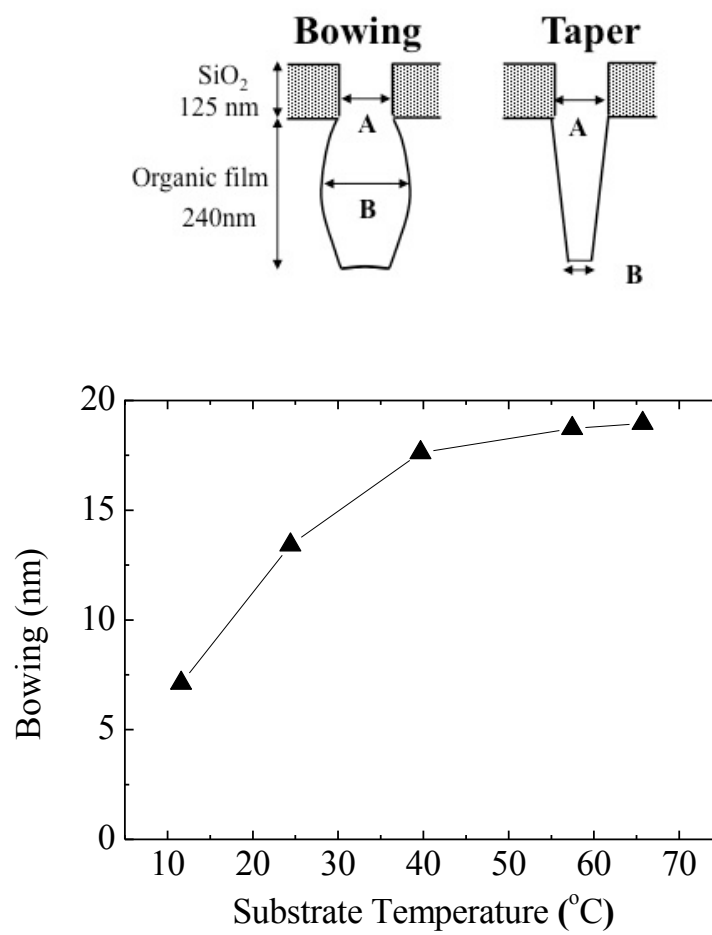


Fig. 3.8 Amount of bowing of organic film as a function of substrate temperature.

### 3.3.5 Etched Profile

Etched profiles have been investigated on the basis of the ratio of H and N radical densities and the substrate temperature. Figure 3.9 shows the amount of bowing at the sidewall of a trench as a function of substrate temperature in H<sub>2</sub>/N<sub>2</sub> plasma. Figure 3.10 shows cross-sectional SEM images of the etch profile of the 65nm line-and-space pattern of the organic film at H radical density ratios of (a) 0.80, (b) 0.68, (c) 0.52, (d) 0.35, and (d) 0 when the substrate temperature was 24 °C. Each etching time was set at 10% over-etched time estimated from the etch rate. (Note: In case of experiment (d), pure N<sub>2</sub> plasma etching, 10% over-etched time was not enough to reach to bottom of the pattern.) The bowing profile was not seen at any substrate temperature after N<sub>2</sub> plasma ( $H/(H+N) = 0$ ) etching; however, the amount of bowing increased with increasing substrate temperature except  $H/(H+N) = 0$ . These results show that the amount of bowing increased or the amount of taper decreased with increasing H radical density ratio and substrate temperature. However, a vertical profile was not obtained at any H ratio. Even under the conditions for setting the amount of bowing at nearly zero, the etch profile showed the profiles of both bowing and taper [Fig. 3.10(b)]. Even though this attempt was based on measurement of radical densities and the substrate temperature, we could not control featured profile within  $\pm 5$  nm. This result implies that a few more steps are required to realize highly precise etching of organic materials.

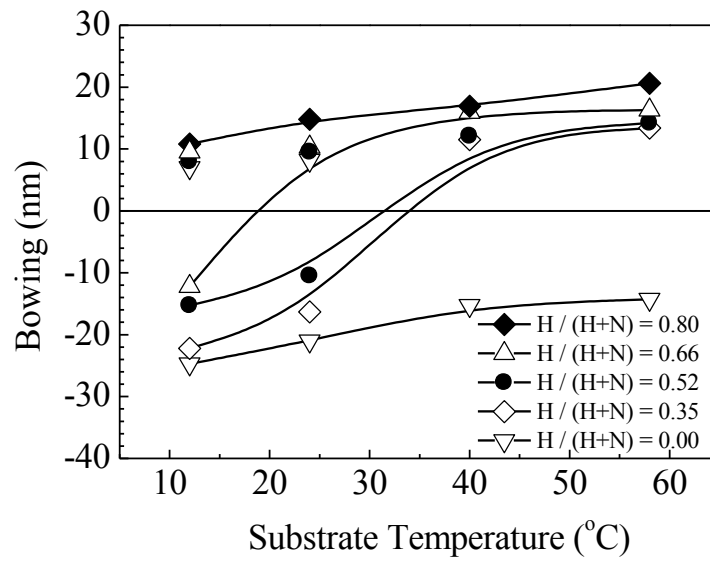


Fig. 3.9 Amount of bowing at sidewall of trench pattern as a function of substrate temperature.

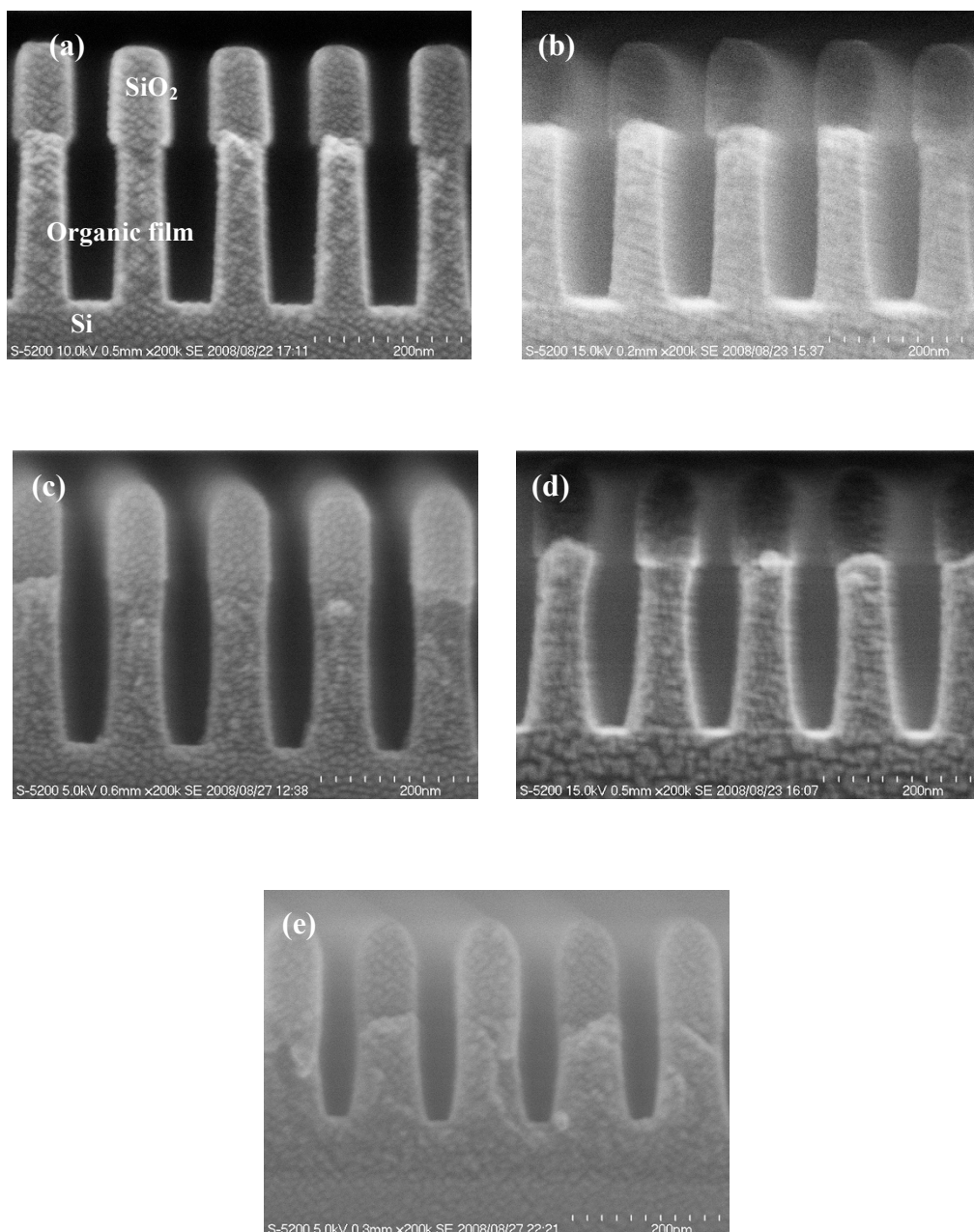


Fig. 3.10 SEM images of etched profile of organic film (a)  $H/(H+N) = 0.80$ , (b)  $H/(H+N) = 0.68$ , (c)  $H/(H+N) = 0.52$ , (d)  $H/(H+N) = 0.35$ , (e)  $H/(H+N) = 0.00$ .

### 3.3.6 Etch Process with a Temporal Control of Radical Density

From results shown in Fig. 3.9, we consider that the vertical profile could not be obtained under the constant radical ratio condition when the substrate temperature was varied as the etching evolution. We designed a new process that controls radical density ratio depending on substrate temperature step by step on the basis of the results shown in Figs. 3.9 and 3.10. Figure 3.11 shows the change in substrate temperature as a function of plasma exposure time at a ratio of  $H/(H+N) = 0.8$ . The substrate temperature before plasma exposure was 5 °C. From these results, the substrate temperature was 17, 22, and 25 °C after the plasma exposure for 10, 40, and 70 s, respectively. On the basis of these results, the appropriate H radical density ratio for obtaining the vertical profile was estimated. Consequently, etching conditions were changed to realize the vertical profile as follows: H radical density ratio was set at (A) 0.80, (B) 0.68, (C) 0.52, and (D) 0.35, when the plasma exposure time ranges were (A) from 0 to 10 s, (B) from 10 to 40 s, (C) from 40 to 70 s, and (D) from 70 s to the end point, respectively, as shown in Fig. 3.11 at a substrate temperature of 5 °C before the plasma exposure. Figure 3.12 shows SEM images of etched the profile of the organic film after the new process where radical density ratio was changed depending on substrate temperature. Comparing the results shown in Fig. 3.12 with those in Figs. 3.10 (a) and (b), the amount of bowing decreased considerably in the case of the new process and we have successfully achieved an almost vertical profile.

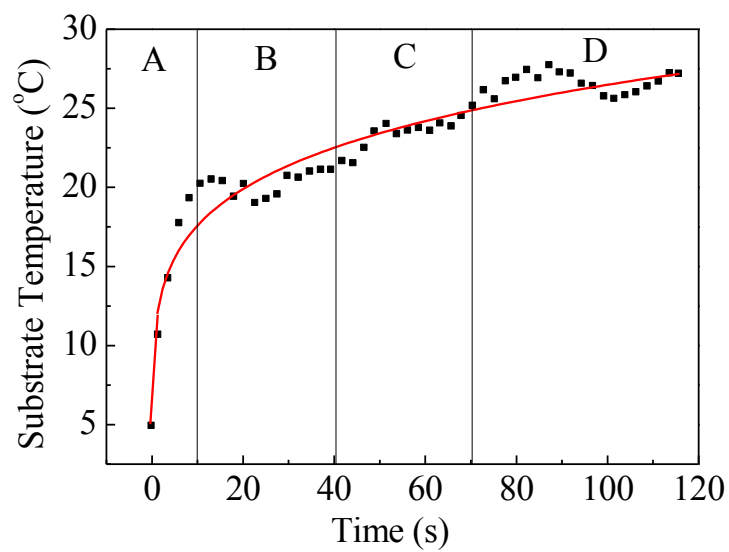


Fig. 3.11 Substrate temperature during new plasma processes that varied the radical density ratio as a function of plasma exposure time.

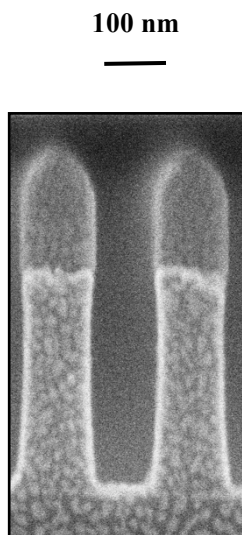


Fig. 3.12 SEM images of etched profile of organic film after new plasma process.



### 3.3.7 X-ray Photoelectron Spectroscopic Analyses on Etched Surface

In order to investigate the relation between Si substrate temperature and sidewall etching, XPS analysis was performed on the organic film after N<sub>2</sub> plasma exposure. In this section, blanket low-*k* organic film etch was performed at a total pressure of 2.0 Pa, a VHF power of 400 W, and a bias power of 0 W for simulating sidewall condition. Figure 3.13 shows atomic concentration of the organic films after pure N<sub>2</sub> plasma exposure at Si substrate temperature of (a) 4 °C and (b) 54 °C calculated from XPS spectra. With increasing take-off angle of X-ray, the concentration of C decreased and that of O increased in both samples. The concentration of N increased only in sample (a) at take-off angle of 80°. Figure 3.14 shows the variation of the N/C ratio of the low-*k* organic films after N<sub>2</sub> plasma exposure for 120 s at the substrate temperature of 4 °C and 54 °C calculated from XPS spectra. With increasing take-off angle of photoelectron, the N/C ratio increased in both samples. The amount of increase of N/C ratio at lower substrate temperature was higher than that at higher temperature. This result indicates that nitride layer formed on the low-*k* organic films during the N<sub>2</sub> plasma exposure at lower substrate temperature is thicker than that at higher temperature.

Figure 3.15 shows the XPS C1s spectra of the low-*k* organic film surface exposed to N<sub>2</sub> plasma for 120 s at substrate temperatures of (a) 4 °C and (b) 54 °C. On the spectrum of the initial films before the plasma etch, no shoulder arose from the chemical shift for carbon-nitrogen bonding and no signal from N 1s was observed. Note that on the spectra taken after the plasma etch, peak shifts attributed to C-O (288.3 eV), sp<sup>3</sup> C-N (288.7 eV), sp<sup>2</sup> C=N (286.0 eV), and C-C (285.0 eV) were detected [16-18]. From these results, CN layer was formed on the surface by exposed to N<sub>2</sub> plasma. Figure 3.16 shows the XPS N1s spectra of the low-*k* organic film surface exposed to N<sub>2</sub> plasma for 120 s at substrate temperatures of 4 °C and 54 °C. The N1s spectra of the

sample exposed to N<sub>2</sub> plasma have a broad peak corresponding to bonding configurations related to nitrogen atoms. The N1s peak consists of three contributions. The contributions corresponded to CN layer, which were attributed to sp<sup>3</sup> N-C (398.5 eV), sp<sup>2</sup> N=C (400.0 eV) and N-O (402.0 eV). The figure showed dominant peak is N-O bonds since the exposure of modified material to the atmosphere can then amplify the formation of N-O into the modified top surface (note: XPS measurement was carried out *ex situ*). These spectra were obtained at take-off angles of 80°.

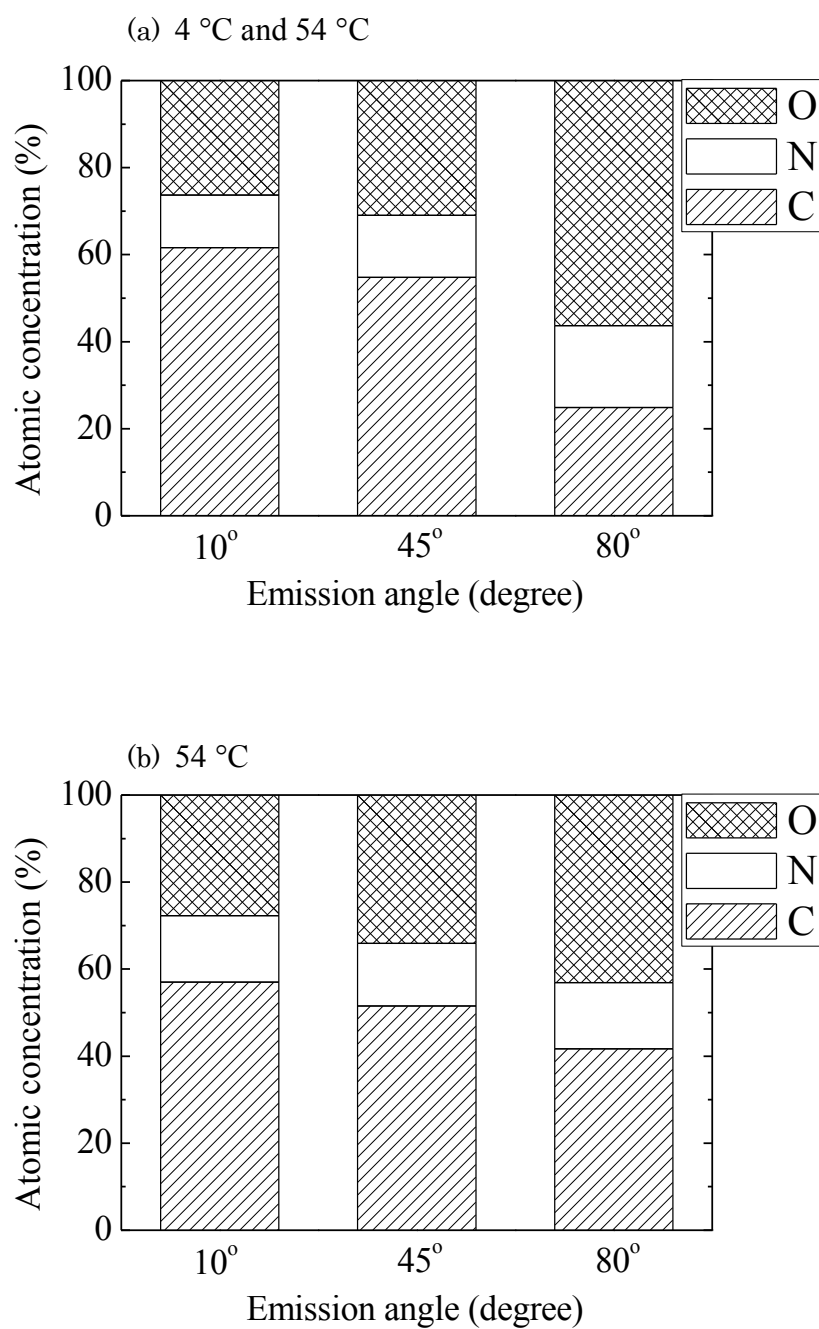


Fig. 3.13 Atomic concentration of organic films after N<sub>2</sub> plasma exposure at Si substrate temperature of (a) 4 °C and (b) 54 °C calculated from XPS spectra.

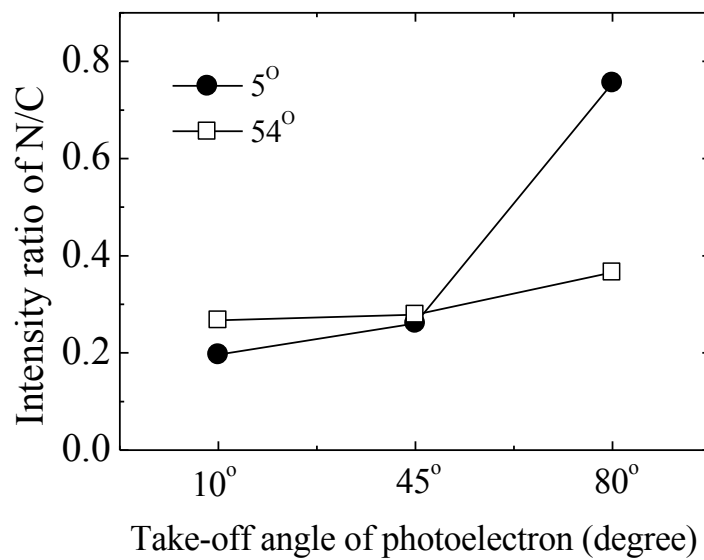


Fig. 3.14 Variation of N/C ratio of organic films as a function of take-off angle measured by XPS.

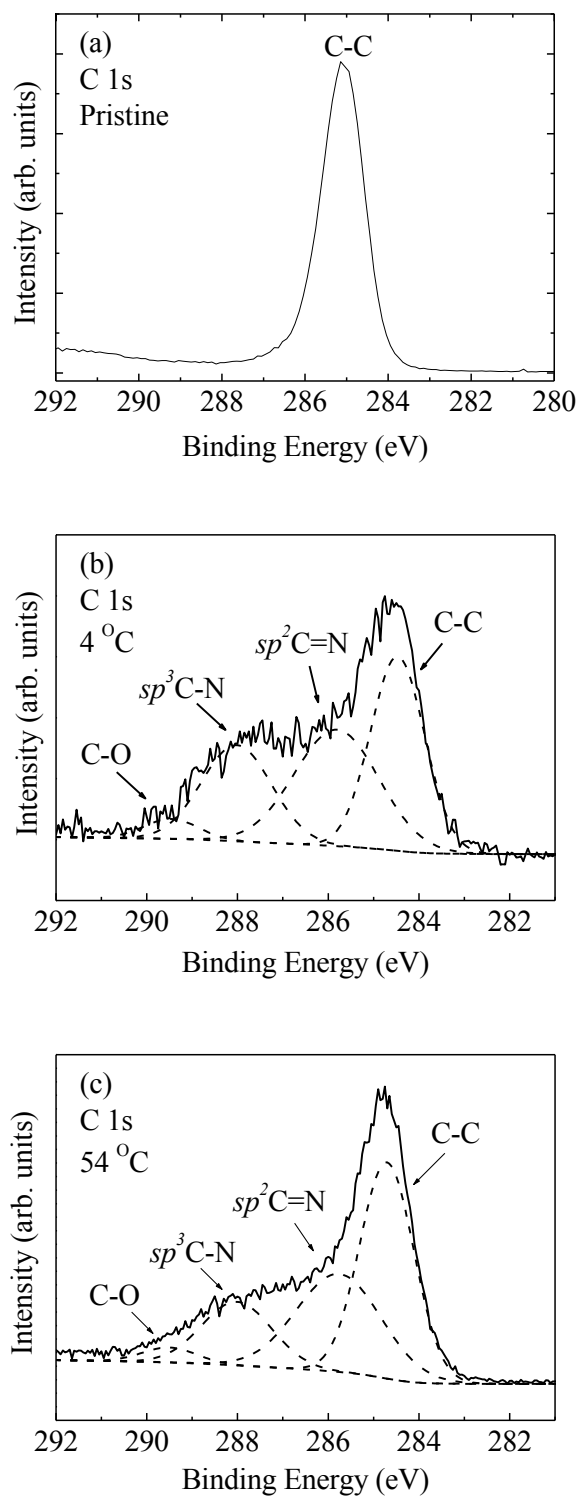


Fig. 3.15 C1s spectra of (a) pristine sample and sample surface exposed to N<sub>2</sub> plasma at Si substrate temperature of (b) 4 °C and (c) 54 °C.

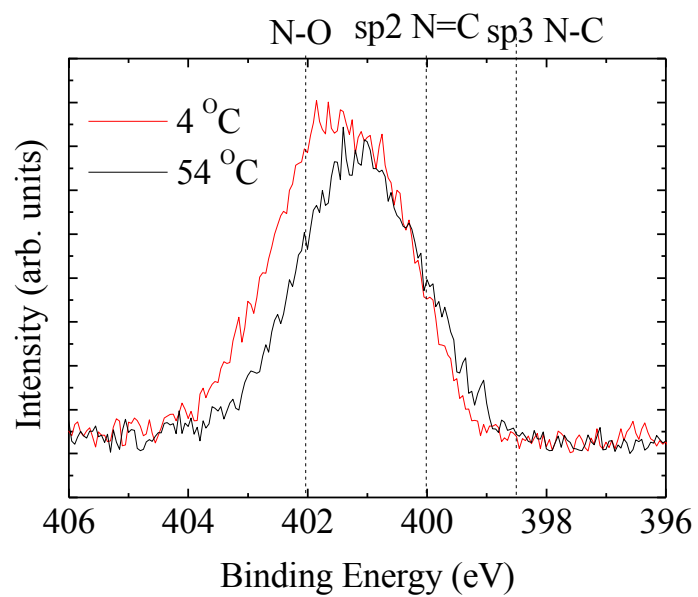


Fig. 3.16 N1s spectra of sample surface exposed to N<sub>2</sub> plasma at Si substrate temperature of 4 °C and 54 °C.

Figure 3.17 shows the percentages of C–O, sp<sup>3</sup> C–N, sp<sup>2</sup> C=N, and C–C concentrations of the surface components. C–N/C–C ratio decreased with increasing substrate temperature. The signal intensities of sp<sup>3</sup> C–N and sp<sup>2</sup> C=N bonds increased after the plasma exposure in the experiment. These results indicate that the nitride layers that formed on low-*k* organic films by the N<sub>2</sub> plasma exposure at lower substrate temperatures are thicker than those by the N<sub>2</sub> plasma exposure at higher substrate temperatures. Since previous works showed that sp<sup>3</sup> C–N bonds inhibit sidewall etching owing to H radicals [4,6], we conclude that a higher concentration of sp<sup>3</sup> C–N bonds formed at lower substrate temperatures leads to less damage to organic films during a plasma process.

To investigate the relationship between the formation of nitride layer and the etch rate on the sidewall, the etching rate of low-*k* organic films by H<sub>2</sub> plasma exposure with or without previous N<sub>2</sub> plasma treatment was measured, and the results are shown in Fig. 3.18. The plasma etching was performed at a total pressure of 2.0 Pa, a VHF power of 400 W, and a bias voltage of -500 V. The etch rate of the low-*k* organic films treated with N<sub>2</sub> plasma. The etching rate of the low-*k* organic films using H<sub>2</sub> plasma after N<sub>2</sub> plasma treatment at a substrate temperature of 4 °C is smaller than that at a substrate temperature of 54 °C. Under the conditions of N<sub>2</sub> plasma exposure at a high substrate temperature, the protective effect of the nitride layer was weak. These results also support the conclusion that nitride layers formed on the sidewall at low substrate temperatures protect organic films against etching.

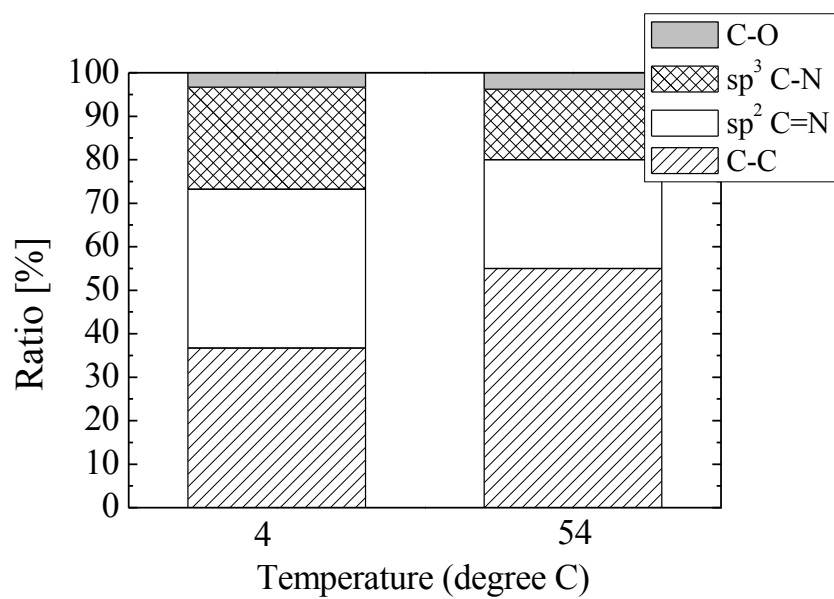


Fig. 3.17 Ratio of C-O, C-N, and C-C bond of organic film as a function of substrate temperature.

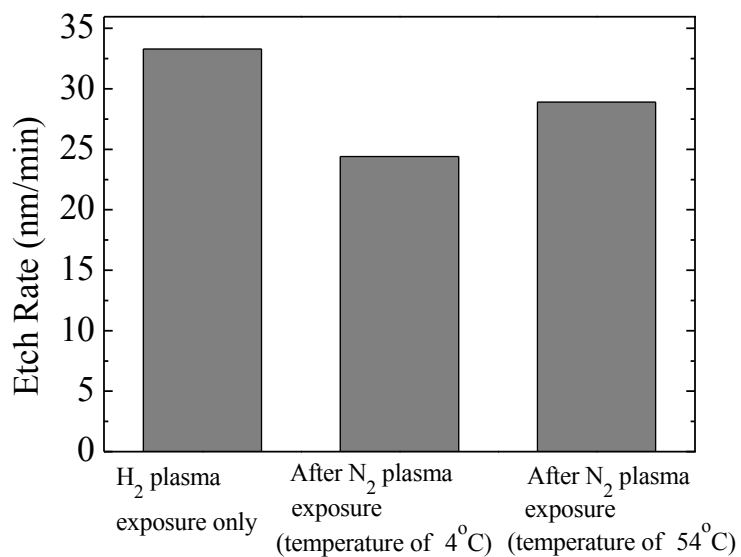


Fig. 3.18 Etch rate of organic film by  $H_2$  plasma exposure.



### 3.4 Conclusion

Low- $k$  organic films were etched using a dual-frequency CCP etching reactor employing a gas mixture of  $H_2/N_2$ . Absolute H and N radical densities were measured by VUVAS, and substrate temperature was measured using an optical-fiber-type low-coherence interferometer during precise low- $k$  organic film etching. We have successfully measured substrate temperature in real time during the etching process. It was found that substrate temperature increased with increasing H radical density ratio of  $H/(H+N)$ . On the basis of these measurements, the etching profiles of low- $k$  organic films were investigated. Using the results, we developed a new process that controls radical density ratio depending on substrate temperature step by step.

The amount of bowing on the sidewall decreased markedly with the new process. XPS analysis confirmed that nitride layers formed at low substrate temperatures by nitrogen-related species protect films against sidewall etching. We have succeeded in the control of the etched feature profile of low- $k$  organic films precisely using internal parameters of plasma processing even though the organic materials have mechanical and chemical instability. However, Uchida *et al.* pointed out that modification of the low- $k$  organic films were considerably less than that of porous low- $k$  films. We investigated that kind of problem on the porous low- $k$  material in next Chapter.

### 3.5 References

- [1] M. Fukasawa, T. Hasegawa, S. Hirano, and S. Kadomura, in Proceedings of Symposium on Dry Process, Waseda University, Tokyo, Japan (1998) pp. 175.
- [2] M. Fukasawa, T. Tatsumi, T. Hasegawa, S. Hirano, K. Miyata, and S. Kadomura, in Proceedings of Symposium on Dry Process, Waseda University, Tokyo, Japan (1999) pp. 221.
- [3] Y. Morikawa, S. Yasunami, W. Chan, T. Hayashi, and T. Uchida, J. Vac. Sci. Technol. A **19**, 1747 (2001).
- [4] H. Nagai, S. Takashima, M. Hiramatsu, M. Hori, and T. Goto, J. Appl. Phys. **91**, 2615 (2002).
- [5] H. Nagai, M. Hiramatsu, M. Hori, and T. Goto, J. Appl. Phys., **94**, 1362 (2003).
- [6] S. Uchida, S. Takashima, M. Hori, and M. Fukasawa, Jpn. J. Appl. Phys. **47**, 3621 (2008).
- [7] H. Nagai, Ph.D. Thesis, 2003, Department of Quantum Engineering, Nagoya University, Nagoya, Japan.
- [8] C. S. Moon, K. Takeda, M. Sekine, Y. Setsuhara, M. Shiratani, and M. Hori, J. Appl. Phys. **107**, 113310 (2010).
- [9] C. S. Moon, K. Takeda, M. Sekine, Y. Setsuhara, M. Shiratani, and M. Hori, Appl. Phys. Express **2**, 096001 (2009).
- [10] Y. Yamaoka, K. Kurihara, K. Karahashi, M. Sekine, and M. Nakamura, Extended Abstracts of the Electrochemical Society 201st Meeting (ECS2002 Spring), Philadelphia, PA, 2002, p. 410.
- [11] Y. Morikawa, T. Hayashi, and T. Uchida, Jpn. J. Appl. Phys. Part 1 **42**, 1441 (2003).
- [12] K. Ishikawa, Y. Yamaoka, M. Nakamura, U. Yamazaki, Y. Ishikawa, and S. Samukawa, J. Appl. Phys. **99**, 083305 (2006).

- [13] S. Takashima, A. Kono, M. Ito, K. Yoneda, M. Hori and T. Goto, Appl. Phys. Lett. **75** (25), 3929 (1999).
- [14] S. Takashima, S. Arai, A. Kono, M. Ito, K. Yoneda, M. Hori and T. Goto, J. Vac. Sci. Technol. A **19**, 599 (2001).
- [15] K. Takeda, Y. Tomekawa, T. Shina, M. Ito, Y. Okamura, and N. Ishii, Jpn. J. Appl. Phys. **43**, 773 (2004).
- [16] C. Koshimizu, T. Ohta, T. Matsudo, S. Tsuchitani, and M. Ito, Appl. Phys. Express **3**, 056201 (2010).
- [17] D. Marton, K. J. Boyd, A. H. Al-Bayati, S. S. Todorov, and J. W. Rabalais: Phys. Rev. Lett. **73**, 118 (1994).
- [18] K. J. Boyd, D. Marton, S. S. Todorov, A. H. Al-Bayati, J. Kulik, R. A. Zuhr, and J. W. Rabalais: J. Vac. Sci. Technol. A **13**, 2110 (1995).
- [19] S. Bhattacharyya, C. Cardinaud, and G. Turban: J. Appl. Phys. **83**, 4491 (1998).
- [20] S. Uchida, S. Takashima, M. Hori, M. Fukasawa, K. Ohshima, K. Nagahata, and T. Tatsumi, Jpn. J. Appl. Phys. **47**, 3621 (2008).



## **Chapter 4 Investigation of Effect of Remained Fluorocarbon Layer and Air Exposure after Plasma Exposure on Low- $k$ Porous SiOCH Films**

### **4.1 Introduction**

This Chapter describes effect of remained fluorocarbon (CF) layer and air exposure after plasma exposure on porous low- $k$  SiOCH films. Main integration difficulties of the porous low- $k$  materials are their sensitivity to plasma exposures leading to a change of the film structural properties. Electrical performance and reliability of the porous low- $k$  materials are degraded when they are exposed to plasma processes such as etching and ashing during microfabrication [1]. Many research groups investigated degradation mechanism of the porous low- $k$  films induced by plasma processes by *ex situ* analysis. Those studies provided us useful information to understand plasma damage mechanism. However those studied assume that surface modification caused by exposure to air after plasma processes is negligible compared with that caused by plasma exposure [1-10]. The low- $k$  films were characterized by spectroscopic ellipsometry, Fourier-transform infrared reflection absorption spectroscopy (FTIR-RAS), and chemical composition was investigated using the *ex situ* XPS. Vacuum ultraviolet absorption spectroscopy (VUVAS) was used to measure the H and N radical densities in the plasmas. The low- $k$  films are exposed to various plasmas through ULSI manufacturing processes. After a plasma etching process using fluorocarbon plasma, a CF layer is formed on the low- $k$  film surface. We investigated the effect of the CF layer during H<sub>2</sub> or N<sub>2</sub> ashing plasma exposure.

## 4.2 Experimental Details

Effect of fluorocarbon (CF) layer remained after low- $k$  etching process. The SiOCH low- $k$  film was exposed to a 60 MHz excited capacitively coupled plasma (CCP) for depositing a CF layer as shown in Fig. 4.1. This 60 MHz CCP chamber is different from the 100 MHz CCP chamber used for igniting ash plasma since the fluorocarbon gases have never been introduced to the 100 MHz CCP chamber in order to avoid a memory effect due to a CF film deposition on the chamber walls. The CF layer was deposited on the porous SiOCH films in fluorocarbon-based plasmas ( $C_4F_8/Ar$ ). In this CF layer deposition process, pressure, a 60 MHz power, substrate temperature, and flow ratio of  $C_4F_8/Ar$  was 5.0 Pa, 500 W, 20 °C, 10/500 sccm, respectively. We investigated Si-CH<sub>3</sub> bond using the *in situ* FTIR-RAS and chemical composition using the *ex situ* XPS on the porous SiOCH films with or without the CF layer during the H<sub>2</sub> or N<sub>2</sub> plasma exposure. In this ashing plasma exposure process, the pressure, the 100 MHz power, the substrate temperature, and the flow ratio of H<sub>2</sub> or N<sub>2</sub> were 2.5Pa, 450 W, 20 °C, 100 sccm, respectively.

The ash plasma processes were performed in a parallel-plate capacitively coupled plasma (CCP) chamber excited by very high frequency (VHF) radiation with a frequency of 100 MHz (See Fig. 3.1). To generate a plasma, VHF power was applied to the upper electrode through a matching network. The lower electrode was floating. The H<sub>2</sub> and N<sub>2</sub> gases were fed from the upper electrode through a showerhead electrode. A total gas flow is 100 sccm. A Si wafer was placed on the lower electrode with an electrostatic chuck system. The lower electrode temperature was controlled by solvent cooling. Helium was introduced between the electrode and the wafer (He backside cooling) to improve heat transfer. The thickness of porous SiOCH film ( $k = 2.3$ , approximately 40% porosity) was 75 nm and the refractive index at 633 nm was 1.31.

An *in situ* spectroscopic ellipsometer and FTIR and VUVAS systems were

installed in the chamber. The thickness and the refractive index at 633 nm of the porous SiOCH films were measured by *in situ* spectroscopic ellipsometry (M-2000F, JA Woollam). A single-layer Cauchy model was used to fit the ellipsometry data. Actual data were improved to fit based on two layer model but ambiguities in parameters such as each layer thickness, the Cauchy coefficients will be irreversible issued. Here for simplification, we assumed to be the model of single layer. The refractive index is related to the dielectric constant as  $\varepsilon(\lambda) = n(\lambda)^2 + k(\lambda)^2$ , where  $\varepsilon$  is the relative dielectric constant,  $\lambda$  is the wavelength, and  $n$  and  $k$  are respectively the real and imaginary parts of the refractive index.

Chemical bond structures in the porous SiOCH films were analyzed by *in situ* FTIR-RAS (Thermo Scientific, Nicolet-8700). FTIR-RAS spectra were recorded between 400 and 4000  $\text{cm}^{-1}$  with a spectral resolution of 4  $\text{cm}^{-1}$  by averaging 500 scans. FTIR-RAS spectra presented in this study were not normalized with respect to the SiOCH film thickness since film shrinkage may occur [5].

To measure the H and N radical densities in the ashing plasma, VUVAS was performed using a microdischarge hollow-cathode lamp close to the chamber sidewall to prevent disturbing the plasma [11–15].

The Si substrate temperature was measured by a temperature measurement system that employs low-coherence interferometry [16]. This system enabled us to estimate the Si wafer temperature during plasma processes by measuring the light path length in the Si wafer, which varied due to thermal expansion and changes in the refractive index.

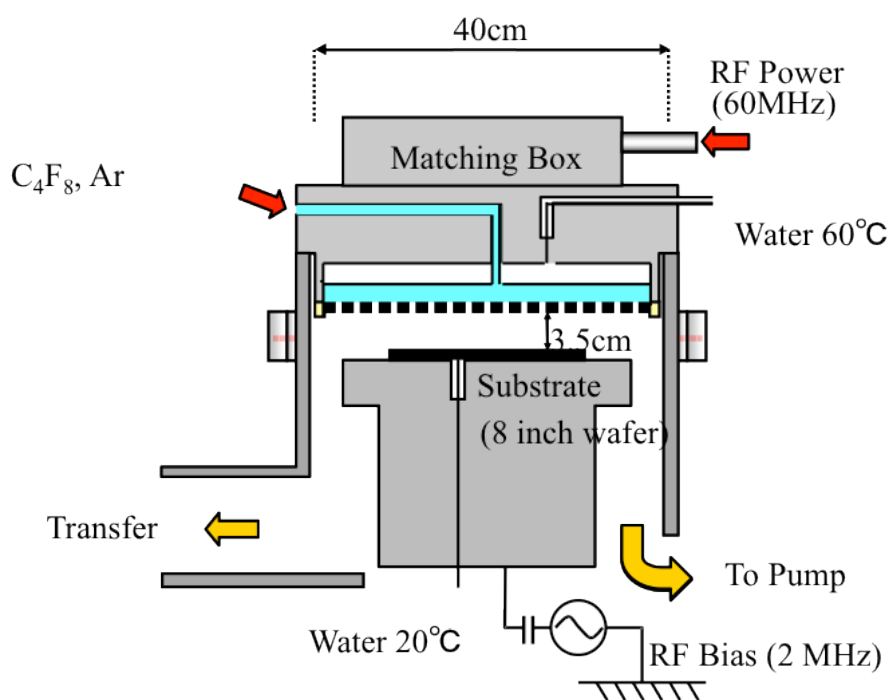


Fig. 4.1 Schematic diagram of 60MHz/2MHz CCP etcher.



## 4.3 Results and Discussion

### 4.3.1 Ashing Rate

Resist stripping (ashing) was performed by  $H_2$ ,  $H_2/N_2$  (1:1), and  $N_2$  plasma at a total pressure of 2.5 Pa, a 100MHz power of 450 W, a 2MHz bias power of 250 W, and a substrate temperature of 20 °C. Figure 4.2 shows ash rate by  $H_2$ ,  $H_2/N_2$ , and  $N_2$  plasma. The ash rate was calculated based on cross-sectional SEM image of blanket ArF photoresist. The ash rate of  $H_2$ ,  $H_2/N_2$ , and  $N_2$  plasma were 88.3, 248, 98 nm, respectively. These behaviors of etch rates are similar to the results of the etch rate of low- $k$  organic films discussed in Chapter 3.

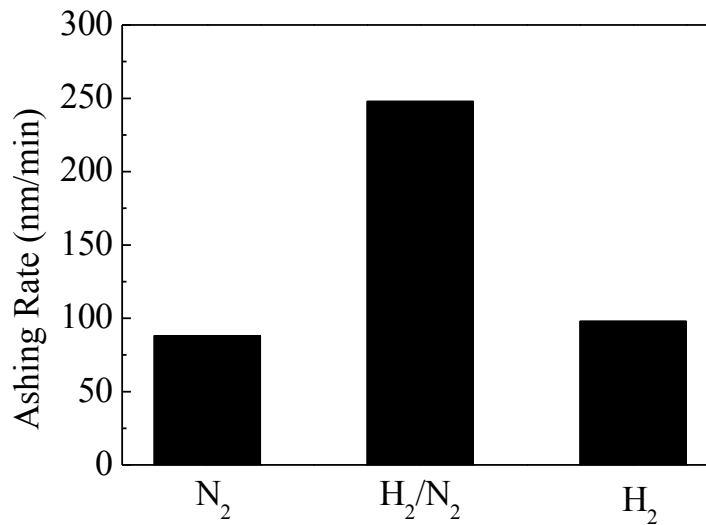


Fig. 4.2 Ash rate as a function of  $H_2$  flow rate ratio  $H_2/(H_2+N_2)$ .

#### 4.3.2 Modification by Air Exposure after Plasma Exposure

To investigate the effect of air exposure on damaged the porous SiOCH films after plasma exposure, modifications to films were examined by *in situ* spectroscopic ellipsometry and FTIR-RAS spectroscopy after exposure to H<sub>2</sub>, H<sub>2</sub>/N<sub>2</sub>, and N<sub>2</sub> plasma for 60 s and after exposure to air for 2 h. Measurement position for all tests were center of the samples. Figure 4.3 shows the variation in the refractive index after H<sub>2</sub>, H<sub>2</sub>/N<sub>2</sub>, and N<sub>2</sub> plasma exposure for 60 s and subsequent air exposure. The refractive index of all samples increased after the plasma exposures and it increased further on air exposure. FTIR-RAS analysis indicates that the porous SiOCH films have absorption bands between 3200 and 3700 cm<sup>-1</sup> (attributed to the Si-OH bond and H<sub>2</sub>O), between 2850 and 3000 cm<sup>-1</sup> (attributed to the CH<sub>x</sub> bond), at 1275 cm<sup>-1</sup> (attributed to the Si-CH<sub>3</sub> bond), and between 1000 and 1250 cm<sup>-1</sup> (attributed to the Si-O-Si bond) (see Figs. 4.4 (A) and (B)) [17]. The Si-NH<sub>2</sub>, Si-OH, and H<sub>2</sub>O peak intensities increase after H<sub>2</sub>/N<sub>2</sub> plasma exposure and are further enhanced after air exposure. The Si-O-Si peak was shifted after H<sub>2</sub>/N<sub>2</sub> plasma exposure and after air exposure. These results reveal that exposing the porous SiOCH films to air after plasma processes modifies the films. Based on these results, we conclude that the effect of plasma exposure and air exposure should be discussed separately and *in situ* analysis is critical for accurately investigating the plasma damage mechanism. The details of effects of air exposure will be discussed later.

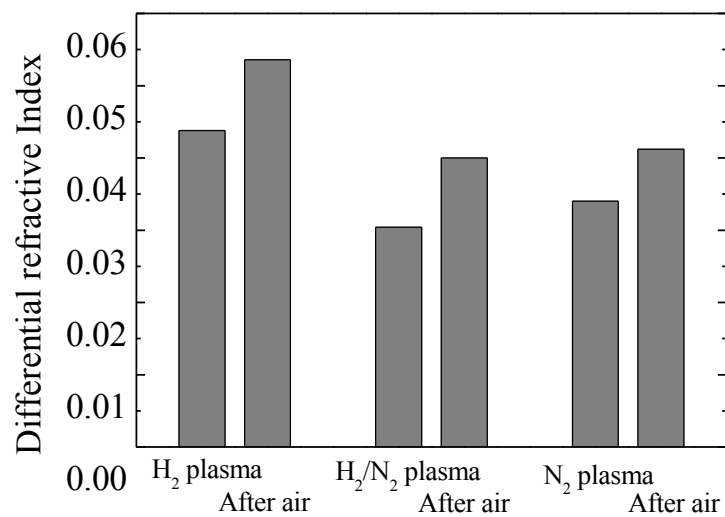


Fig. 4.3 Differential refractive index of porous SiOCH films after H<sub>2</sub>/N<sub>2</sub> plasma and air exposure.

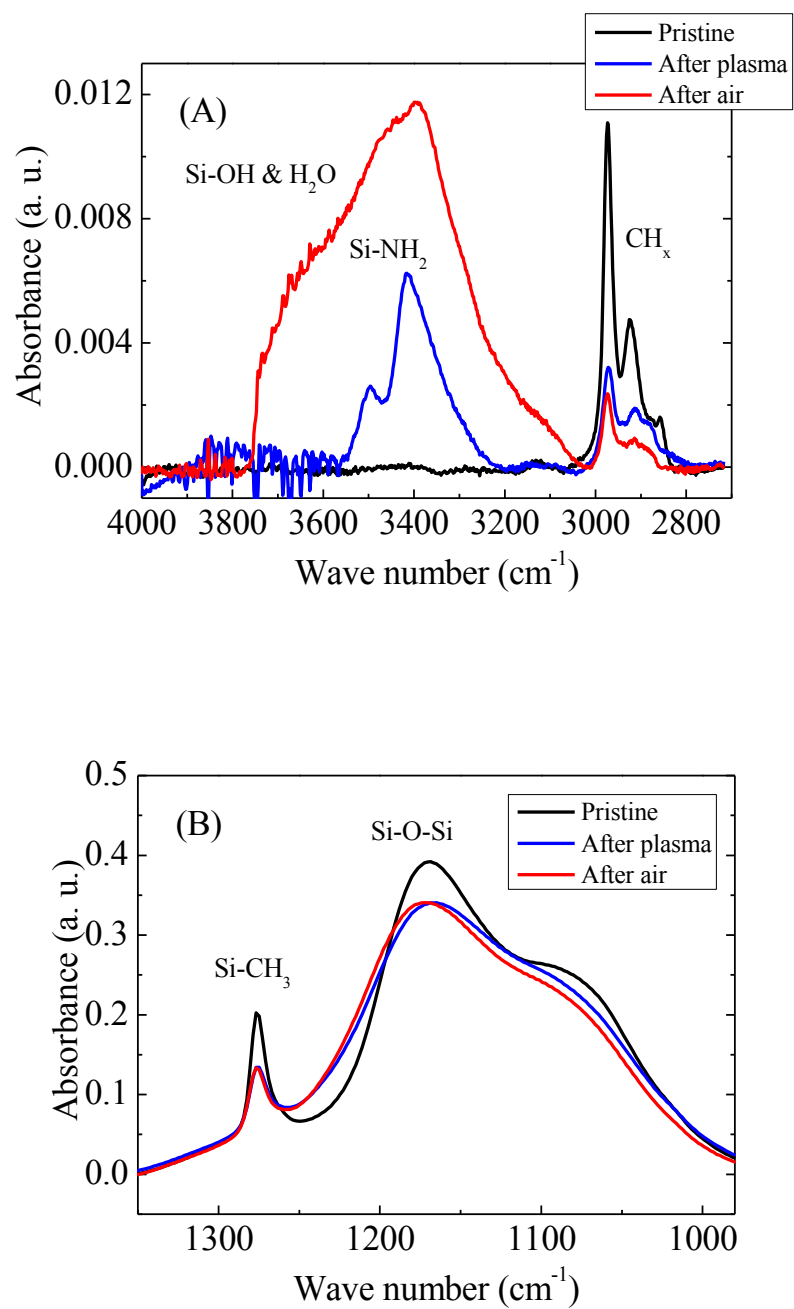


Fig. 4.4 FTIR spectra of porous SiOCH films before and after  $\text{H}_2/\text{N}_2$  plasma exposure and air exposure for (A) Si-OH and  $\text{H}_2\text{O}$  band and (B) Si-CH<sub>3</sub> and Si-O-Si band.

### 4.3.3. Effect of Remained Fluorocarbon Layer on Porous SiOCH Films

In this section, we investigate the effect of CF layer remained after low- $k$  etching process. The CF layer was deposited on the porous SiOCH films in fluorocarbon-based plasmas ( $\text{C}_4\text{F}_8/\text{Ar}$ ). In this CF layer deposition process, pressure, a 60 MHz power, substrate temperature, and flow ratio of  $\text{C}_4\text{F}_8/\text{Ar}$  was 5.0 Pa, 500 W, 20 °C, 10/500 sccm, respectively. We investigated Si- $\text{CH}_3$  bond using the *in situ* FTIR-RAS and chemical composition using the *ex situ* XPS on the porous SiOCH films with or without the CF layer during the  $\text{H}_2$  or  $\text{N}_2$  plasma exposure. In this ashing plasma exposure process was carried out in the 100 MHz CCP chamber, the pressure, the 100 MHz power, the substrate temperature, and the flow ratio of  $\text{H}_2$  or  $\text{N}_2$  were 2.5Pa, 450 W, 20 °C, 100 sccm, respectively.

Figure 4.5 shows the variation of the Si- $\text{CH}_3$  bond absorbance for the porous SiOCH films as a function of the  $\text{H}_2$  or  $\text{N}_2$  plasma exposure time. The amount of Si- $\text{CH}_3$  bond in the porous SiOCH films with or without CF layer after the  $\text{H}_2$  plasma exposure were 10% and 8.0%, respectively. In the case of the  $\text{N}_2$  plasma process, the amounts of Si- $\text{CH}_3$  bond in the films with or without CF layer were 50% and 42%, respectively. From these results, we confirmed that the Si- $\text{CH}_3$  bond was protected by the CF layer during the  $\text{N}_2$  plasma exposure. Figure 4.6 and 4.7 show the refractive index and thickness of the porous SiOCH films as a function of plasma exposure time. In the case of  $\text{H}_2$  plasma, the difference in refractive index and thickness were only seen on the samples before the plasma exposure. There was little effect of CF layer during the plasma exposure, which imply CF layer was removed immediately by  $\text{H}_2$  plasma. In the case of  $\text{N}_2$  plasma, the changes of refractive index and thickness on the sample with CH layer were smaller than that without CF layer.

Figure 4.8 shows the atomic concentration of the porous SiOCH film and the films after the  $\text{H}_2$  or  $\text{N}_2$  plasma exposure. The XPS analysis were demonstrated on (a)

the pristine film, (b) after the CF layer deposit process, (c) after the H<sub>2</sub> plasma exposure, (d) after the N<sub>2</sub> plasma exposure, (e) after the CF layer deposit process and the H<sub>2</sub> plasma exposure, (f) after the CF layer deposit process and the N<sub>2</sub> plasma exposure. The presence or absence of the CF layer did not affect to chemical composition after the plasma exposure. The fluorine concentration on the porous SiOCH film after CF layer deposition was 27%. After the H<sub>2</sub> plasma exposure, a small amount of fluorine was detected on the film, however, the fluorine concentration after the N<sub>2</sub> plasma exposure was 3%. Figure 4.9 shows C1s core level energy regions of XPS for the porous SiOCH films after fluorocarbon-based plasmas exposure. The deposited CF layer on the porous SiOCH films consist of CF, CF<sub>2</sub>, CF<sub>3</sub>.

Figure 4.10 shows C1s core level energy regions of XPS for the porous SiOCH films after the H<sub>2</sub> or N<sub>2</sub> plasma exposure. No peak shift was detected after the H<sub>2</sub> plasma exposure as shown in Fig. 4.10 (a). While the peak shift corresponding to CF<sub>x</sub> and CN were detected as shown in Fig. 4.10 (b). These results showed that the CF layer removed after the H<sub>2</sub> plasma exposure and the CF layer and reactive layer remained on the films after the N<sub>2</sub> plasma exposure and slowed down the plasma damage generation. The reason why the plasma damage occur even though the CF layer exist on the porous SiOCH film is probably because radicals and radiation light pass though the CF layer and damage to the porous SiOCH films. Schematic model of effect of remained CF layer on porous SiOCH film during ash plasma process is shown in Fig. 4.11.

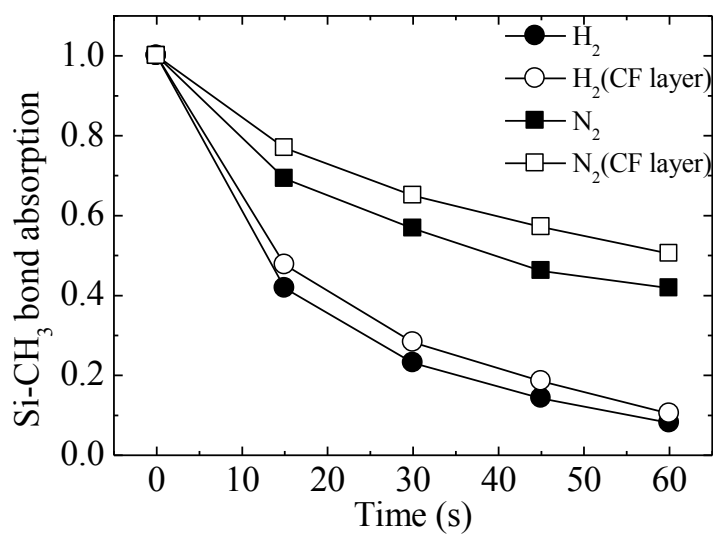


Fig. 4.5 Si-CH<sub>3</sub> bond absorbance as a function of plasma exposure time.

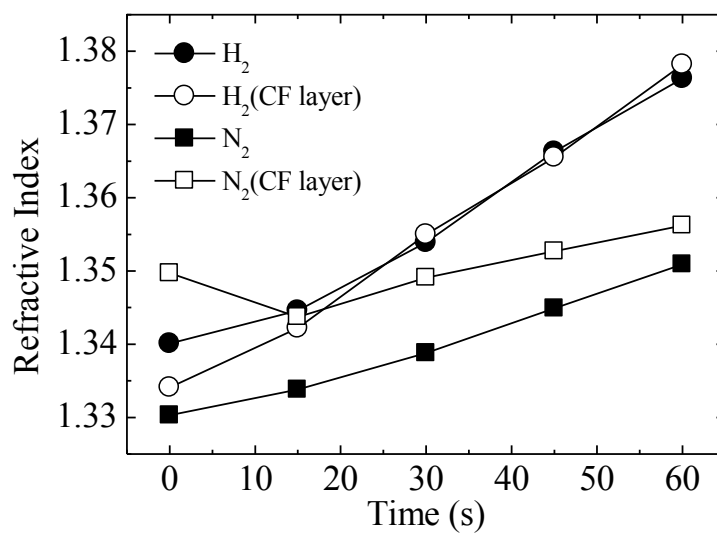


Fig. 4.6 Refractive index as a function of plasma exposure time.

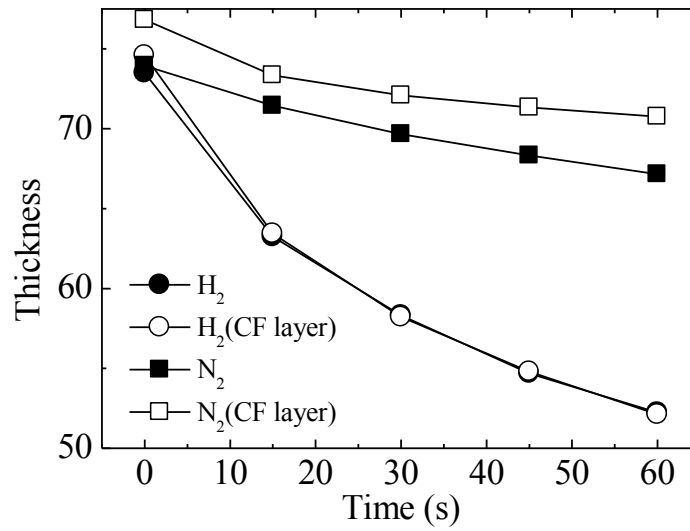


Fig. 4.7 Thickness as a function of plasma exposure time.

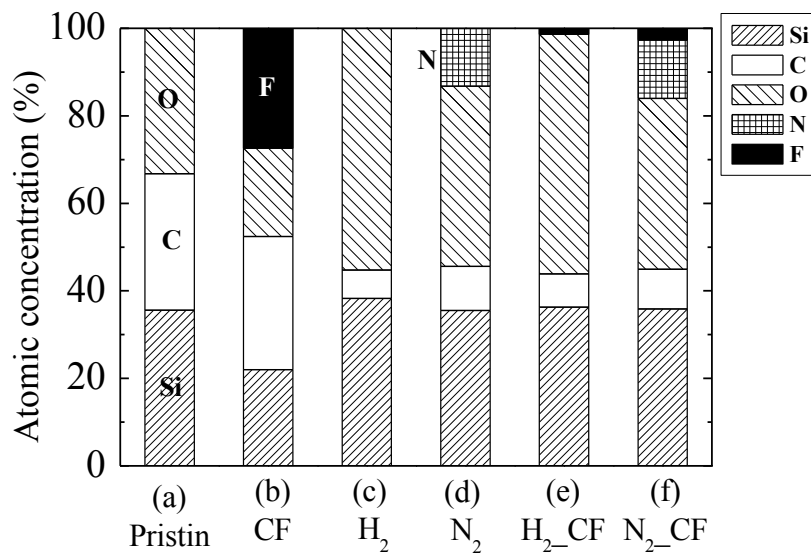


Fig. 4.8 Chemical composition of porous SiOCH films: (a) pristine, (b) after CF layer deposit, (c) after  $H_2$  plasma, (d) after  $N_2$  plasma, (e) after CF layer deposit and  $H_2$  plasma, (f) after CF layer deposit and  $N_2$  plasma.



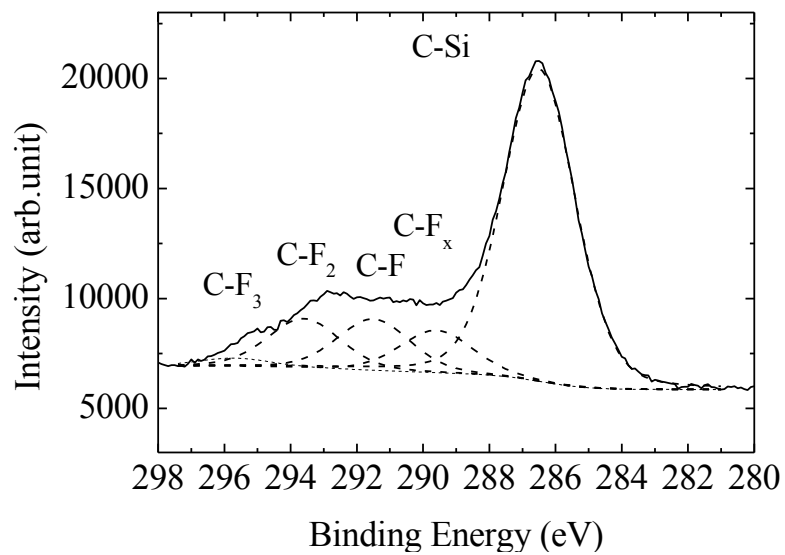


Fig. 4.9. C1s spectra on porous SiOCH films after fluorocarbon-based plasmas exposure.

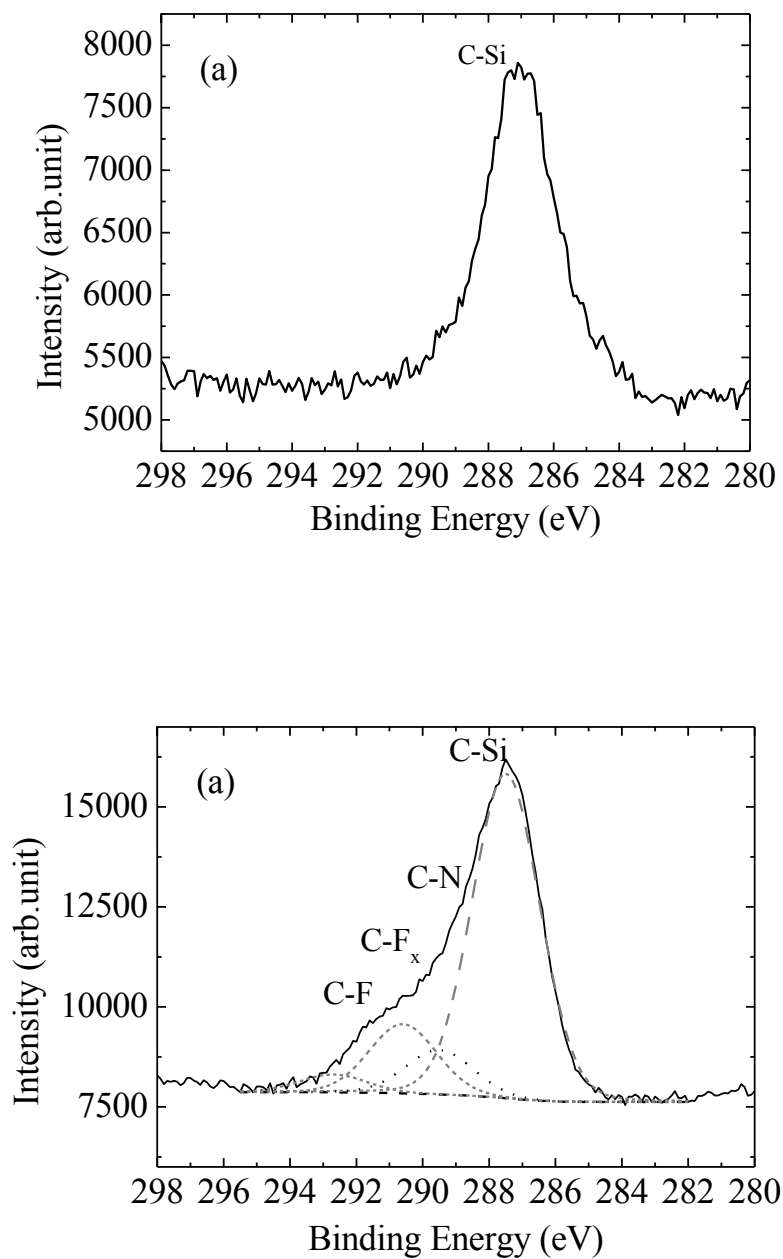


Fig. 4.10  $C_{1s}$  spectra on porous  $SiOCH$  films after (a)  $H_2$  plasma exposure, (b)  $N_2$  plasma exposure.

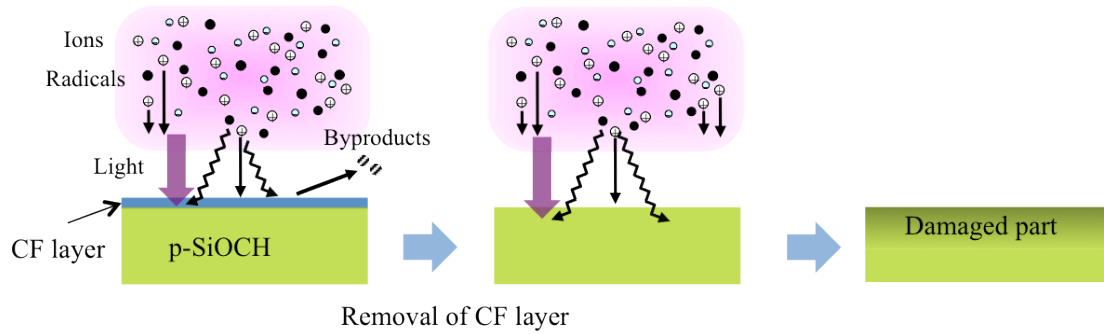


Fig. 4.11 Schematic model of effect of remained CF layer on porous SiOCH film during ash plasma process.

#### 4.3.4 Temperature Dependence

In this section, we consider the substrate temperature dependence of the plasma damage. We employed the temperature measurement system that uses low-coherence interferometry to measure the substrate temperature. Figure 4.12 shows the normalized Si-CH<sub>3</sub> bond (1275 cm<sup>-1</sup>) absorption area of the porous SiOCH films after H<sub>2</sub>/N<sub>2</sub> plasma exposure (H<sub>2</sub>/N<sub>2</sub> gas flow ratio: 0.75) for 60 s at four substrate temperatures. In this experiment, the substrate temperature is the average of the Si wafer temperatures that were measured every 3 s during the plasma process. The substrate temperature increased during plasma exposure for 60 s. The normalized Si-CH<sub>3</sub> bond absorption of the films after the plasma exposure was about 0.4 in the range 8 to 74 °C. *In situ* ellipsometry measurements revealed that the thickness of the porous SiOCH films did not change with the substrate temperature (not shown here). This indicates that the substrate temperature does not affect the amount of damage in this temperature range. Therefore, we did not account for substrate temperature variations during plasma exposure in subsequent experiments.

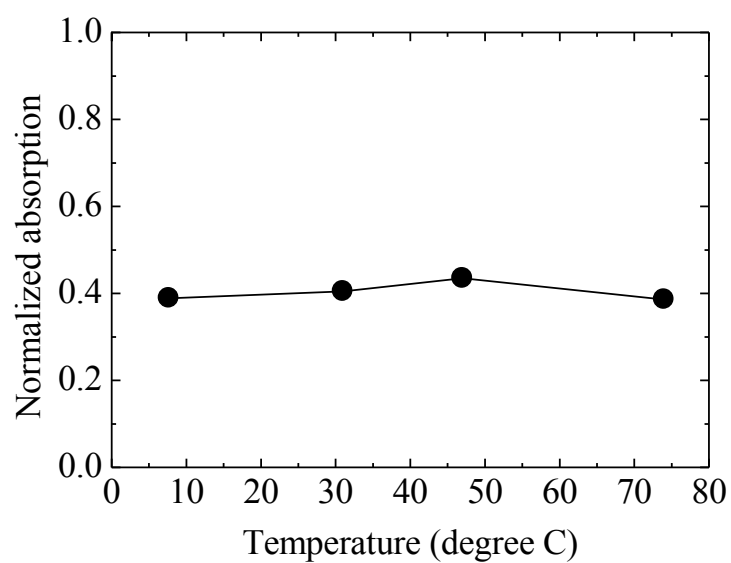


Fig. 4.12 Si-CH<sub>3</sub> bond absorption areas of porous SiOCH films after H<sub>2</sub>/N<sub>2</sub> plasma as a function of substrate temperature.

### 4.3.5 Plasma Diagnostics

To estimate the effect of radicals, the H and N radical densities in the plasmas were investigated using VUVAS. In these measurements, the total gas flow was 100 sccm ( $\text{H}_2/\text{N}_2$  gas flow ratio was 0.5), the total pressure was 2.5 Pa, the VHF power was 450 W, the substrate temperature was 20 °C. The lower electrode was floating. Figure 4.13 shows the H and N radical densities in  $\text{H}_2$  and  $\text{H}_2/\text{N}_2$  plasmas. The N radical density was  $1.5 \times 10^{10} \text{ cm}^{-3}$  in the  $\text{H}_2/\text{N}_2$  plasma, whereas N radicals were not detected in the  $\text{H}_2$  plasma. The H radical density was  $2.3 \times 10^{11} \text{ cm}^{-3}$  in the  $\text{H}_2/\text{N}_2$  plasma, which is higher than that in the  $\text{H}_2$  plasma. This result also supports that N radicals inhibit the extraction of Si-CH<sub>3</sub> bonds by H radicals.

Figure 4.14 shows the optical emission spectra of  $\text{H}_2$  and  $\text{H}_2/\text{N}_2$  plasmas in the wavelength range 115 to 250 nm. A broad emission in the range 150 to 170 nm and a narrow emission at 121.6 nm were observed. Since the bond energies of Si-C and Si-O are respectively 4.5 eV (275 nm) and 8.0 eV (155 nm), VUV radiation in  $\text{H}_2$  and  $\text{H}_2/\text{N}_2$  plasmas might break these bonds by bond excitation [6]. The VUV intensity in the  $\text{H}_2$  plasma is stronger than in the  $\text{H}_2/\text{N}_2$  plasma. This agrees well with the spectroscopic ellipsometry and FTIR spectroscopy results for the modification of sample (d), which had been exposed to only light radiation.

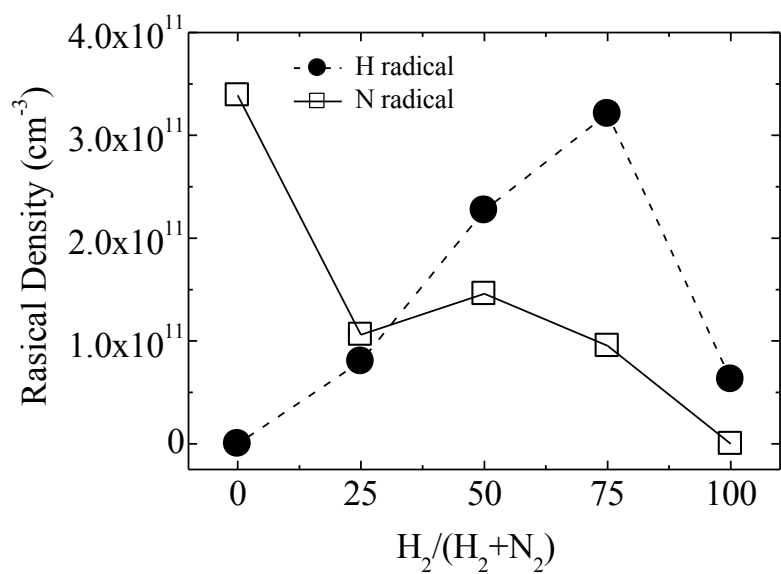


Fig. 4.13 H and N radical densities as a function of flow rate ratio.

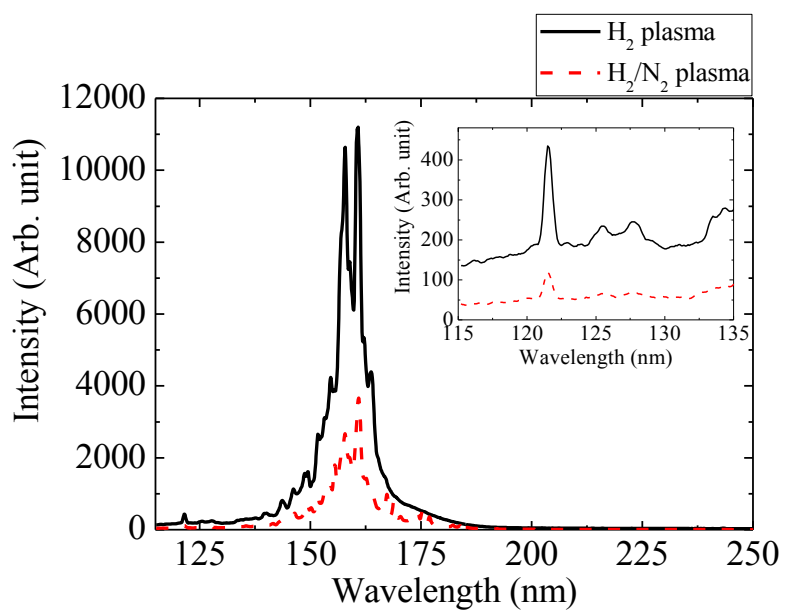


Fig. 4.14 Optical emission spectra of  $H_2$  and  $H_2/N_2$  plasmas in VUV and UV regions.

## 4.4 Conclusion

In this Chapter, effect of remained CF layer and air exposure after plasma exposure on low- $k$  porous SiOCH Films. Vacuum ultraviolet absorption spectroscopy (VUVAS) was used to measure the H and N radical densities in the plasmas

Change of refractive index and thickness, and chemical composition during plasma treatment and subsequent air exposure was investigated using FTIR and spectroscopic ellipsometry, XPS, respectively. There was no big difference in thickness during air exposure, but the refractive index increased. It could be due to the water absorption during air exposure. The CF layer did not have a large effect on H<sub>2</sub> plasma process. On the other hand, the CF layer inhibited the plasma damage during N<sub>2</sub> plasma process. The mechanism of ash plasma damage on porous SiOCH films are investigated in next Chapter.

## 4.5 References

- [1] M. Fukasawa, T. Hasegawa, S. Hirano, and S. Kadomura: Proc. Symp. Dry Process, 1998, p. 175.
- [2] K. Maex, M. R. Baklanov, D. Shamiryan, F. Iacopi, S. H. Brongersma, and Z. S. Yanovitskaya, J. Appl. Phys. **93**, 8793 (2003).
- [3] N. Posseme, T. Chevolleau, T. David, M. Darnon, O. Louveau, and O. Joubert, J. Vac. Sci. Technol. B **25**, 1928 (2007).
- [4] J. Bao, H. Shi, J. Liu, H. Huang, P. S. Ho, M. D. Goodner, M. Moinpour, and G. M. Kloster, J. Vac. Sci. Technol. B **26**, 219 (2008).
- [5] X. Hua, M. Kuo, G. S. Oehrlein, P. Lazzeri, E. Lacob, M. Andriele, C. K. Inoki, T. S. Kuan, P. Jiang, and W. Wu, J. Vac. Sci. Technol. B **24**, 1238 (2006).
- [6] S. Uchida, S. Takashima, M. Hori, M. Fukasawa, K. Ohshima, K. Nagahata, and T. Tatsumi, J. Appl. Phys. **103**, 073303 (2008).
- [7] S. Xu, C. Qin, L. Diao, D. Gilbert, L. Hou, A. Wiesnoski, E. Busch, R. McGowan, B. White, and F. Weber, J. Vac. Sci. Technol. B **25**, 156 (2007).
- [8] M. A. Worsley, S. F. Bent, S. M. Gates, N. C. Fuller, W. Volksen, M. Steen, and T. Dalton, J. Vac. Sci. Technol. B **23**, 395 (2005).
- [9] H. Cui, R. J. Carter, D. L. Moore, H. G. Peng, D. W. Gidley, and P. A. Burke, J. Appl. Phys. **97**, 113302 (2005).
- [10] B. Jinnai, T. Nozawa, and S. Samukawa, J. Vac. Sci. Technol. B **26**, 1926 (2008).
- [11] K. Takeda, Y. Miyawaki, S. Takashima, M. Fukasawa, K. Oshima, K. Nagahata, T. Tatsumi, and M. Hori, J. Appl. Phys. **109**, 033303 (2011).
- [12] S. Takashima, A. Kono, M. Ito, K. Yoneda, M. Hori and T. Goto, Appl. Phys. Lett. **75**, 3929 (1999).
- [13] S. Takashima, S. Arai, A. Kono, M. Ito, K. Yoneda, M. Hori and T. Goto, J. Vac. Sci. Technol. A **19**, 599 (2001).



- [14] H. Nagai, S. Takashima, M. Hiramatsu, M. Hori, and T. Goto, J. Appl. Phys. **91**, 2615 (2002).
- [15] H. Nagai, M. Hiramatsu, M. Hori, and T. Goto, J. Appl. Phys. **94**, 1362 (2003).
- [16] K. Takeda, Y. Tomekawa, T. Shina, M. Ito, Y. Okamura, and N. Ishii, J. Appl. Phys. **43**, 7737 (2004).



## **Chapter 5      H<sub>2</sub>/N<sub>2</sub> Plasma Damage on Low-*k* Porous SiOCH Film Evaluated by *In Situ* Film Characterization**

### **5.1 Introduction**

This Chapter describes the mechanism of H<sub>2</sub>/N<sub>2</sub> plasma ashing damage of porous SiOCH film.. Investigations of degradation mechanism of porous low-*k* films induced by plasma processes have been investigated only by *ex situ* experiments. Those studies provided us useful information to understand plasma damage mechanism. Several research groups have investigated the damage generation mechanism and revealed that NxHy, H, and N radicals react with SiOCH film and increase of dielectric constant is mainly attributed to the moisture uptake [1-10]. In this Chapter, we investigated the plasma ashing damage mechanism on porous SiOCH films using *in situ* or *ex situ* film characterization techniques. We have constructed an *in situ* measurement system to evaluate the properties of porous SiOCH films during plasma processing. The surface reactions of porous low-*k* materials induced by ions, radicals, and light were investigated using pallet for plasma evaluation (PAPE) [6]. The low-*k* films were characterized by *in situ* spectroscopic ellipsometry, *in situ* Fourier-transform infrared reflection absorption spectroscopy (FTIR-RAS), *ex situ* dynamic secondary ion mass spectrometry (SIMS), and *ex situ* X-ray photoelectron spectroscopy (XPS). Vacuum ultraviolet absorption spectroscopy (VUVAS) was used to measure the H and N radical densities in the plasmas.

## 5.2 Experimental Details

The ash plasma processes were performed in a parallel-plate capacitively coupled plasma (CCP) chamber excited by very high frequency (VHF) radiation with a frequency of 100 MHz (See Fig. 3.1). The lower electrode was floating. The mixture gases of H<sub>2</sub> and N<sub>2</sub> were fed from the upper electrode through a showerhead electrode. A total gas flow is 100 sccm (H<sub>2</sub>/N<sub>2</sub> gas flow ratio was 0.5 unless otherwise mentioned). A Si wafer was placed on the lower electrode with an electrostatic chuck system. The lower electrode temperature was controlled by solvent cooling.

A porous SiOCH ( $k = 2.3$ , approximately 40% porosity) layer was coated on a 150-nm-thick tungsten layer deposited on a Si substrate for the FTIR-RAS experiment. The film thickness was 75 nm and the refractive index at 633 nm was 1.31. The porous SiOCH films were treated by H<sub>2</sub>/N<sub>2</sub> plasma in the CCP chamber. Plasma ashing was performed at a total pressure of 2.5 Pa, a VHF power of 450 W, and a substrate temperature of 20 °C.

An *in situ* spectroscopic ellipsometer and FTIR and VUVAS systems were installed in the chamber. The thickness and the refractive index at 633 nm of the porous SiOCH films were measured by *in situ* spectroscopic ellipsometry (M-2000F, JA Woollam). A single-layer Cauchy model was used to fit the ellipsometry data.

Chemical bond structures in the porous SiOCH films were analyzed by *in situ* FTIR-RAS (Thermo Scientific, Nicolet-8700). FTIR-RAS spectra were recorded between 400 and 4000 cm<sup>-1</sup> with a spectral resolution of 4 cm<sup>-1</sup> by averaging 500 scans. Angle of incidence in FTIR-RAS measurements was 80 degrees with normal to the surface. Infrared radiation was polarized with electric field parallel to an incident plane (p-polarization), introduced through KBr windows to sample position, and detected by using liquid nitrogen cooled mercury cadmium telluride detector. Since the porous SiOCH was coated on a tungsten layer, the signal of the reflection absorption spectrum

was improved and infrared absorption by the Si substrate was negligible. FTIR-RAS spectra presented in this study were not normalized with respect to the SiOCH film thickness since film shrinkage may occur [5].

The *in situ* PAPE method was employed to evaluate the individual or combined effects of light, radicals, and ions generated by the plasmas. A MgF<sub>2</sub> window or a Si plate were placed above the film [6,11]. Four experiments were performed: (a) MgF<sub>2</sub> window with no space, (b) Si plate with a parallel plate gap, (c) MgF<sub>2</sub> plate with a gap, and (d) no placement (see Fig. 5.1). Ion bombardment is significantly reduced by the Si plate and the MgF<sub>2</sub> window. Since the MgF<sub>2</sub> window transmits light with wavelengths above 115 nm, the effect of light could be distinguished by experiment (a). The porous SiOCH film was shielded by the Si plate in experiment (b). With the parallel plate gap, radicals could diffuse through the gap and react with the sample. Experiment (c) was performed to assess the role of radicals and light. Experiment (d) was performed to clarify the effect of the interaction of light, radicals, and ions on the porous SiOCH films. We accounted for the fact that the radicals that diffuse through the gap are estimated to have lower densities than incident radicals when there is no Si plate or MgF<sub>2</sub> window. To investigate the effect of only plasma exposure on the porous SiOCH films, a PAPE was installed in the vacuum chamber. Actual experiment was carried out as shown in Fig. 5.2. *In situ* FTIR-RAS and spectroscopic ellipsometry was performed on the porous SiOCH films every after plasma exposure for 15 s to see changes of chemical bonds, film thickness, and refractive index. To investigate the effect of air exposure, air was introduced into the chamber after the plasma process and the films were exposed to air for 2 h.

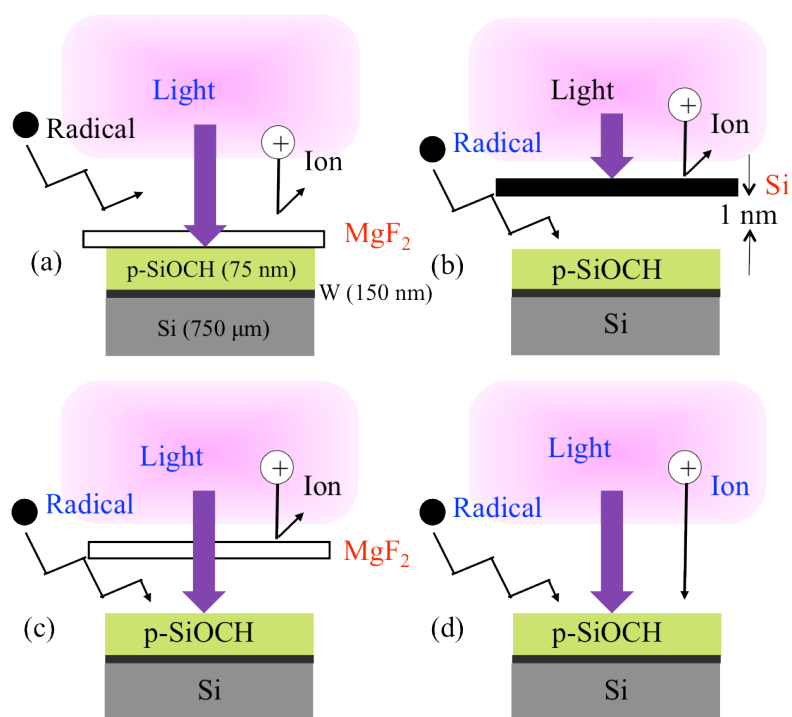


Fig. 5.1 Schematic diagram of sample structure.

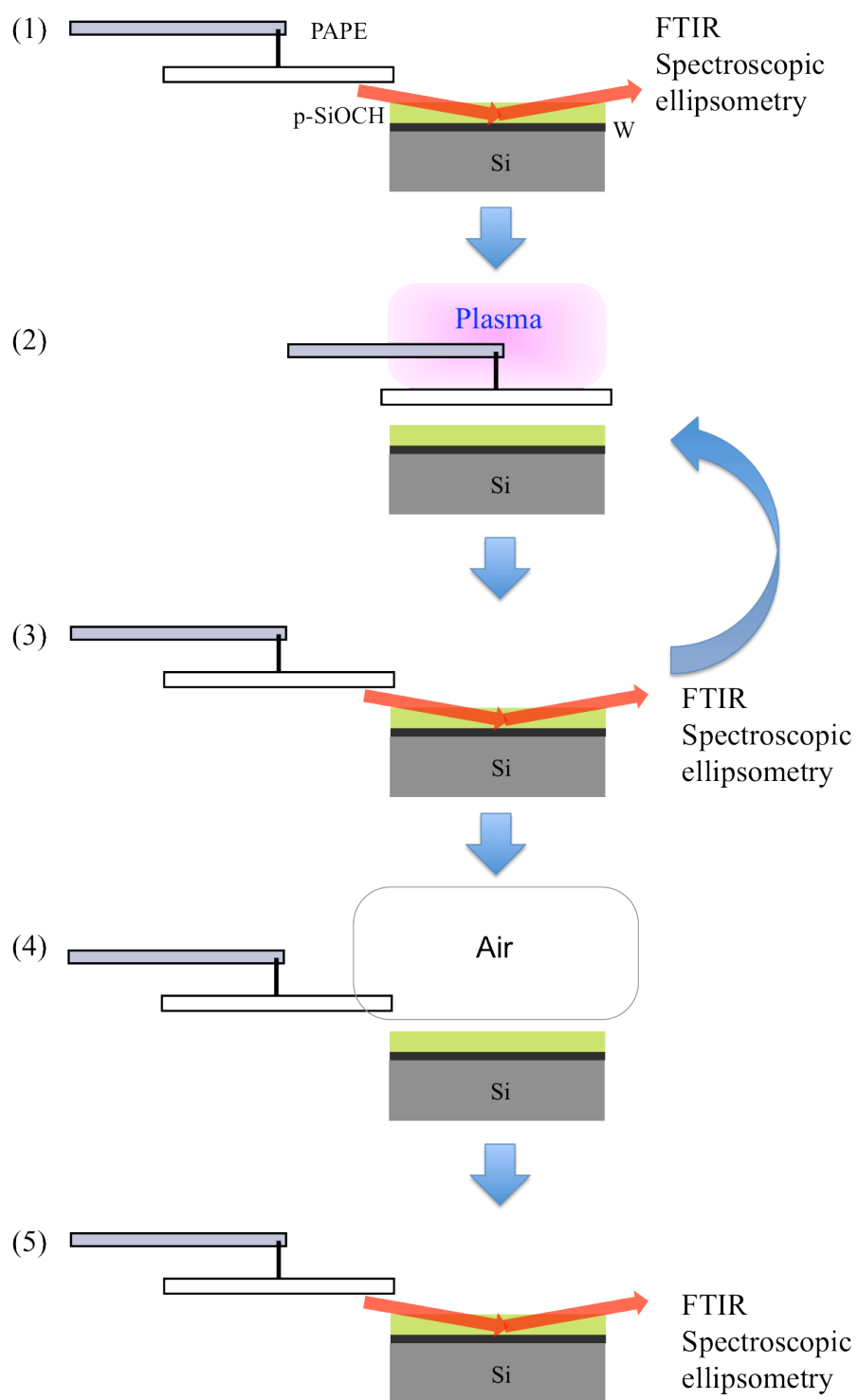


Fig. 5.2 Schematic diagram of experimental procedure.

## 5.3 Results and Discussion

### 5.3.1 Roles for Ions, Radicals, and Light Radiation Analyzed by *in situ* Film Characterization

The porous SiOCH films were treated by  $H_2/N_2$  plasmas in the CCP chamber with a Si plate and a  $MgF_2$  window to evaluate the individual effects of ions, radicals, and light radiation. *In situ* FTIR-RAS and spectroscopic ellipsometry was performed on the porous SiOCH films every after plasma exposure for 15 s to see changes of chemical bonds, film thickness, and refractive index (Note: FTIR analysis required longer than 5 min to obtain a good signal-to-noise ratio.). We assumed that the films damaged by plasma were not modified during film characterization in the vacuum chamber.

Figures 5.3(A), (B), and (C) show the porous SiOCH film thickness as functions of  $H_2$ ,  $H_2/N_2$ , and  $N_2$  plasma exposure times, respectively. First in pure hydrogen case, the thickness of sample (a), which had been exposed to light radiation, decreased to 66 nm and the thickness of sample (c), which had been exposed to radicals and light radiation, decreased to 63 nm and. The thickness of sample (d), which had been exposed to ions, radicals, and light radiation, decreased drastically from 75 nm to 52 nm after  $H_2$  plasma exposure. In contrast, the thickness of sample (b), which had been exposed to radicals, did not decrease. This indicates that H radicals alone are not responsible for reducing the film thickness; rather, ions, light, and the synergy between the radicals, and light causes the thickness reduction of porous SiOCH films. For the  $H_2/N_2$  plasma, the thickness of sample (d) decreased to 63 nm. The thicknesses of the other three samples decreased slightly. The thicknesses of samples that had been treated with the  $H_2$  plasma vary more than those of samples that had been treated with  $H_2/N_2$  plasma. For the  $N_2$  plasma, the thickness of sample (c) and (d) decreased to 69.5 and



68.5 nm, respectively. The thicknesses of the other two samples decreased slightly. The thicknesses of samples that had been treated with the  $H_2$  plasma vary more than those of samples that had been treated with  $H_2/N_2$  plasma. As described later, for this  $H_2/N_2$  case, H radical amount was greater than the pure  $H_2$  case. Therefore we believe addition of nitrogen reduced changes in thickness of the film by inhibiting SiOCH etch.

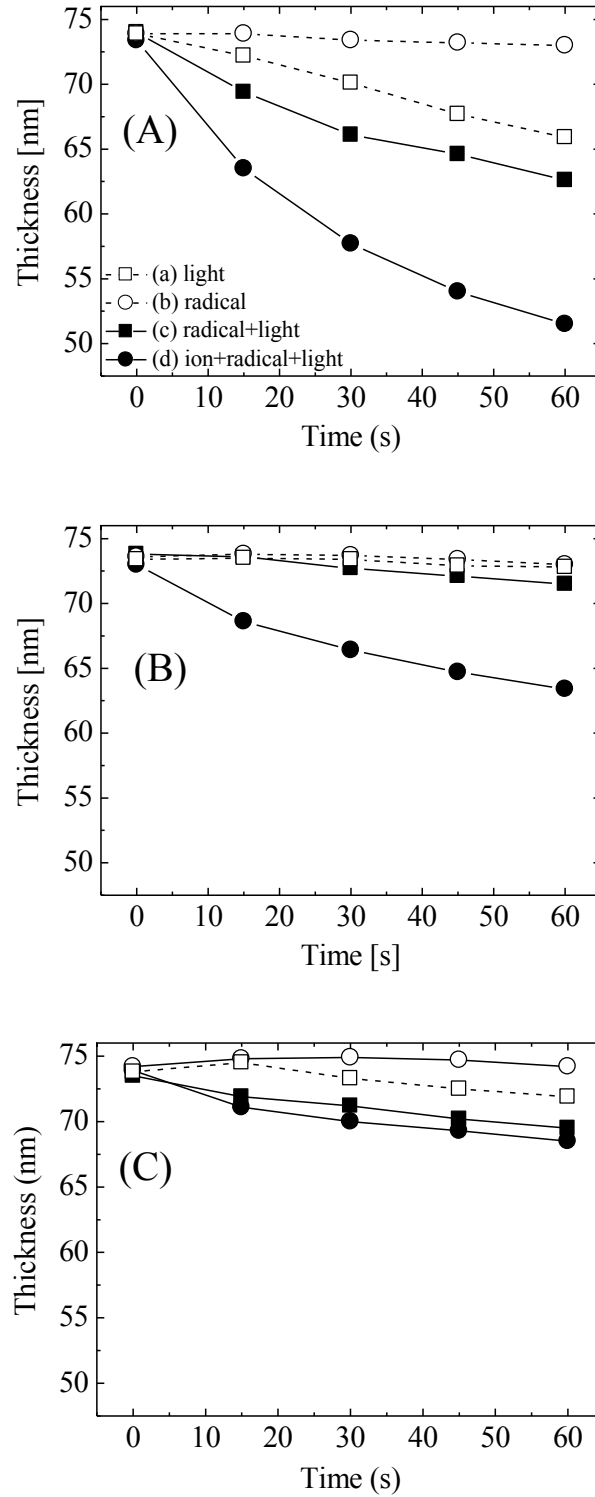


Fig. 5.3 Variation of porous SiOCH film thickness as a function of (A) H<sub>2</sub> plasma, (B) H<sub>2</sub>/N<sub>2</sub> plasma, and (C) N<sub>2</sub> plasma exposure time.

Figures 5.4(A), (B), and (C) show the changes in the refractive index of the porous SiOCH films during  $H_2$ ,  $H_2/N_2$ , and  $N_2$  plasma exposure. The refractive index of each sample prior to plasma exposure was about 1.33. After  $H_2$  plasma exposure for 60 s, the refractive index of sample (d) increased drastically, whereas those of the other samples changed slightly. In the case of the  $H_2/N_2$  plasma, the refractive index of sample (d) increased, whereas those of the other samples changed slightly. In the case of the  $N_2$  plasma, the refractive index of sample (d) increased, whereas those of the other samples changed slightly. Compared with the  $H_2$  plasma, the  $H_2/N_2$  or  $N_2$  plasma changes the refractive index less. These results indicated that ions strongly increase the refractive index of the porous SiOCH films.

Modification of the porous SiOCH films was examined by *in situ* FTIR spectroscopy (FTIR-RAS spectra will be shown later). Figures 5.5(A), (B), and (C) show the normalized area of Si-CH<sub>3</sub> bond absorption in the porous SiOCH films during  $H_2$ ,  $H_2/N_2$ , and  $N_2$  plasma exposure. In the case of  $H_2$  plasma, as similar as the cases for changes in thickness and refractive index as described before, Si-CH<sub>3</sub> bond absorption of sample (d) for exposing all ions, radicals and light radiation decreased drastically to 0.08. The effect of exposure to light radiation, as seen in samples (a) and (c), is to reduce the normalized area of Si-CH<sub>3</sub> bond absorption suppressed to decrease to be 0.53 and 0.44, respectively. In the case of  $H_2/N_2$  plasma exposure, Si-CH<sub>3</sub> bond absorption of samples (b), (c), and (d) decreased to 0.90, 0.77, and 0.31, respectively. The amount of Si-CH<sub>3</sub> extracted by  $H_2/N_2$  plasma was smaller than that by  $H_2$  plasma.

By utilizing the silicon plate and the  $MgF_2$  window, we evaluated the individual and combined contributions of ions, radicals and light radiations. First, in the case of pure hydrogen, we concluded that H radicals alone are not responsible for reducing the film thickness and increasing refractive index, but can reduce Si-CH<sub>3</sub> bond density. Ions, light, and the synergy between the radicals and light cause the modifications of porous SiOCH films. This tendency is also observed for  $H_2/N_2$  plasma

exposure, however, those results indicated a suppression of changes in the modifications. Thus we speculate that nitrogen-related species were responsible for these differences. So we considered how the plasma parameters are modified in the mixture plasma of nitrogen and hydrogen.

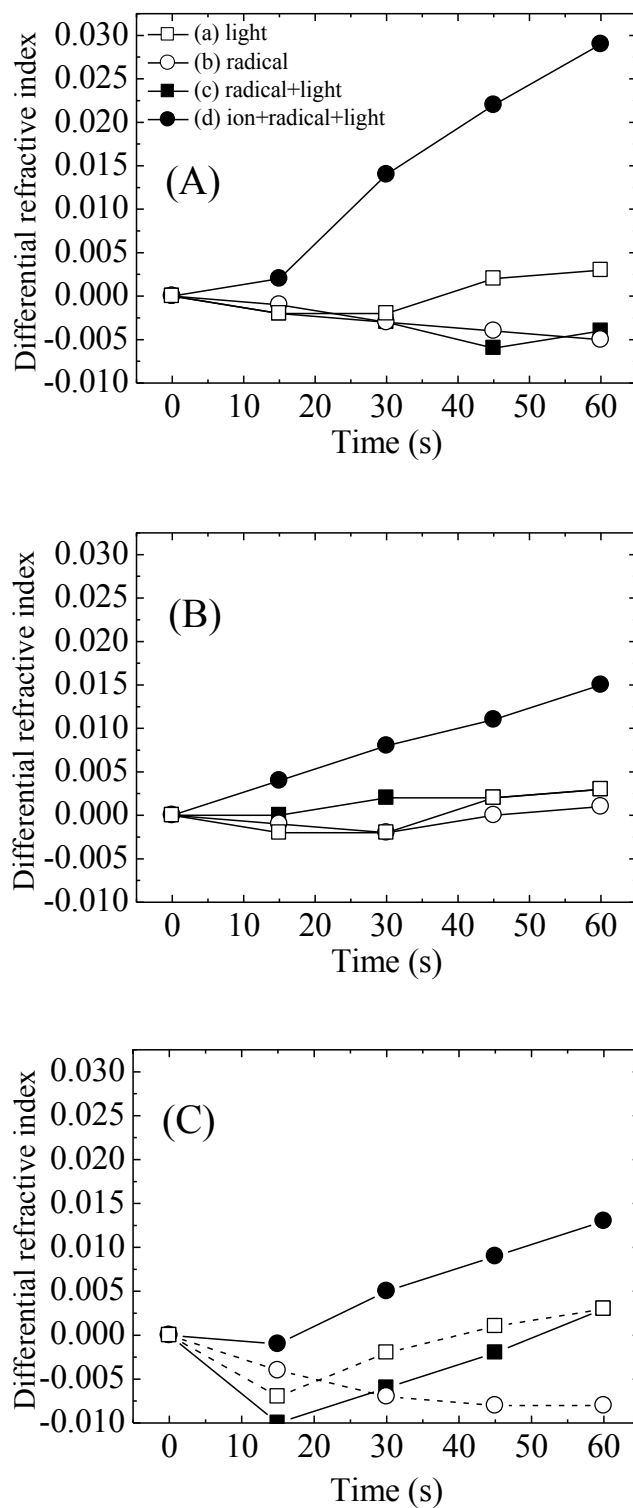


Fig. 5.4 Differential refractive index of porous SiOCH films as a function of (A)  $H_2$  plasma, (B)  $H_2/N_2$  plasma, and (C)  $N_2$  plasma exposure time.

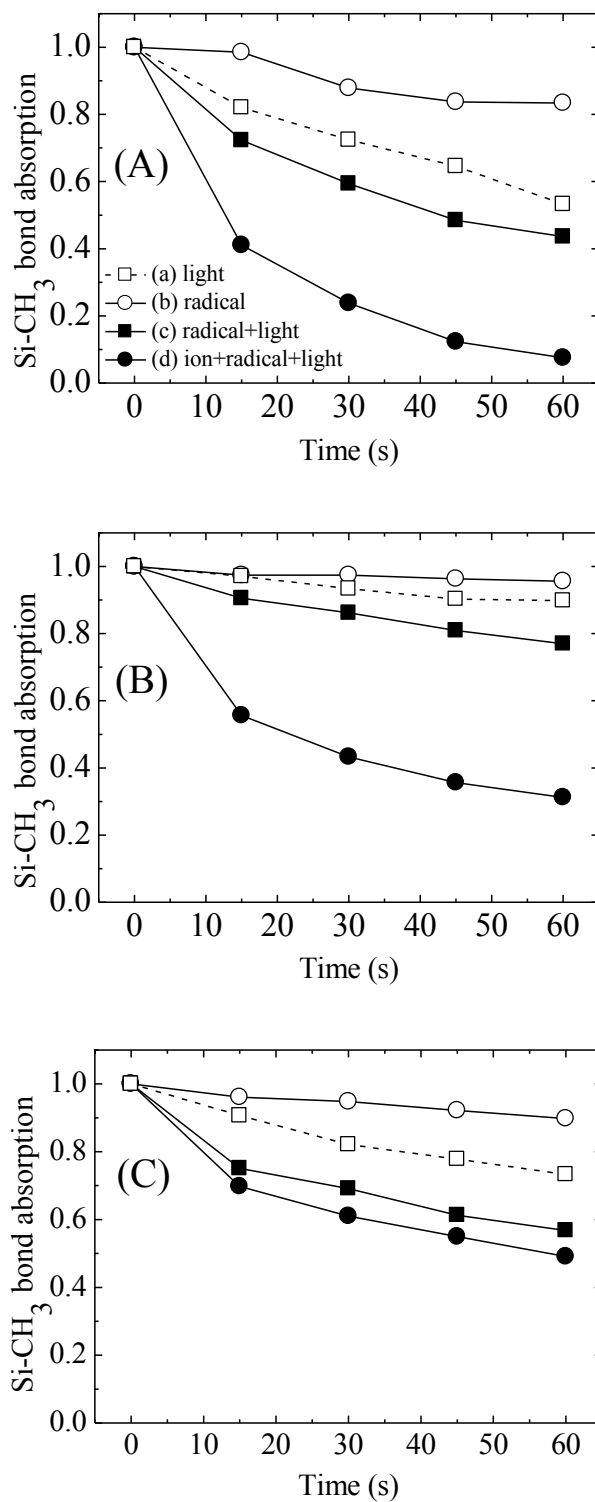


Fig. 5.5 Variation of Si-CH<sub>3</sub> bond absorption of porous SiOCH films as a function of (A) H<sub>2</sub> plasma, (B) H<sub>2</sub>/N<sub>2</sub> plasma, and (C) N<sub>2</sub> plasma exposure time.

Figure 5.6 shows *in situ* FTIR-RAS spectra of porous SiOCH films before and after H<sub>2</sub>/N<sub>2</sub> plasma exposure for 180 s. The pristine film had absorption bands between 2850 and 3000 cm<sup>-1</sup> (attributed to the CH<sub>x</sub> bond), at 1275 cm<sup>-1</sup> (attributed to the Si-CH<sub>3</sub> bond), and between 1000 and 1250 cm<sup>-1</sup> (attributed to the Si-O-Si bond). FTIR-RAS detected peaks between 3200 and 3700 cm<sup>-1</sup> (attributed to the Si-OH bond and H<sub>2</sub>O), between 2300 and 2100 cm<sup>-1</sup> (attributed to the Si-H bond), and between 1600 and 1500 cm<sup>-1</sup> (attributed to the Si-NH<sub>2</sub> bond) in the porous SiOCH film exposure to H<sub>2</sub>/N<sub>2</sub> plasma. The FTIR spectra revealed that the porous SiOCH films consist of a Si-O-Si structure terminated by methyl groups (Si-CH<sub>3</sub>).

Figures 5.7 – 5.9 show enlarged FTIR-RAS spectra of porous SiOCH films during H<sub>2</sub>, H<sub>2</sub>/N<sub>2</sub>, and N<sub>2</sub> plasma exposure and after air exposure in 1400-900 cm<sup>-1</sup> region at different conditions: (a) light radiation, (b) radical, (c) radical + light, and (d) radical + light + ion. These figures showed change in Si-O-Si and Si-CH<sub>3</sub> peak intensities after each plasma exposures. These spectra contain absorption bands between 3200 and 3700 cm<sup>-1</sup> (attributed to Si-OH bond and H<sub>2</sub>O), between 2850 and 3000 cm<sup>-1</sup> (attributed to the CH<sub>x</sub> bond), at 1275 cm<sup>-1</sup> (attributed to the Si-CH<sub>3</sub> bond), and between 1000 and 1250 cm<sup>-1</sup> (attributed to the Si-O-Si bond). The amount of Si-CH<sub>3</sub> was already discussed and those peak shifts in Si-O-Si will be discussed later.

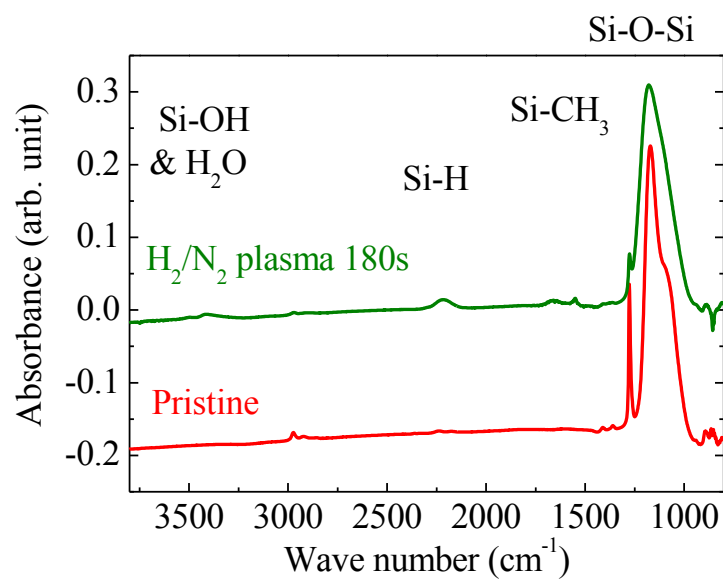


Fig. 5.6 FTIR-RAS spectra of pristine porous SiOCH film.



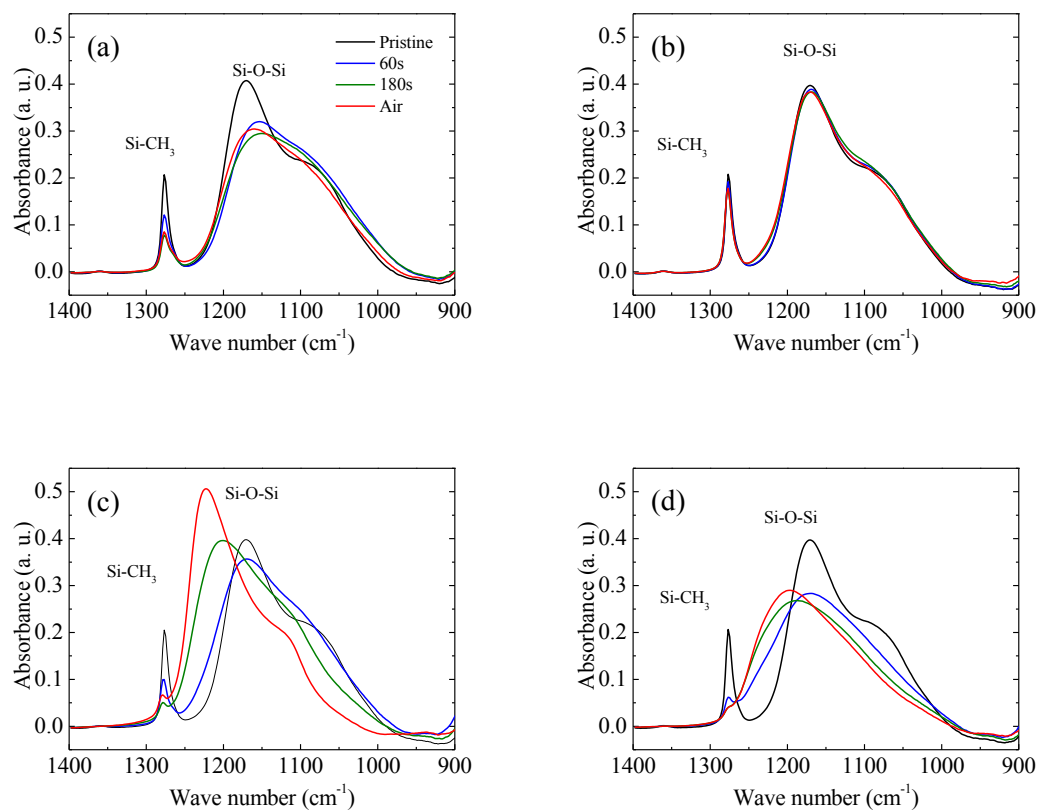


Fig. 5.7 FTIR-RAS spectra of porous SiOCH films during  $\text{H}_2$  plasma exposure and after air exposure in 1400-800  $\text{cm}^{-1}$  region at different conditions: (a) light radiation, (b) radical, (c) radical + light, and (d) radical + light + ion.

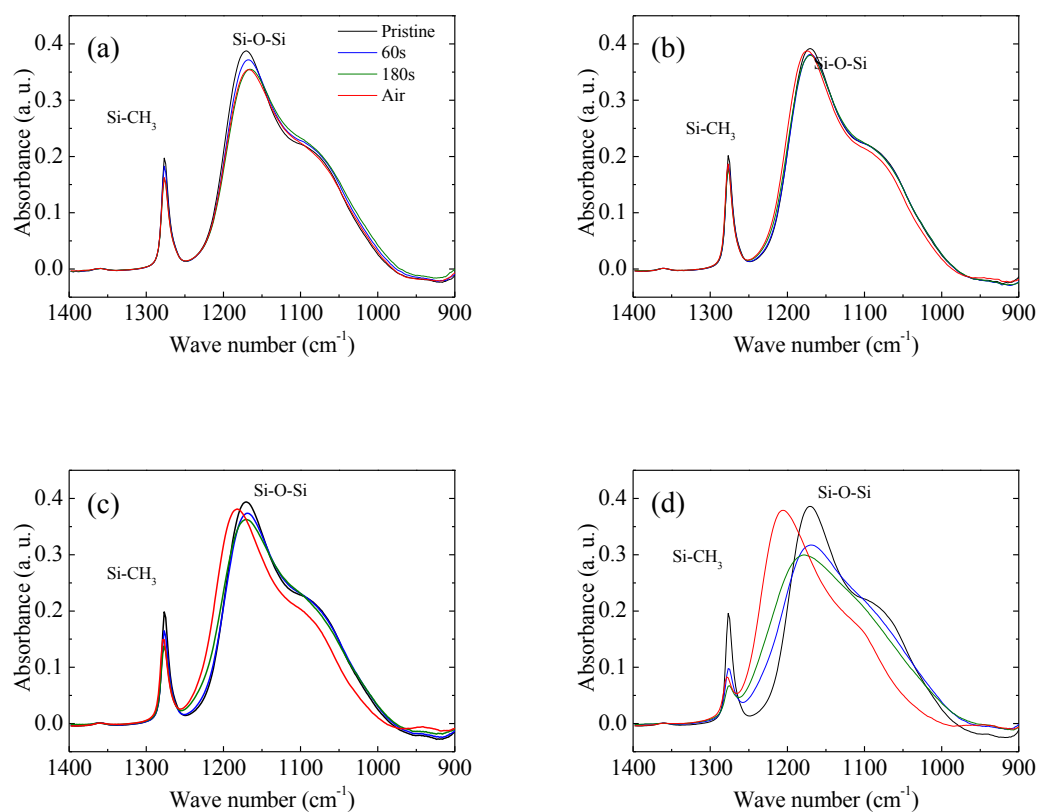


Fig. 5.8 FTIR-RAS spectra of porous SiOCH films during H<sub>2</sub>/N<sub>2</sub> plasma exposure and after air exposure in 1400-800 cm<sup>-1</sup> region at different conditions: (a) light radiation, (b) radical, (c) radical + light, and (d) radical + light + ion.

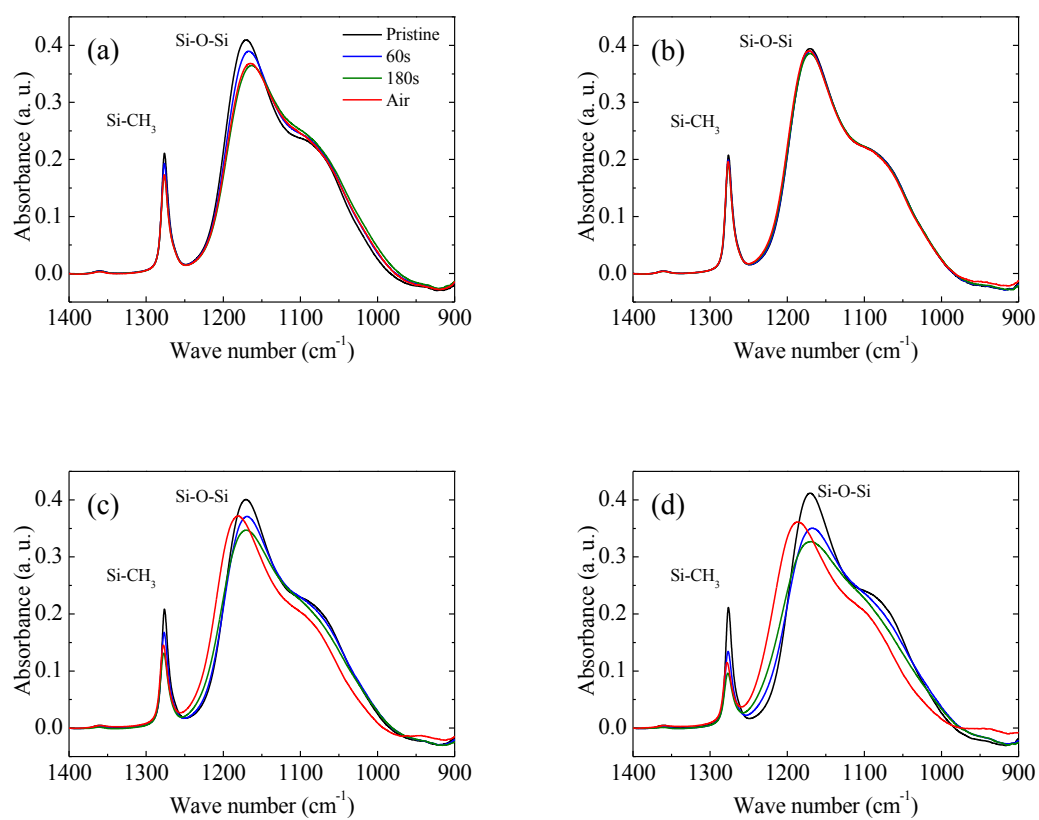


Fig. 5.9 FTIR-RAS spectra of porous SiOCH films during  $\text{N}_2$  plasma exposure and after air exposure in 1400-800  $\text{cm}^{-1}$  region at different conditions: (a) light radiation, (b) radical, (c) radical + light, and (d) radical + light + ion.

Figures 5.10-24 show the relationship between the extraction of methyl and other chemical bonds. These figures show FTIR-RAS spectra in the range 3900 - 2800  $\text{cm}^{-1}$  region of porous SiOCH films obtained during  $\text{H}_2$ ,  $\text{H}_2/\text{N}_2$ , and  $\text{N}_2$  plasma exposure for 60 - 180 s and after subsequent air exposure at different conditions: (a) light, (b) radicals, (c) light + radicals, and (d) light + radicals + ion bombardment. These spectra contain absorption bands between 3200 and 3700  $\text{cm}^{-1}$  (attributed to Si-OH bond and  $\text{H}_2\text{O}$ ), between 2850 and 3000  $\text{cm}^{-1}$  (attributed to  $\text{CH}_x$  bond), and at 3335  $\text{cm}^{-1}$  (attributed to Si-NH<sub>2</sub> bond) [13,15]. The change in the  $\text{CH}_x$  peak during plasma exposure was similar to that for the Si-CH<sub>3</sub> peak. These results imply that carbon was depleted by plasma exposure and they indicate that the  $\text{CH}_x$  peak is attributable to Si-CH<sub>3</sub> bonds.

In the case of  $\text{H}_2$  plasma exposure, even though carbon was detected, no obvious change in the Si-OH peak was detected for samples (a) and (d) during plasma exposure (i.e., without exposure to air). The Si-OH peak in samples (b) and (c) increased with increasing  $\text{H}_2$  plasma exposure time. After air exposure, the Si-OH peak in samples (a), (c), and (d) increased drastically, whereas only a slight increase was observed for sample (b). The remarkable changes in these samples during air exposure can be explained by the presence of reactive species such as dangling bonds, which easily react with moisture and change Si-OH bonds. No obvious change was observed for sample (a) during exposure to the  $\text{H}_2/\text{N}_2$  plasma, whereas the Si-NH<sub>2</sub> and Si-OH peaks increased in samples (b), (c), and (d) during plasma exposure. The Si-OH peak increased in all samples after air exposure. Slight change was observed for sample (a) and (b) during exposure to the  $\text{N}_2$  plasma. The Si-NH<sub>2</sub> and Si-OH peaks increased in samples (c), and (d) during plasma exposure. The Si-OH peak increased in all samples after air exposure.

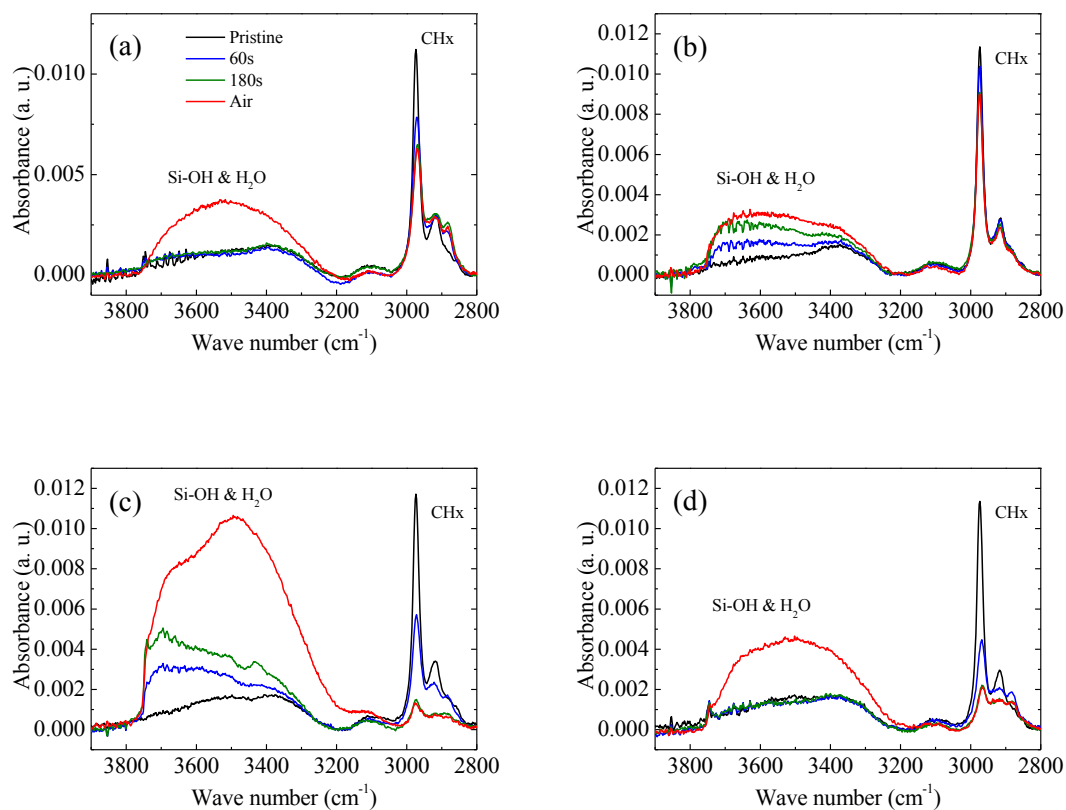


Fig. 5.10 FTIR-RAS spectra in the range 3900-2800 cm<sup>-1</sup> of porous SiOCH films during H<sub>2</sub> plasma exposure and after subsequent exposure to air for (a) light, (b) radicals, (c) light + radicals, and (d) light + radicals + ion.

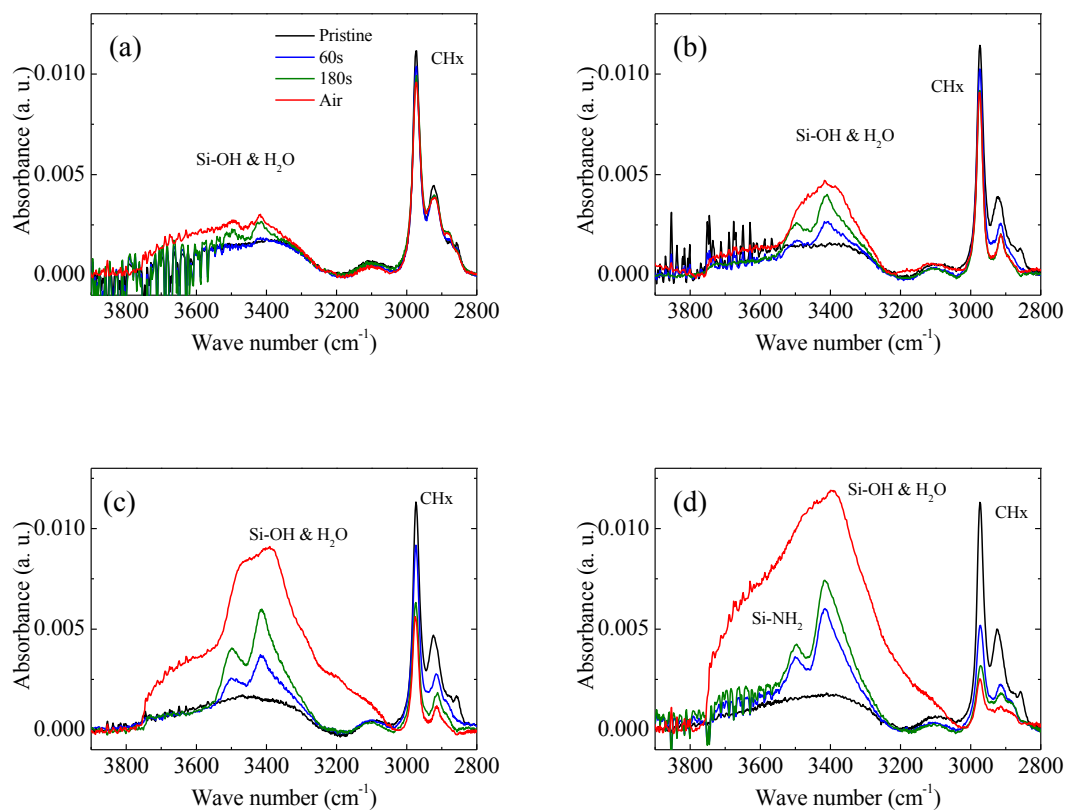


Fig. 5.11 FTIR-RAS spectra in the range 3900-2800 cm<sup>-1</sup> of porous SiOCH films during H<sub>2</sub>/N<sub>2</sub> plasma exposure and after subsequent exposure to air for (a) light, (b) radicals, (c) light + radicals, and (d) light + radicals + ions.

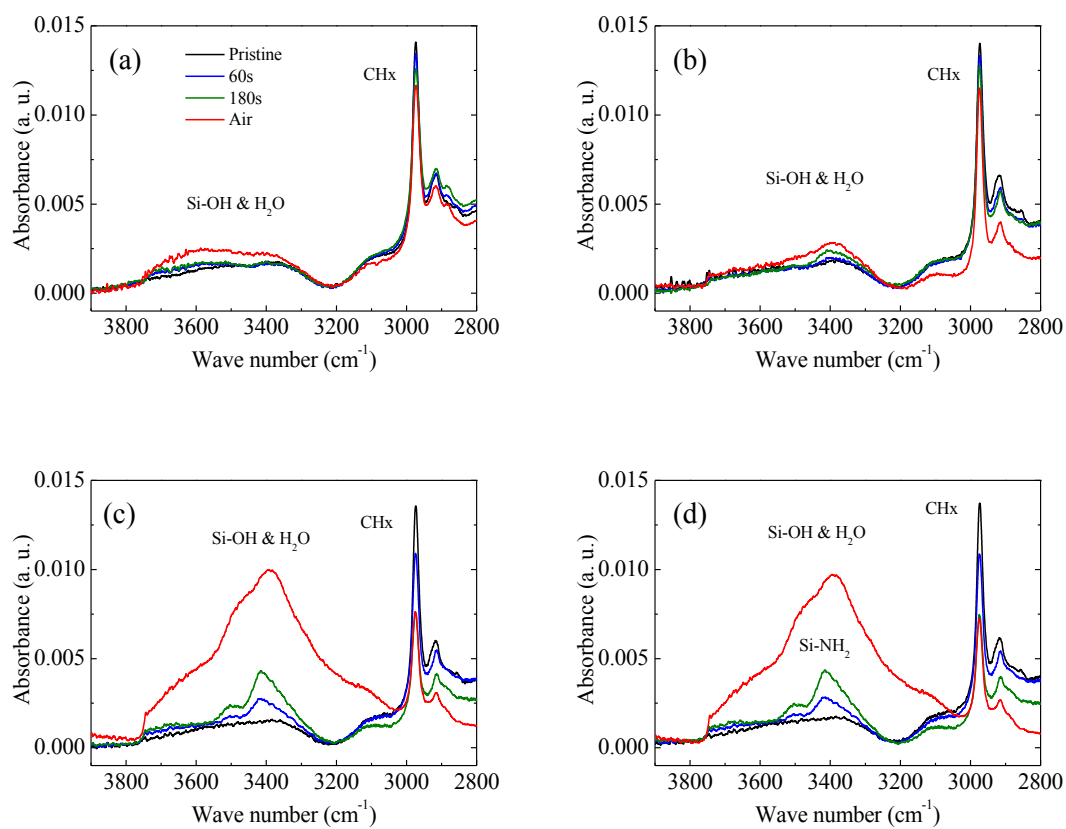


Fig. 5.12 FTIR-RAS spectra in the range 3900-2800 cm<sup>-1</sup> of porous SiOCH films during N<sub>2</sub> plasma exposure and after subsequent exposure to air for (a) light, (b) radicals, (c) light + radicals, and (d) light + radicals + ions.

To investigate nitrogen-containing bonds, Si-NH<sub>2</sub> (1600 cm<sup>-1</sup>) and CH=NH (1655, 1725 cm<sup>-1</sup>) [13,17] peaks were considered because these peaks did not overlap with other peaks. Figure 5.13 and 5.14 shows FTIR-RAS spectra in the range 1800-1500 cm<sup>-1</sup> of porous SiOCH films during H<sub>2</sub>/N<sub>2</sub> or N<sub>2</sub> plasma exposure for 60-180 s and subsequent exposure to air for the different conditions. H<sub>2</sub> plasma exposure did not cause the formation of Si-NH<sub>2</sub> and CH=NH bonds in all samples. In the case of H<sub>2</sub>/N<sub>2</sub> plasma, light from H<sub>2</sub>/N<sub>2</sub> plasma did not form any nitrogen-containing bonds, whereas Si-NH<sub>2</sub> and CH=NH peaks increased with increasing H<sub>2</sub>/N<sub>2</sub> plasma exposure time in samples (b), (c), and (d). The Si-NH<sub>2</sub> peak decreased, whereas the CH=NH peak did not decrease when these samples were exposed to air. These results imply that Si-NH<sub>2</sub> bonds react with moisture and that CH=NH bonds remain in porous SiOCH films exposed to air. In the case of N<sub>2</sub> plasma, light did not form any nitrogen-containing bonds. Slight change was observed for sample (b) during exposure to the N<sub>2</sub> plasma. Si-NH<sub>2</sub> and CH=NH peaks increased with increasing N<sub>2</sub> plasma exposure time in samples, (c), and (d). Obvious change was not observed when these samples were exposed to air. These results imply that Si-NH<sub>2</sub> bonds react with moisture and that CH=NH bonds remain in porous SiOCH films exposed to air.



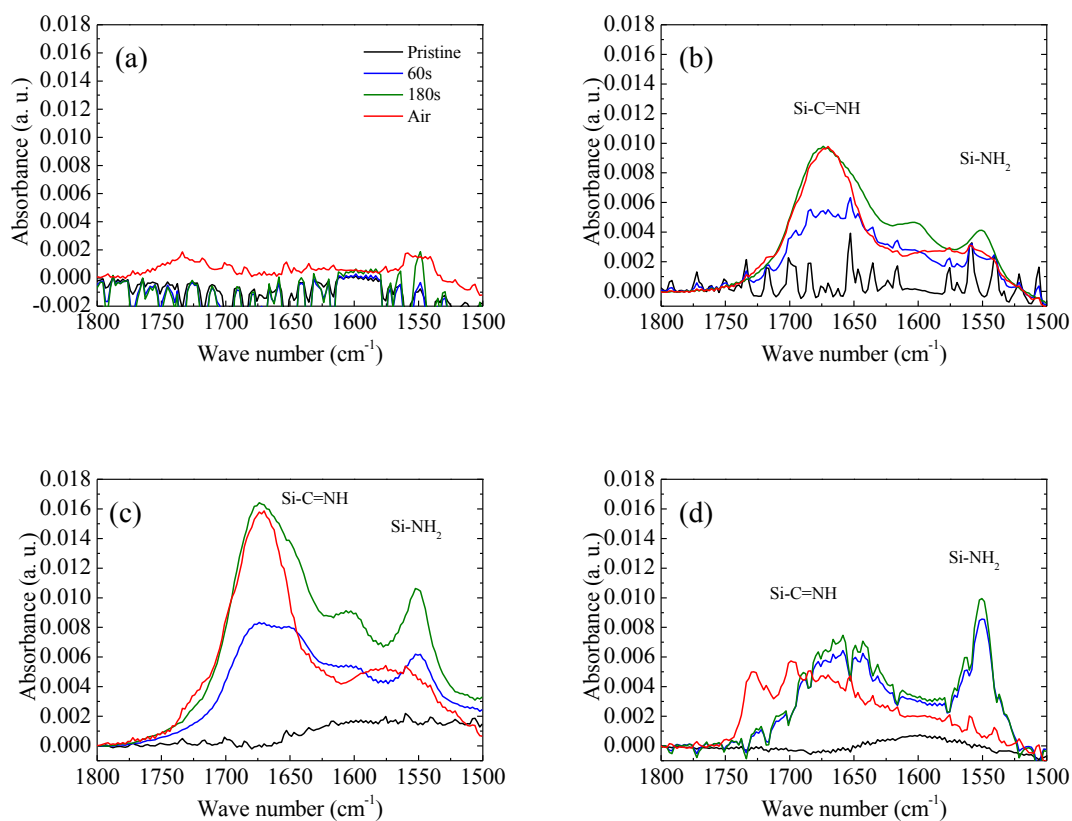


Fig. 5.13 FTIR-RAS spectra in the range 1800-1500  $\text{cm}^{-1}$  of porous SiOCH films during  $\text{H}_2/\text{N}_2$  plasma exposure and after subsequent exposure to air for: (a) light, (b) radicals, (c) light + radicals, and (d) light + radicals + ions.

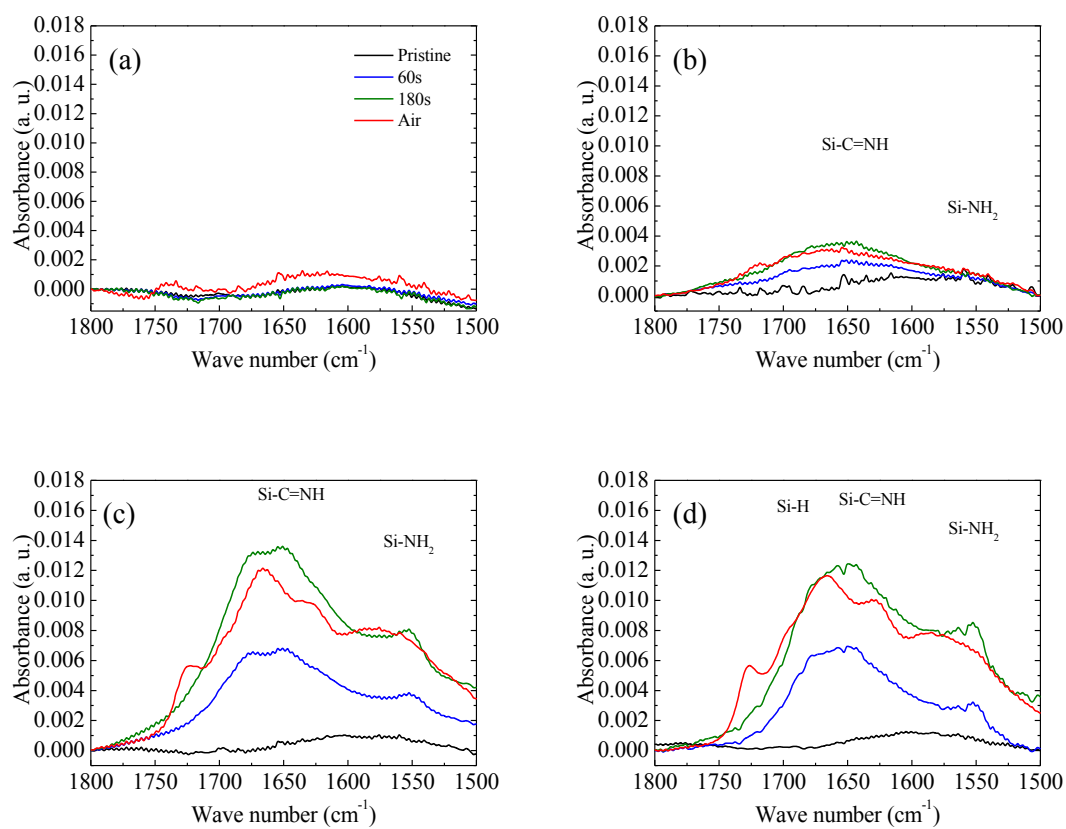


Fig. 5.14 FTIR-RAS spectra in the range 1800-1500  $\text{cm}^{-1}$  of porous SiOCH films during  $\text{N}_2$  plasma exposure and after subsequent exposure to air for: (a) light, (b) radicals, (c) light + radicals, and (d) light + radicals + ions.

Figures 5.15 and 5.16 show FTIR-RAS spectra in the range  $2500 - 2000 \text{ cm}^{-1}$  of porous SiOCH films during exposure to  $\text{H}_2$  or  $\text{H}_2/\text{N}_2$  plasmas for 60 - 180 s and subsequent exposure to air for different conditions. In the case of  $\text{H}_2$  plasma exposure, even though sample (a) was irradiated by only light, the Si-H peak increased with increasing plasma exposure time. This may be due to hydrogen-containing radicals reacting with dangling bonds. The Si-H peak in sample (b) radiated by radicals increased slightly during plasma exposure. The Si-H peak in samples (c) and (d) increased after  $\text{H}_2$  plasma exposure for 60 s; it then decreased after plasma exposure for 180 s. No obvious changes were observed after samples (a), (b), and (d) had been exposed to air. The Si-H peak in sample (c) decreased after exposure to air. No obvious changes were observed in sample (a) during  $\text{H}_2/\text{N}_2$  plasma exposure. The Si-H peak increased slightly in sample (b) after plasma exposure. Si-H peaks in samples (c) and (d) increased with increasing  $\text{H}_2/\text{N}_2$  plasma exposure time. Interestingly, the Si-H peak in these samples decreased drastically after exposure to air, which implies that Si-H bonds formed by the  $\text{H}_2/\text{N}_2$  plasma react with moisture. The Si-H peak for sample (c) was larger than that in sample (b) after exposure to both  $\text{H}_2$  and  $\text{H}_2/\text{N}_2$  plasmas. This indicates that radicals formed Si-H bonds and that light enhanced Si-H bond formation during  $\text{H}_2$  or  $\text{H}_2/\text{N}_2$  plasma exposure.

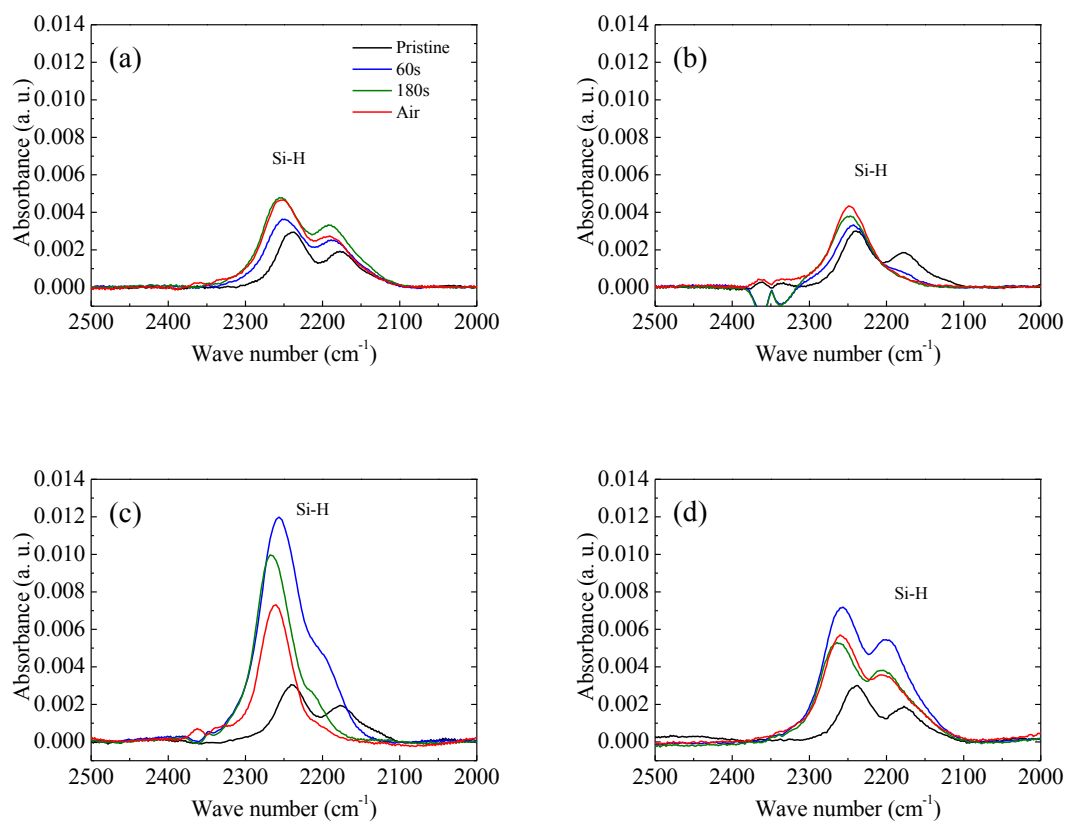


Fig. 5.15 FTIR-RAS spectra in the range 2500-2000  $\text{cm}^{-1}$  of porous SiOCH films during  $\text{H}_2$  plasma exposure and after subsequent exposure to air for: (a) light, (b) radicals, (c) light + radicals, and (d) light + radicals + ions.

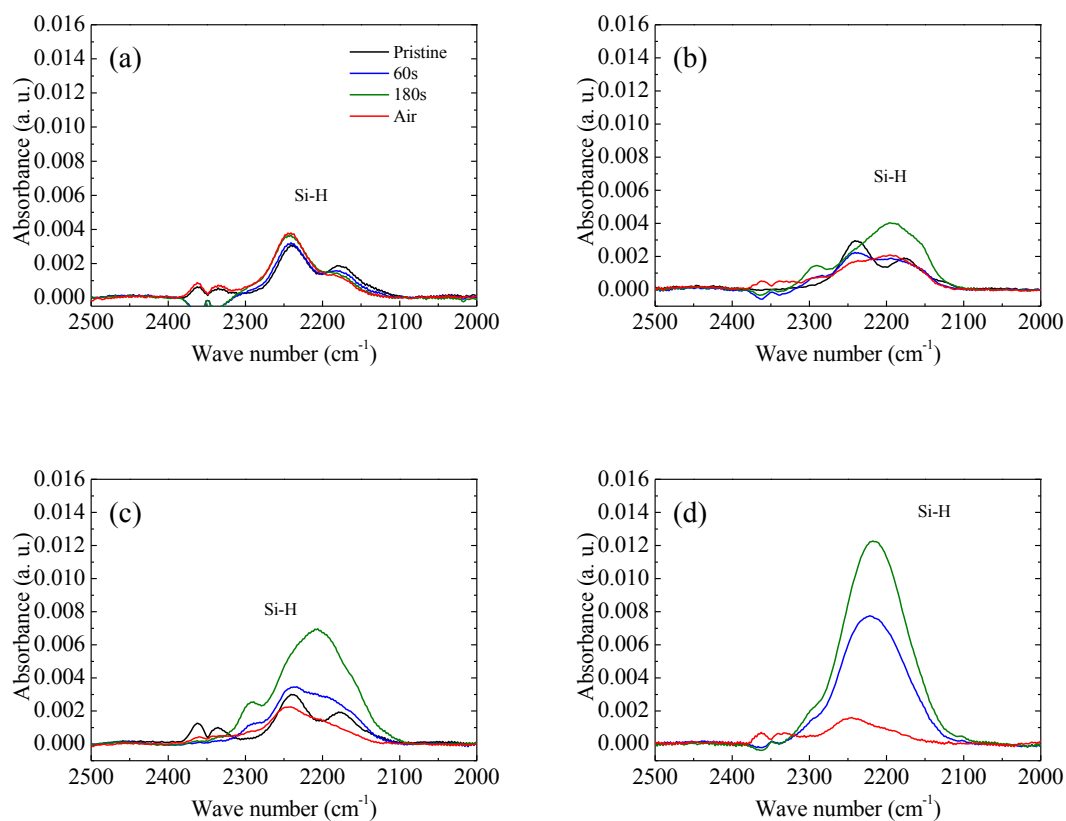


Fig. 5.16 FTIR-RAS spectra in the range 2500-2000  $\text{cm}^{-1}$  of porous SiOCH films during  $\text{H}_2/\text{N}_2$  plasma exposure and after subsequent exposure to air for: (a) light, (b) radicals, (c) light + radicals, and (d) light + radicals + ions.

### 5.3.2 Roles for Ions, Radicals, and Light Radiation Analyzed by *Ex Situ* Film Characterization

To obtain a better understanding of the plasma damage mechanism, bulk analysis by dynamic SIMS and surface analysis by XPS were performed before and after exposure to the  $H_2/N_2$  plasma. In this section, the effects of surface modification by air exposure during sample transfer after plasma processes could not be separated.

Figures 5.17(A) and (B) show the carbon and nitrogen depth profiles measured by dynamic SIMS for the porous SiOCH films after exposure to  $H_2/N_2$  plasma and air, respectively. Carbon depletion was observed to depths of about 40 and 30 nm from the surface in samples (a) and (b), respectively. Low carbon depletion was observed on the surface of sample (c). Carbon depletion was not observed in sample (d). Nitrogen was strongly observed about 5 nm from the surface and weakly observed in the bulk of sample (a). For samples (b) and (c), nitrogen was weakly observed in the bulk. Nitrogen was not observed in sample (d). These results confirm that the extraction of methyl by radicals occurred from the film surface and was enhanced by light and adding ions increase the extraction of methyl. The SIMS data reveal that the porous SiOCH film exposed to  $H_2/N_2$  plasma has a layer that been highly damaged by radicals and ions and a layer that had been slightly damaged by light after  $H_2/N_2$  plasma exposure.

Figure 5.18 shows the surface compositions calculated from XPS spectra [Si (2p), C (1s), O (1s), N (1s)] of the porous SiOCH films before and after  $H_2/N_2$  plasma exposure. In samples (b), (c), and (d), the oxygen concentration on the porous SiOCH surface had increased whereas carbon depletion had decreased after  $H_2/N_2$  plasma exposure. On top of that, small amounts of nitrogen were detected on samples (b), (c), and (d). No obvious changes in the atomic composition were observed for sample (a). These results also support the conclusions that the radicals extract methyl from the surface and that light alone does not have much impact on the surface.

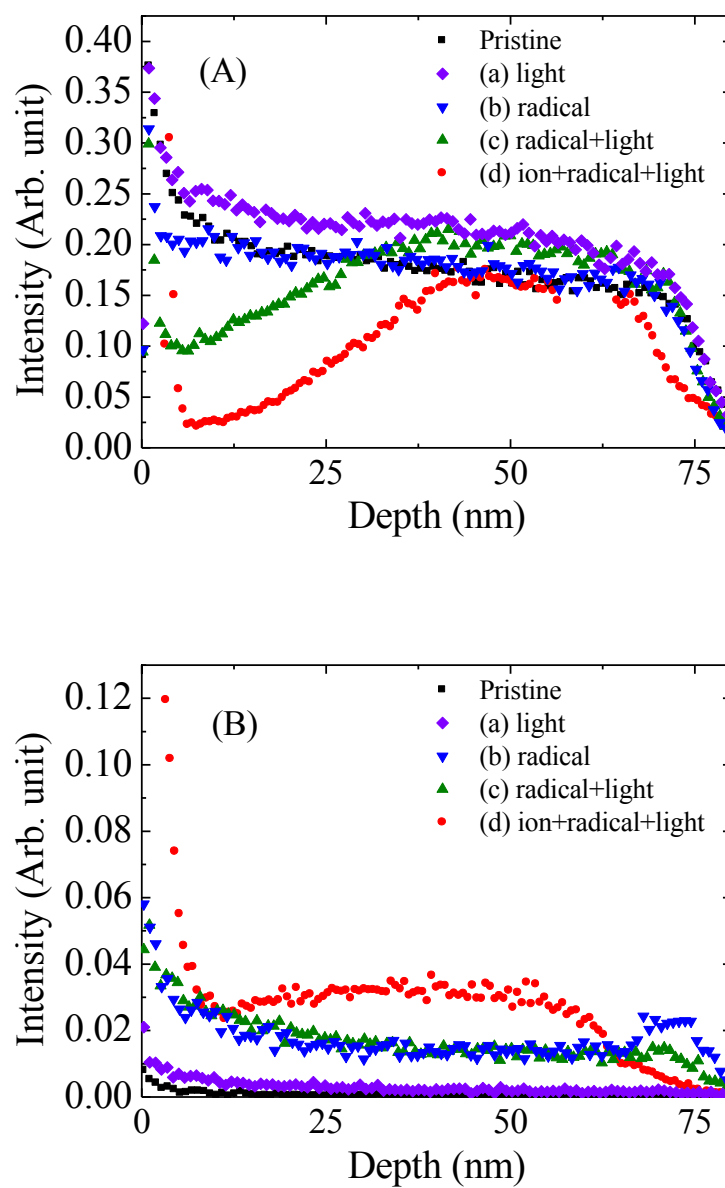


Fig. 5.17 (A) Carbon and (B) Nitrogen depth profiles of porous SiOCH films obtained by dynamic SIMS.

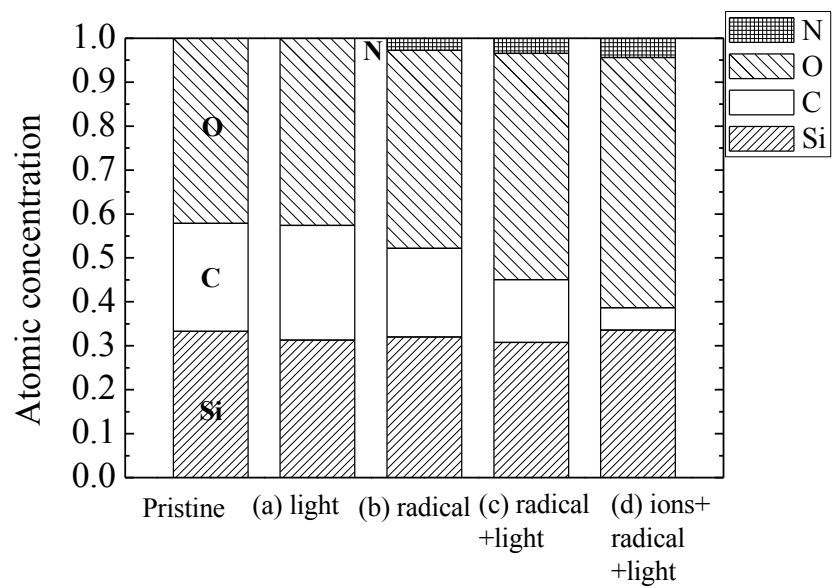


Fig. 5.18 Surface compositions of porous SiOCH films obtained by XPS.



### 5.3.3 Modification of Si-O-Si Structure in Porous SiOCH Films by Ions, Radicals, and Light Radiation

To investigate the modification of Si-O-Si structures in the porous SiOCH films, IR absorption in the range 985-1250  $\text{cm}^{-1}$  was decomposed into three bands with peaks at 1035, 1065, and 1149  $\text{cm}^{-1}$ , which correspond to linear, network, and cage structures, respectively [13,16,17]. Cage structure is a three-dimensional structure, and contains basically one methyl group. Network structure is also a three-dimensional structure doesn't contain basically methyl group. Linear structure is a two-dimensional structure contains mainly two basically group. For comparison with reported transmission spectra, we calculated absorption spectra by using the Fresnel equation using the dielectric function of porous SiOCH films extracted from measured reflection spectra. Each Si-O-Si structure and deconvoluted absorption peak is shown in Fig. 5.19.

Figures 5.20 and 5.21 show the relative proportions of the individual components described above such as the linear, network, and cage structures in porous SiOCH films after  $\text{H}_2$  or  $\text{H}_2/\text{N}_2$  plasma exposure for 180 s and subsequent air exposure. The variation in these three peak area ratios was investigated during plasma exposure and air exposure.

In the case of  $\text{H}_2$  plasma exposure, the cage structure decreased, whereas the linear structure increased remarkably after sample (a) was exposed to the plasma. This implies that light breaks Si-O-Si bonds, generating Si-O dangling bonds; these Si-O dangling bonds are then detected as linear structures. A slight change was observed during  $\text{H}_2$  plasma exposure of sample (b). This result agrees well with the amount of residual silicon-methyl bonds.

In sample (c), linear and network structures increased, whereas the cage structure decreased during plasma exposure. The linear and cage structures decreased, while the network structure increased in sample (d). For all four samples, the ratio of

linear structures decreased, while the ratios of cage and network structures increased on exposure to air. These ratios changed dramatically for sample (c). The network structure decreased and the cage structure increased during  $H_2/N_2$  plasma exposure of sample (a) (which was irradiated only by light emitted by the plasma). A slight change was observed during plasma exposure of samples (a) and (b). The linear and cage structures decreased and the network structure increased during plasma exposure of sample (d). For all four samples, the ratio of the linear structure decreased and the ratio of the cage structure increased on exposure to air. This change was remarkable for sample (d). The difference in the behaviors of sample (d) obtained during air exposure after exposure to  $H_2$  and  $H_2/N_2$  plasmas is considered to be due to the shrieked layer on top of the film being altered by the  $H_2$  plasma.

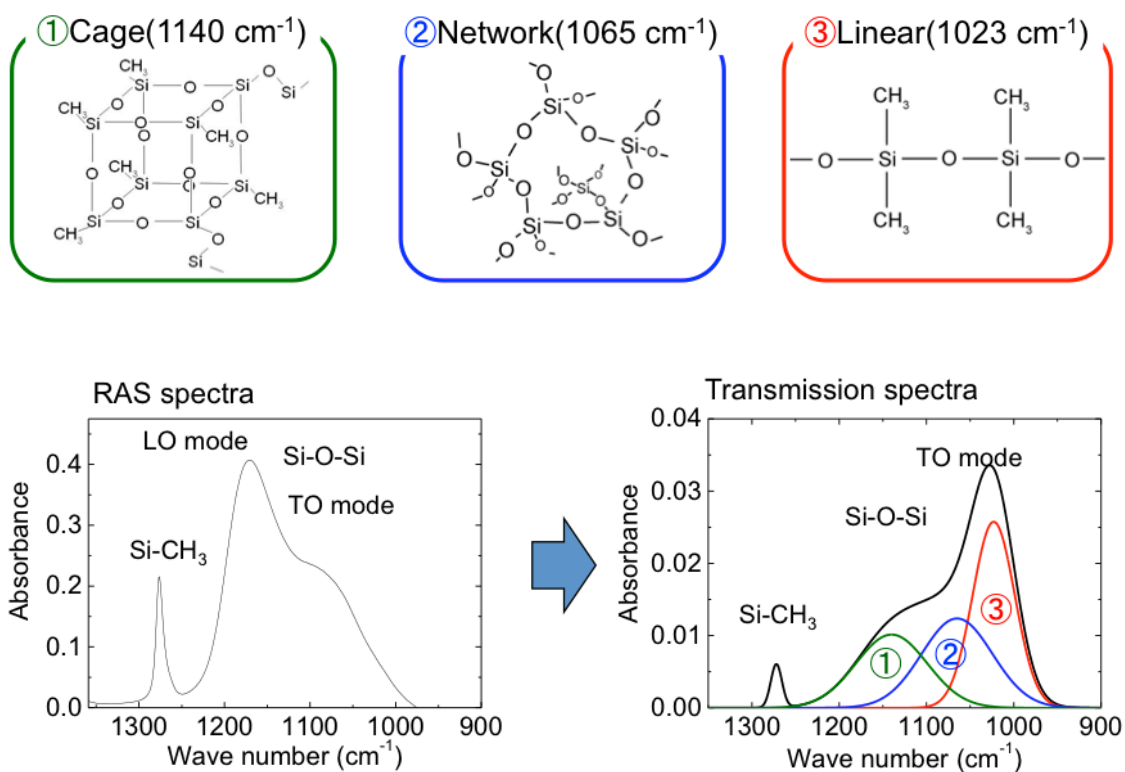


Fig. 5.19 Diagrams of each Si-O-Si structure and deconvoluted absorption peak.

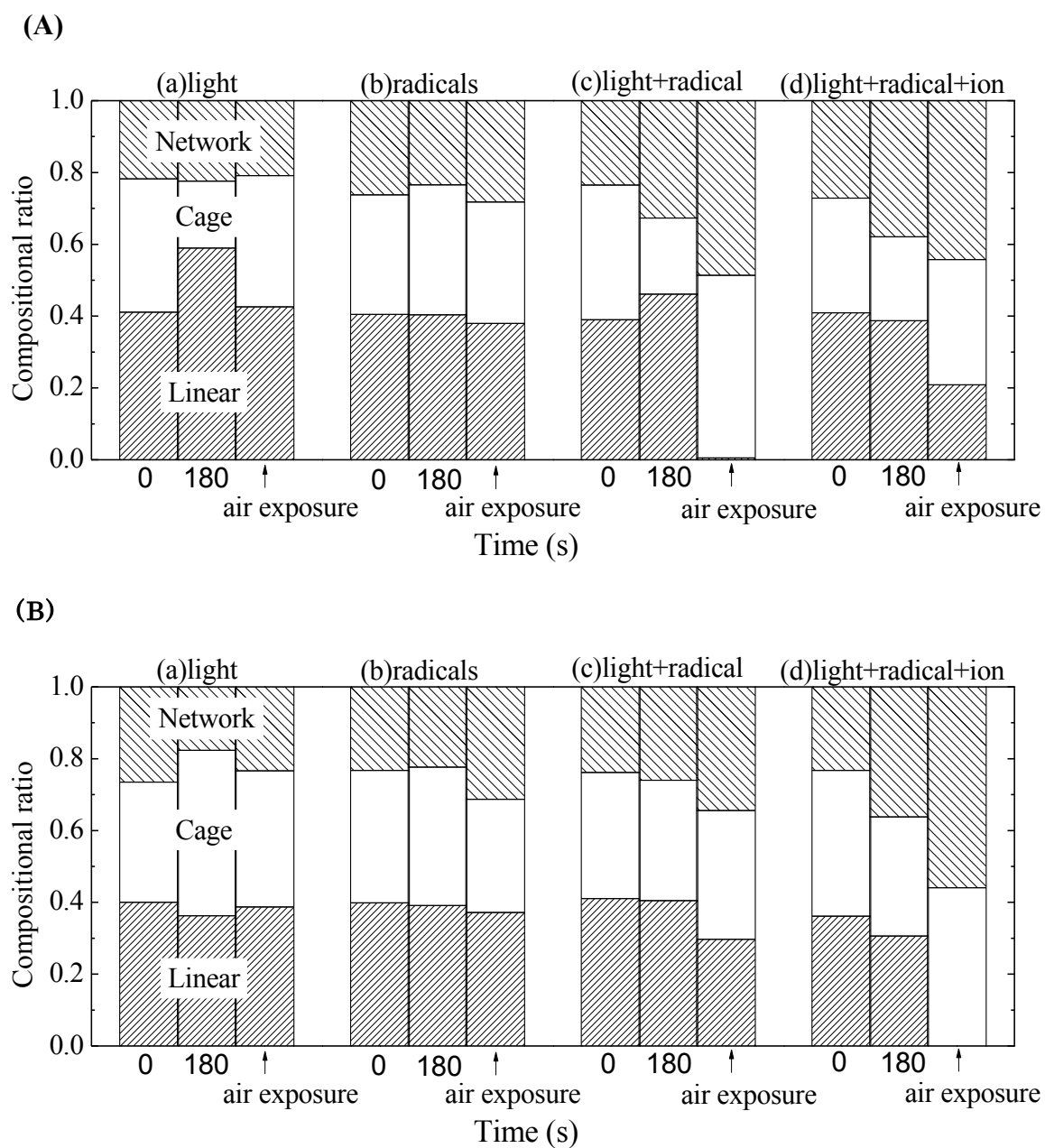


Fig. 5.20 Relative proportions of Si-O-Si structures in porous SiOCH films during (A)  $\text{H}_2$  plasma and (B)  $\text{H}_2/\text{N}_2$  plasma exposure and after subsequent exposure to air.

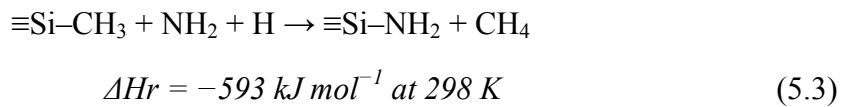
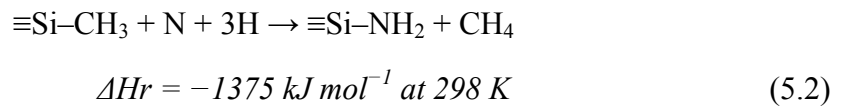
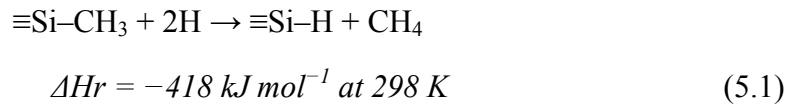
### 5.3.4 H<sub>2</sub>/N<sub>2</sub> Plasma Damage Mechanism of Porous SiOCH Films

In the case of the H<sub>2</sub>/N<sub>2</sub> plasma, XPS and dynamic SIMS analysis revealed that the surface of the porous SiOCH films was a nitride due to N radicals. Although light transmits through the thin nitride layer and the H radical density was higher than in the H<sub>2</sub> plasma, fewer Si-CH<sub>3</sub> bonds were broken by H<sub>2</sub>/N<sub>2</sub> plasma exposure since the light flux was low in the H<sub>2</sub>/N<sub>2</sub> plasma and the nitride layer inhibits diffusion of H radicals. Therefore, the variations in the thickness, refractive index, and Si-CH<sub>3</sub> bond absorption of the porous SiOCH films after H<sub>2</sub>/N<sub>2</sub> plasma exposure were smaller than those of the film exposed to the H<sub>2</sub> plasma.

The experimental results in the previous section reveal the effect of ions, radicals, and light in H<sub>2</sub> and H<sub>2</sub>/N<sub>2</sub> plasmas. In this section, we propose models for the plasma damage mechanism.

#### Role of Radicals

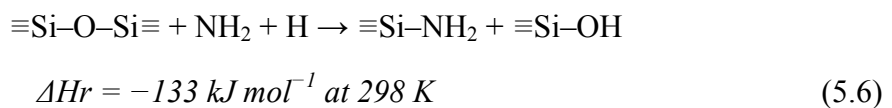
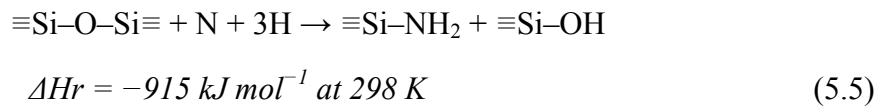
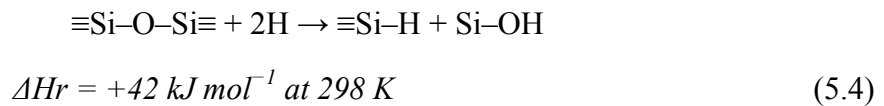
Radicals in H<sub>2</sub> and H<sub>2</sub>/N<sub>2</sub> plasmas (e.g., N<sub>x</sub>H<sub>y</sub>, H, and N radicals) can break silicon-methyl bonds in porous SiOCH films, leading to Si-H and Si-NH<sub>2</sub> bonds being formed by the following reactions:



As these equations show, H radicals break silicon-methyl bonds. Reaction (5.1) occurs

preferentially since its enthalpy ( $\Delta H_r$ ) is more negative than those of the other reactions. This reaction occurs from the surface to bulk, as the SIMS data shows. The porous SiOCH films consist of damaged and non-damaged layers after H radical exposure. The displacement of the Si-CH<sub>3</sub> bond to the Si-H bond by H radicals reduces the density and increases the polarizability of the damaged layer. The reduction in the density offsets the effect of the increase in the polarizability on the refractive index of the damaged layer, since the refractive index is determined by both the polarizability and the density [18]. The extraction of -CH<sub>3</sub> by radicals, leads to the formation of Si-NH<sub>2</sub> and Si-H bonds on porous SiOCH films. The enthalpies of reactions (5.2) and (5.3) are more negative than that of reaction (5.1), indicating that Si-NH<sub>2</sub> bonds are preferentially formed by radicals in the H<sub>2</sub>/N<sub>2</sub> plasma. These inferences are consistent with the variations in the Si-CH<sub>3</sub> and Si-NH<sub>2</sub> bond absorptions shown in Figs. 5.5(B) and 5.12, which indicate that H radicals and nitrogen-containing species can reduce Si-CH<sub>3</sub> bonds.

The experimental results shown in Figs. 4.31 and 4.32 reveal that Si-O-Si structures in porous SiOCH films were modified during plasma exposure. Previous studies also suggest that H radicals and nitrogen-containing species can break Si-O-Si bonds, leading to the formation of Si-H, Si-NH<sub>2</sub>, and Si-OH bonds, as shown by the following reactions: [3,8,9]

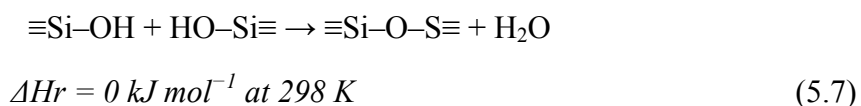


Reaction (5.4) has a higher enthalpy than reaction (5.1), which implies that breaking of Si-O-Si bonds by H radicals is energetically unfavorable. However, reaction (5.4) is supported by the results for the change in the Si-O-Si structure and the increase in the Si-H and Si-OH peaks during H<sub>2</sub> plasma exposure shown in Figs. 5.20(A), 5.10(b), and 5.15(b). Reaction (5.5) has a higher enthalpy than reaction (5.2), while reaction (5.6) has a higher enthalpy than reaction (5.3), indicating that N and H radicals break Si-CH<sub>3</sub> bonds more easily than Si-O-Si bonds. However, Figs. 5.20(B), 5.11(b), and 5.13(b) suggest that reactions (5.5) and (5.6) may also occur on porous SiOCH films during H<sub>2</sub>/N<sub>2</sub> plasma exposure. Schematic model of these reactions on the porous SiOCH films is shown in Fig. 5.21.

The reduction in the amount of Si-CH<sub>3</sub> bonds and the modification of the Si-O-Si structure in porous SiOCH films during H<sub>2</sub> plasma exposure was larger than that during H<sub>2</sub>/N<sub>2</sub> plasma exposure. This is despite the facts that the above chemical reactions imply nitrogen-containing species react more easily with these bonds than H radicals and the H<sub>2</sub>/N<sub>2</sub> plasma has a higher H radical density than the H<sub>2</sub> plasma.

These results indicate that nitrogen-containing species inhibit the reaction of Si-CH<sub>3</sub> and Si-O-Si bonds by forming nitride layers on the film surface during H<sub>2</sub>/N<sub>2</sub> plasma exposure and/or that the H<sub>2</sub> plasma generates a higher VUV intensity than the H<sub>2</sub>/N<sub>2</sub> plasma, which enhances bond breaking. Since this consideration is consistent with the detection of CH=NH bonds during H<sub>2</sub>/N<sub>2</sub> plasma exposure (see Fig. 5.10), CH=NH bonds are considered to be the main constituent of nitride layers, which inhibit the extraction of methyl by H radicals.

The Si-O-Si structure is modified by reactions (4)–(6) and the following subsequent dehydroxylation reaction: [3,19,20]



This reaction indicates that two silanol groups form a cross-link to produce a Si–O–Si structure. In fact, our experimental results reveal that the amount of Si–OH bonds increased during plasma exposure and that some Si–OH bonds simultaneously react with each other to form a Si–O–Si network structure.

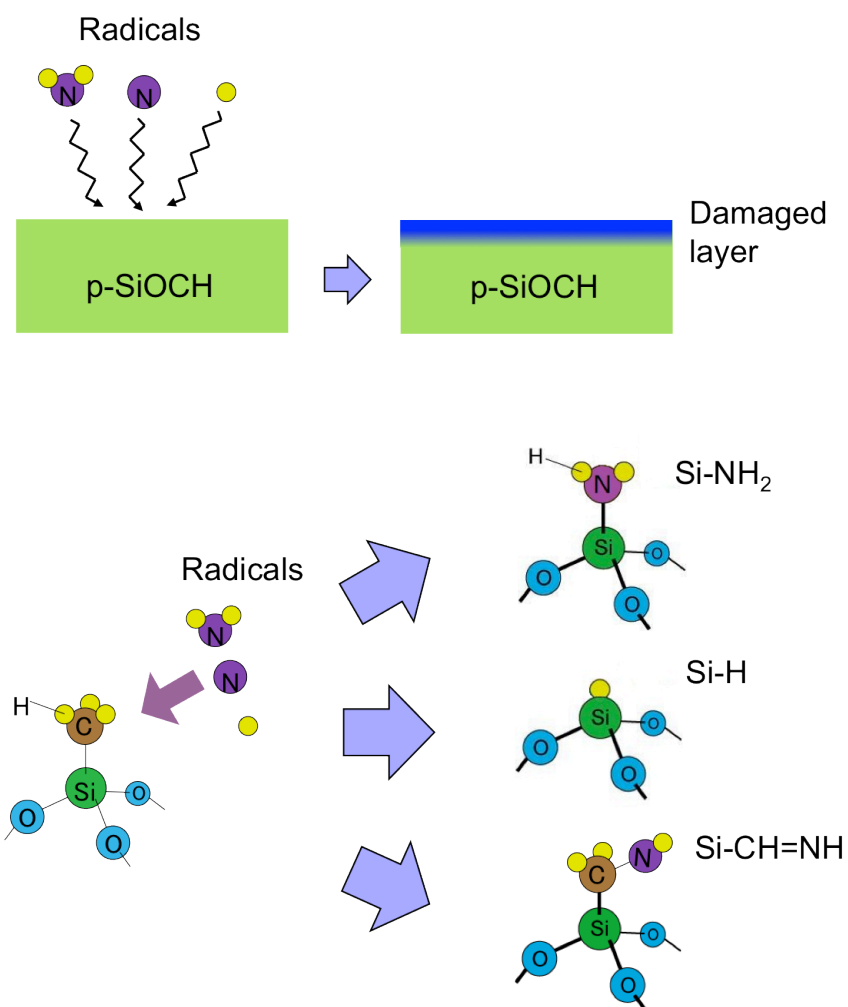


Fig. 5.21 Schematic model of damage mechanism on porous SiOCH film by Radicals.

**Role of Light**

Light radiation can break Si-CH<sub>3</sub> and Si-O-Si bonds producing dangling bonds by photoexcitation of bonds. *In situ* spectroscopic ellipsometry and *ex situ* dynamic SIMS results reveal that this reaction occurs throughout the films during plasma exposure. Light radiation accelerates the extraction of methyl in the porous SiOCH films by H radicals. As this reaction progresses, greatly damaged regions start to shrink. The shrunken regions will become dense like a film. No obvious change in the refractive indices of samples (a) and (c) was observed since the effect of methyl extraction offsets the effect of shrinkage on the refractive index (see Fig. 5.4).

The H<sub>2</sub> plasma generates a considerably greater VUV intensity than the H<sub>2</sub>/N<sub>2</sub> plasma. VUV radiation can break Si-C and Si-O bonds. These results are consistent with the results for residual Si-CH<sub>3</sub> bonds in sample (a) after H<sub>2</sub> or H<sub>2</sub>/N<sub>2</sub> plasma exposure (see Figs. 5.5(A) and (B)), which indicate that light generated by the H<sub>2</sub> or H<sub>2</sub>/N<sub>2</sub> plasma broke Si-CH<sub>3</sub> and Si-O-Si bonds. This implies the generation of dangling bonds in the films. Since Si-O and Si-C dangling bonds are very unstable, they easily react with the hydrogen in water molecules, which leads to the formation of Si-OH bonds [19]. This is consistent with the results for the variation in the Si-OH peak in sample (a) during exposure to air after H<sub>2</sub> plasma exposure (see Fig. 5.10). The variation in the chemical bonds in sample (c) (which was radiated by light and radicals) was larger than that in sample (b) (which was radiated by only radicals). These results indicate that VUV radiation enhances reactions (5.1)–(5.6) and the formation of dangling bonds.



**Role of Ion Bombardment**

Ion bombardment can also break Si-CH<sub>3</sub> and Si-O-Si bonds. Since the lower electrode is floating, the effect of ion bombardment on samples (d) estimated to be limited to a few nanometers in depth. However, the thickness and refractive index of sample (d) are drastically altered since ion bombardment shrinks the damaged layer by accelerating chemical reactions. The porous SiOCH film consists of a shrunken damaged layer, non-shrunken damaged layer, and a non-damaged layer after H<sub>2</sub> plasma exposure. There was a remarkable difference between the results for the variation in Si-CH<sub>3</sub> bonds and the modification of Si-O-Si structures exposed to the H<sub>2</sub>/N<sub>2</sub> plasma. The radicals that diffuse into the gap between the spacer and the film in the experiment employing PAPE are estimated to have lower densities than radicals in the plasma. In this experiment, it was difficult to investigate the effect of only ion bombardment on the porous SiOCH film. Even though the effect of ion bombardment without a bias (which was floating) was estimated to be below a few nanometers in depth, the chemical bonds in sample (d) varied considerably more than those in the other three samples in all the experiments. The combined effect of the radicals and light with ion bombardment is considered to dramatically enhance breaking of CH=NH bonds, which inhibits the extraction of methyl and thus accelerates film degradation. Schematic model of these reactions on the porous SiOCH films is shown in Fig. 5.22.

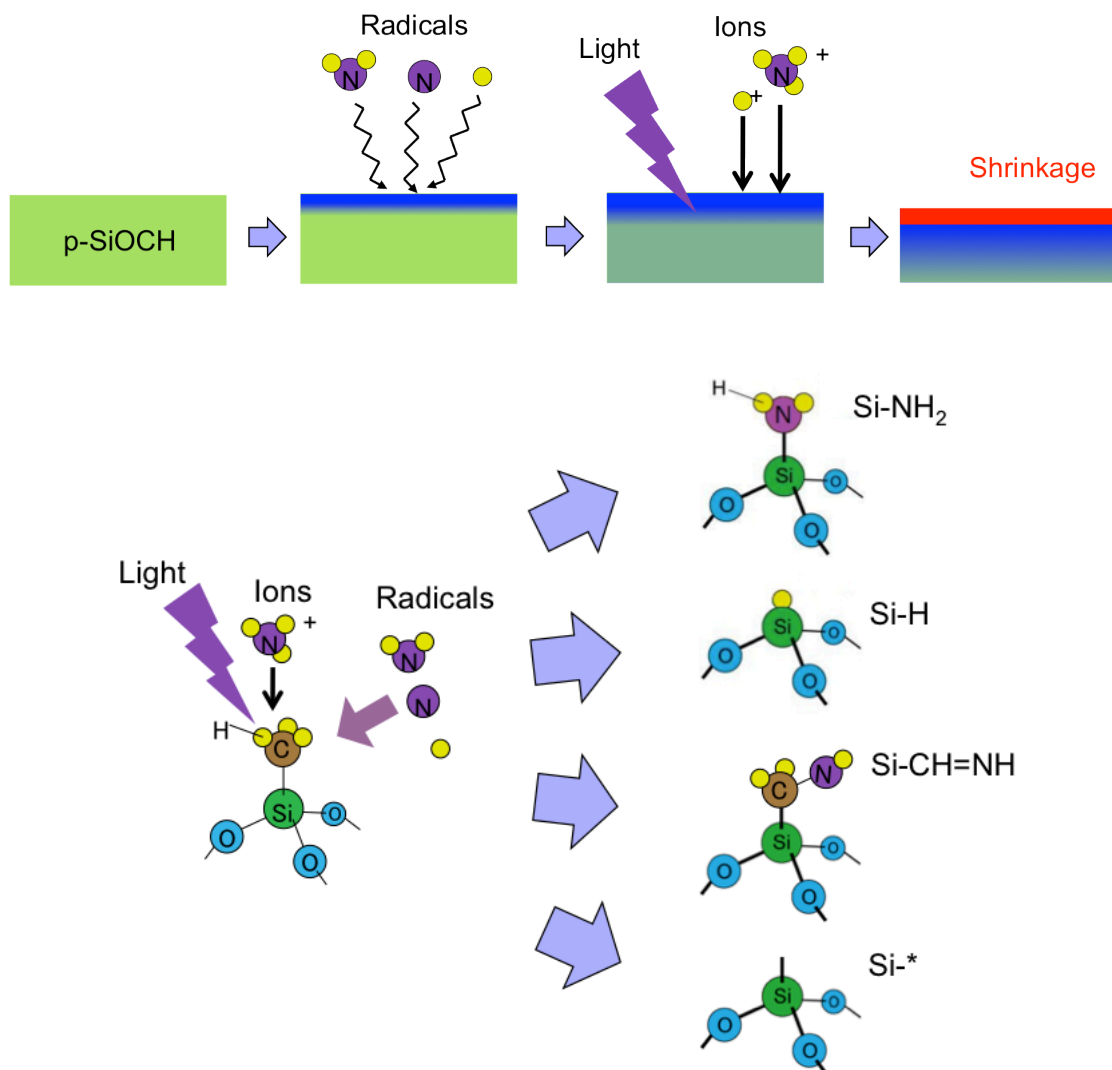
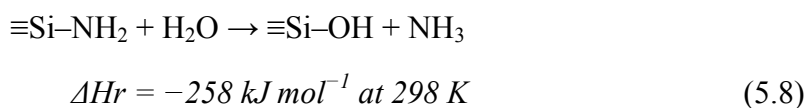


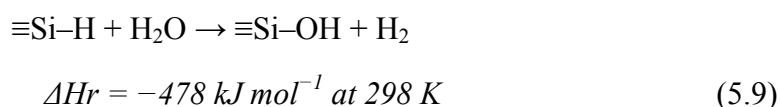
Fig. 5.22 Schematic model of damage mechanism on porous SiOCH film by light, radicals, and ions.

### Modification of Porous SiOCH Film by Air Exposure

The experimental results of this study indicate that dangling bonds created by light or ion bombardment react with moisture, resulting in the formation of Si-OH bonds and moisture uptake (see Figs 5.7 - 5.9). The moisture also reacts with Si-NH<sub>2</sub> bonds, leading to the formation of Si-OH bonds according to the following chemical reaction: [3]



This occurrence of this reaction is supported by the increase in the Si-OH peak and the decrease in the Si-NH<sub>2</sub> peak observed after air exposure (see Figs. 5.11 and 5.13). Moreover, as shown in the result for only air exposure after the experiment of (c, light and radical), we point out that the reduction of Si-H peak takes place. We believe that the characteristic changes after synergistic irradiation of both light and radical maybe resulted to modify bond-environment to remove easily chemical groups bound to Si (as -NH<sub>2</sub> and -H). One assumes that the Si-H is substantially stable, because of no observation in decrease of Si-H for pristine films, samples (a), and (b). However, as shown in Fig. 5.15(c), we can recognize that the spectral features for Si-H are shifted to higher frequencies. This means that hydrides such as Si-H<sub>2</sub> and Si-H<sub>3</sub> might be formed during the synergistic irradiation in the case. As the results, we suppose that the higher hydrides might have lower activation energy of hydroxyl formation. So we propose the following possible reaction based on the experimental results:



Consequently, exposing the porous SiOCH films treated by  $H_2/N_2$  plasma to air enhances the formation of Si-OH bonds from Si-NH<sub>2</sub>. The formation of Si-OH bonds during air exposure leads to dehydroxylation of Si-OH, which modifies the Si-O-Si structures. This agrees well with a result in our previous study, namely that the refractive index of porous SiOCH film exposed to  $H_2/N_2$  plasma increased after air exposure. The displacement of Si-NH<sub>2</sub> or Si-H bonds to Si-OH bonds and moisture absorption during air exposure increases the polarizability, which increases of the refractive index of the film. These results imply that to prevent modification, porous SiOCH films should not be exposed to air during plasma processing, even when strong carbon depletion occurs. Schematic model of modification mechanism on Si-O-Si structure by Air exposure is shown in Fig. 5.23.

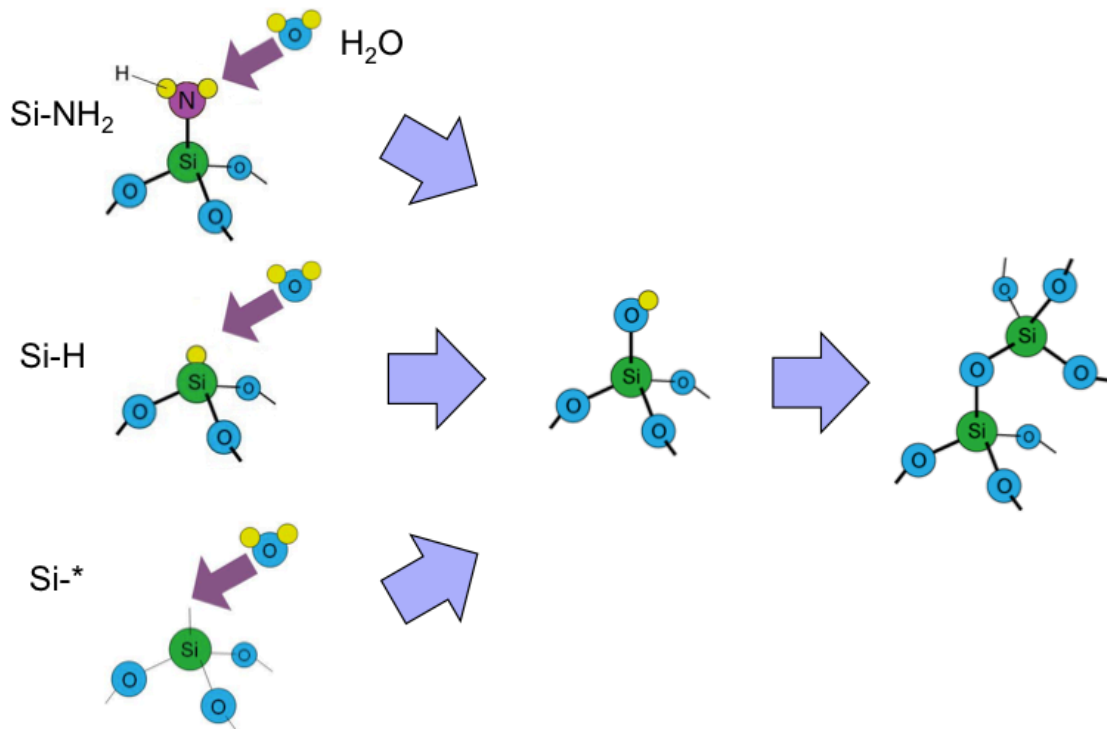


Fig. 5.23 Schematic model of modification mechanism on Si-O-Si structure by Air exposure.

## 5.4 Conclusion

The mechanism of  $\text{H}_2/\text{N}_2$  plasma damage of porous  $\text{SiOCH}$  films was investigated by the *in situ* and *ex situ* film characterization and plasma diagnostics. Since exposing porous  $\text{SiOCH}$  films to air after plasma processes modifies the films, *in situ* analysis is critical for determining the plasma damage mechanism. The effects of radicals, light, and ions generated by  $\text{H}_2$  and  $\text{H}_2/\text{N}_2$  plasmas and subsequent air exposure were investigated by the *in situ* PAPE method.

*In situ* spectroscopic ellipsometry revealed that ions, light, and the synergy between the radicals, and light reduces the thickness and increases the refractive index of the porous  $\text{SiOCH}$  films. We used *in situ* FTIR-RAS to investigate the modification of chemical bonds in porous  $\text{SiOCH}$  films induced by hydrogen-containing plasmas. *In situ* FTIR spectroscopy revealed that the extraction of methyl by radicals was enhanced by light and adding ions increase the extraction of methyl in the porous  $\text{SiOCH}$  films.

Light generated by  $\text{H}_2$  and  $\text{H}_2/\text{N}_2$  plasmas can break  $\text{Si-CH}_3$  and  $\text{Si-O-Si}$  bonds, resulting in the generation of dangling bonds. The reduction in the amount of  $\text{Si-CH}_3$  bonds by radicals results in an increase in the amount of  $\text{Si-OH}$  bonds and modification of  $\text{Si-O-Si}$  structure during plasma exposure.  $\text{Si-OH}$  bonds were formed by  $\text{Si-NH}_2$ ,  $\text{Si-H}$ , and dangling bonds reacting with moisture.

The change in  $\text{Si-O-Si}$  composition was analyzed during plasma exposure and subsequent air exposure.  $\text{Si-O-Si}$  is modified by dehydroxylation of  $\text{Si-OH}$  and termination between dangling bonds.

With confirmation by the *ex situ* SIMS and XPS results, we confirmed that porous  $\text{SiOCH}$  films exposed to  $\text{H}_2/\text{N}_2$  plasma consist of a highly damaged layer by radicals and ions and a slightly damaged layer by light after  $\text{H}_2/\text{N}_2$  plasma exposure. The VUVAS experimental results showed that the effect of extracting  $\text{Si-CH}_3$  bonds by

H radicals was drastically promoted by light radiation and ion bombardment, whereas N radicals inhibit the extraction of Si-CH<sub>3</sub> bonds by forming a nitride layer. The breaking of Si-CH<sub>3</sub> bonds by H radicals reduces the density and increases the polarizability of the damaged layer. Ion bombardment causes the damaged layer to shrink by breaking Si-C and Si-O-Si bonds.

These results imply that to prevent modification, porous SiOCH films should not be exposed to air just after plasma processing, even when strong carbon depletion occurs. The information provided by these *in situ* experiments is expected to be very useful for the design and processing of low-*k* materials.

## 5.5 References

- [1] M. Fukasawa, T. Hasegawa, S. Hirano, and S. Kadomura: Proc. Symp. Dry Process, 1998, p. 175.
- [2] K. Maex, M. R. Baklanov, D. Shamiryan, F. Iacopi, S. H. Brongersma, and Z. S. Yanovitskaya, J. Appl. Phys. **93**, 8793 (2003).
- [3] N. Posseme, T. Chevolleau, T. David, M. Darnon, O. Louveau, and O. Joubert, J. Vac. Sci. Technol. B **25**, 1928 (2007).
- [4] J. Bao, H. Shi, J. Liu, H. Huang, P. S. Ho, M. D. Goodner, M. Moinpour, and G. M. Kloster, J. Vac. Sci. Technol. B **26**, 219 (2008).
- [5] X. Hua, M. Kuo, G. S. Oehrlein, P. Lazzeri, E. Lacob, M. Andrie, C. K. Inoki, T. S. Kuan, P. Jiang, and W. Wu, J. Vac. Sci. Technol. B **24**, 1238 (2006).
- [6] S. Uchida, S. Takashima, M. Hori, M. Fukasawa, K. Ohshima, K. Nagahata, and T. Tatsumi, J. Appl. Phys. **103**, 073303 (2008).
- [7] S. Xu, C. Qin, L. Diao, D. Gilbert, L. Hou, A. Wiesnoski, E. Busch, R. McGowan, B. White, and F. Weber, J. Vac. Sci. Technol. B **25**, 156 (2007).
- [8] M. A. Worsley, S. F. Bent, S. M. Gates, N. C. Fuller, W. Volksen, M. Steen, and T. Dalton, J. Vac. Sci. Technol. B **23**, 395 (2005).
- [9] H. Cui, R. J. Carter, D. L. Moore, H. G. Peng, D. W. Gidley, and P. A. Burke, J. Appl. Phys. **97**, 113302 (2005).
- [10] B. Jinnai, T. Nozawa, and S. Samukawa, J. Vac. Sci. Technol. B **26**, 1926 (2008).
- [11] K. Takeda, Y. Miyawaki, S. Takashima, M. Fukasawa, K. Oshima, K. Nagahata, T. Tatsumi, and M. Hori, J. Appl. Phys. **109**, 033303 (2011).
- [12] A. Grill and D. A. Neumayer, J. Appl. Phys. **94**, 6697 (2003).
- [13] *Handbook of Infrared and Raman Characteristic Frequencies of Organic Molecules*, edited by D. Lin-Vien, D. L. Vieh, N. B. Colthup, W. G. Fateley, and J. G. Grasselli. (Academic Press, San Diego, 1991), p. 162, p. 200.

- [14] J. Olivares-Roza, O. Sanchez, and J. M. Albella, *J. Vac. Sci. Technol. A* **16**, 2757 (1998).
- [15] Y Zhang, *J. Molecular Catalysis A: Chemical* **118**, 205 (1997).
- [16] A. Grill and D. A. Neumayer, *J. Appl. Phys.* **94**, 6697 (2003).
- [17] S. Yasuhara, J. Chung, K. Tajima, H. Yano, S. Kadomura, M. Yoshimaru, N. Matsunaga, and S. Samukawa, *J. Phys. D: Appl. Phys.* **42**, 235201 (2009).
- [18] T. Yagi, M. Susa, and K. Nagata *J. Non-Cryst. Solids*, **54**, 315 (2003).
- [19] T. C. Chang, P. T. Liu, Y. S. Mor, T.M. Tsai, C.W. Chen, Y. J. Mei, F. M. Pan, W. F. Wu, and S. M Sze, *J. Vac. Sci. Technol. B* **20**, 1561 (2002).
- [20] E. A. Wovchko, J. C. Camp, J. A. Glass, Jr., and J. T. Yates, Jr. *Langmuir* **11**, 2592. (1992).



## Chapter 6      Conclusions and Future Works

### 6.1 Conclusions of Present Research

The motivation of this thesis was to understand chemical reaction between plasma and low- $k$  materials and to realize highly precise etching. We have constructed a smart plasma process system based on *in situ* film characterization and plasma diagnostics and substrate temperature measurement system. This study also investigated plasma modification mechanism of the low- $k$  materials and to realize highly precise and damage less processing of the low- $k$  materials.

In Chapter 1, the trend in future scaled integrated circuits and the necessity of low- $k$  materials were shown as introduction. The necessity for plasma processing in the fabrication of electronics device was also introduced. For the first initiative innovation of etching process development, new approach based on control of internal parameter was proposed to overcome the problem induced by conventional process. The concept of high precision plasma processing and purpose of this thesis were also described.

In Chapter 2, the experimental system for diagnostic techniques of plasma and analysis of surface reaction on etched film are described. Theories of plasma diagnostics such as VUVAS and microwave Interferometer were described. Theories of film characterization technique such as spectroscopic ellipsometry, X-ray photoelectron spectroscopy (XPS) and a Fourier transform infrared reflection absorption spectroscopy (FTIR-RAS) used as measurement methods of etched surface reactions were introduced.

In Chapter 3, we developed a new plasma etch process for precise feature control of organic films by control of radical densities and substrate temperature. Low- $k$  organic films were etched using a dual-frequency CCP etching reactor employing a gas mixture of  $H_2/N_2$ . Absolute H and N radical densities were measured by VUVAS, and

substrate temperature was measured using an optical-fiber-type low-coherence interferometer during precise low- $k$  organic film etching. We have successfully measured substrate temperature in real time during the etching process. It was found that substrate temperature increased with increasing H radical density ratio of  $H/(H+N)$ . On the basis of these measurements, the etching profiles of low- $k$  organic films were investigated using SEM. We developed a new process that can change the radical density ratio step by step based on experimental results. The amount of bowing on the sidewall decreased markedly with the new process. XPS analysis confirmed that nitride layers formed at low substrate temperatures by nitrogen-related species protect films against sidewall etching. We have succeeded in the control of the etched profile of low- $k$  films precisely using internal parameters of plasma processing.

In Chapter 4, the effect of remained fluorocarbon layer and air exposure after plasma exposure on porous low- $k$  SiOCH film were investigated. Refractive index, thickness in porous SiOCH film was investigated during plasma treatment and subsequent air exposure. We revealed that *in situ* evaluation is crucial for the clarification of damage generation mechanism because the damaged low- $k$  films are modified during exposing to atmosphere. On top of that, plasma analysis such as VUVAS was performed. The film characterization and plasma analysis revealed the plasma damage mechanism of porous low- $k$  SiOCH films.

In Chapter 5, investigated the mechanism of  $H_2/N_2$  plasma ashing damage of porous SiOCH films, focusing on *in situ* analysis. The mechanism of plasma ashing damage on the porous SiOCH films was investigated by *in situ* Fourier transform infrared reflection absorption spectroscopy. Since exposing porous SiOCH films to air after plasma processes modifies the films, *in situ* analysis is critical for determining the plasma damage mechanism. The effects of radicals, light, and ions generated by  $H_2$  and  $H_2/N_2$  plasmas and subsequent air exposure were investigated by the *in situ* PAPE method. *In situ* spectroscopic ellipsometry revealed that ions, light, and the synergy

between the radicals, and light reduces the thickness and increases the refractive index of the porous SiOCH films. We used *in situ* FTIR-RAS to investigate the modification of chemical bonds in porous SiOCH films induced by hydrogen-containing plasmas. *In situ* FTIR spectroscopy revealed that the extraction of methyl by radicals was enhanced by light and adding ions increase the extraction of methyl in the porous SiOCH films. Light generated by H<sub>2</sub> and H<sub>2</sub>/N<sub>2</sub> plasmas can break Si-CH<sub>3</sub> and Si-O-Si bonds, resulting in the generation of dangling bonds. The reduction in the amount of Si-CH<sub>3</sub> bonds by radicals results in an increase in the amount of Si-OH bonds and modification of Si-O-Si structure during plasma exposure. Si-OH bonds were formed by Si-NH<sub>2</sub>, Si-H, and dangling bonds reacting with moisture. The change in Si-O-Si composition was analyzed during plasma exposure and subsequent air exposure. Si-O-Si is modified by dehydroxylation of Si-OH and termination between dangling bonds. With confirmation by the *ex situ* SIMS and XPS results, we confirmed that porous SiOCH films exposed to H<sub>2</sub>/N<sub>2</sub> plasma consist of a highly damaged layer by radicals and ions and a slightly damaged layer by light after H<sub>2</sub>/N<sub>2</sub> plasma exposure. The VUVAS experimental results showed that the effect of extracting Si-CH<sub>3</sub> bonds by H radicals was drastically promoted by light radiation and ion bombardment, whereas N radicals inhibit the extraction of Si-CH<sub>3</sub> bonds by forming a nitride layer. The breaking of Si-CH<sub>3</sub> bonds by H radicals reduces the density and increases the polarizability of the damaged layer. Ion bombardment causes the damaged layer to shrink by breaking Si-C and Si-O-Si bonds. These results imply that to prevent modification, porous SiOCH films should not be exposed to air during plasma processing, even when strong carbon depletion occurs. The information provided by these *in situ* experiments is expected to be very useful for the design and processing of low-*k* materials.

## 6.2 Scopes for Future Works

In this thesis, plasma etching process of low- $k$  materials for fine pattern profile and less damage process were studied based on *in situ* film characterization and plasma diagnostics. To understand plasma etch process, it is necessary to evaluate the behavior of internal parameters produced as a function of various process conditions and information about target materials. If it possible to understand the behaviors of internal parameters and those effects on the film properties, it helps our understanding on plasma chemistry.

Low- $k$  organic films were etched using a dual-frequency (100 MHz/2 MHz) CCP etcher employing a gas mixture of  $H_2/N_2$ . H and N radical densities were measured by VUVAS, and substrate temperature was measured using an optical-fiber-type low-coherence interferometer during precise low- $k$  organic film etching. However, other information about some species would help our understanding more. If absolute quantities of etching by-products can be measured, important information on mechanisms of plasma etching will be able to be supplied. Investigation of chemical bonds in the low- $k$  organic films also should be able to give us useful information. On top of that, plasma diagnostics by multi beam study could be our next step to investigate more precisely the interaction of ions and radicals on the low- $k$  film. The complex chemistry of H, N, and  $NH_x$  ions and radicals containing plasma was simplified to investigate the interaction of ions and radicals on the low- $k$  film.

Mechanism of  $H_2/N_2$  plasma ashing damage of porous SiOCH films was investigated by *in situ* film characterization such as FTIR-RAS and spectroscopic ellipsometry and plasma diagnostics such as VUVOES and VUVAS. Based on our knowledge and understanding on plasma damage on the porous SiOCH films, damage-free plasma process could be achieved. The process based on internal parameter and our knowledge must be useful for high precise and damage-free plasma process.

Miniaturization is expected to keep going and demand for plasma process is getting harder. However, our approach to precise etching process would be able to develop semiconductor device industry. In this thesis, although the author have mainly considered ion and H, N radicals to interpret the etching characteristics, actually other internal parameters such as the energies of species, the temperature and surface reaction coefficient have to be considered for the sophisticated interpretation with reproducibility.

In near future, the establishment of Plasma Nano-Science with real-time control of the internal parameter based on *in situ* film characterization and plasma diagnostics would be expected to accelerate development for plasma etching process.



## Acknowledgements

The present research has been performed in Prof. Hori and Prof. Sekine Laboratory, Department of Electrical Engineering and Computer Science, Nagoya University. The research results presented in this thesis couldn't have been obtained without the support of the following people.

First and foremost, I would like first thank Prof. Masaru Hori, Department of Electrical Engineering and Computer Science, Nagoya University, for having given me the opportunity to pursue a Ph.D. in his group. I could not progress rapidly in my understanding of this research without His guidance, valuable advices, and encouragements. I also would like to deeply thank my co-supervisor, Prof. Makoto Sekine, Plasma Nanotechnology Research Center, Nagoya University, for providing his wealth of experience and wonderful discussions. At same time, I wish to express my sincere gratitude to the vice-adviser, Prof. Hirotaka Toyoda, Department of Electrical Engineering and Computer Science, Nagoya University, for his valuable suggestions and discussions in progressing this research. I also thank to the vice-adviser, Prof. Tatsuru Shirafuji, Department of Physical Electronics and Informatics, Osaka City University, for giving the big motivation for the passionate research.

I would like to express my appreciation to Dr. Tokuhiisa Oiwa, Dr. Itsuko Sakai, Dr. Hisataka Hayashi, Dr. Kei Hattori, Mr. Katsumi Yamamoto, Mr Takeshi Kaminatsui, Mr. Tsubasa Imamura in Toshiba Corporation, for collaborating and giving regular and valuable advices for the project of. I am also grateful to the entire staff in Hori and Sekine's Lab., Prof. Kenji Ishikawa, Associate Prof. Hiroki Kondo, Associate Prof. Satomi Tajima, Assistant Prof. Keigo Takeda, Dr. Seigo Takashima, Dr. Noboru Ebizuka, and Dr. Fengdong Jia for their fruitful discussion and valuable comments. I would like to express my gratitude to Prof. Masafumi Ito, Department of Electrical and

## Acknowledgements

Electronic Engineering, Meijo University, Prof. Mineo Hiramatsu, Department of Electrical and Electronic Engineering, Meijo University, Associate Prof. Takayuki Ohta, Department of Electrical and Electronic Engineering, Meijo University, and Mr. Masanaga Fukasawa, Sony corporation. I would like to acknowledge Dr. Shoji Den, Dr. Koji Yamakawa, Dr. Shunji Takahashi in Katagiri Engineering Co., Ltd., Dr. Hiroyuki Kano in NU Eco-Engineering Co., Ltd., and Ryota Kawauchi in COM Electronics Development Inc., for constructing and modifying the experimental equipments.

I appreciate Prof. Jane P. Chang, Department of Chemistry and Biochemistry, University of California, Los Angeles, for the opportunity to study in her group. Her guidance, valuable advices allowed me to progress in my understanding on plasma chemistry. I would like to deeply thank Nathan Marchack for collaborating and giving valuable advices. A big thanks to members of Prof. Chang's group, Dr. Ju Choi, Dr. James Dorman, Ms. Diana Chien, Ms. Ya-Chuan (Sandy) Perng, Mr. Han Chueh, Mr. Jack Chen, Mr. Calvin Pham, and Mr. Jea Cho. To whom it concerns with Japan Society for the Promotion of Science International Training Program, I am heartily grateful for having given me unforgettable opportunity to experience motivation for world-wide research area and constantly sufficient support. I believe that every experience that I have had in Prof. Chang's laboratory will help promote my study in future.

The author thanks sincerely Mr. Hiroki Kuroda, Mr. Kohei Asano, Mr. Toshiya Suzuki, and Mr. Yudai Miyawaki who aided their experimental works carried out in this thesis and also expressed their valuable suggestions and discussions.

A big thanks to my colleagues in Hori and Sekine's Lab, Dr. Saburo Uchida, Dr. Masahiro Iwasaki, Dr. Wakana Takeuchi, Dr. Chang Soon Moon, Dr. Shingo Kondo, Dr. Tsuyoshi Yamaguchi, Dr. Hirotoshi Inui, Mr. Eiji Takahashi, Mr. Hajime Sasaki, Mr. Lee Myung Ryong, Mr. Satoshi Kono, Mr. Shigetoshi Maruyama, Mr. Takuma Machino, Mr. Tomomi Obayashi, Ms. Emi Shibata, Mr. Masayoshi Kashihara,



## Acknowledgements

Mr. Kenichi Ando, Mr. Tetsuya Kimura, Mr. Hiroyuki Mikuni, Mr. Kota Mase, Mr. Yuto Matsudaira, Mr. Sho Kawashima, Mr. Tokushige Kino, Mr. Yoshihiro Itani, Mr. Arkadiusz Malinowski, Ms. Sachiko Iseki, Mr. Shang Chen, Mr. Hyung Jun Cho, Mr. Hitoshi Watanabe, Mr. Takuya Takeuchi, Mr. Yuske Abe, Mr. Lu Yi, Mr. Hironao Shimoeda, Mr. Koji Yasuda, Mr. Leyong Yu, Mr. Masanori Kato, Mr. Naoya Sumi, Mr. Tatsuya Hagino, Mr. Shinpei Amasaki, Mr. Takayuki Kanda, Mr. Yusuke Kondo Ms. Lu Ya, Mr. Minyoung Ahn, Mr. Jun Kuki, Mr. Ryosuke Kometani, Mr. Atsushi Fukushima, Mr. Takeyoshi Horibe, Mr. Tomohiro Takahashi, Mr. Jiadong Cao, Mr. Kuangda Sun for giving the big pleasure in life and creating a most enjoyable work atmosphere. I also appreciate the enough secretarial supports to Ms. Tomoko Yokoi, Ms. Megumi Oshigane, Ms. Azusa Ohta, Ms. Mitsuko Era, and Ms. Naoko Kataoka for helping to concentrate on the research without any problem of administrative task.

Finally, I'd like to dedicate this thesis to my parents, my brothers, my fiancé, and good friends.

*Hiroshi Yamamoto*

January 2012

## List of Papers

### 1. Original Papers

	<i>Title</i>	<i>Journal</i>	<i>Authors</i>
1	H <sub>2</sub> /N <sub>2</sub> plasma damage on porous dielectric SiOCH film evaluated by in situ film characterization and plasma diagnostics	Journal of Applied Physics, Vol. 109, 084112 (2011).	H. Yamamoto, K. Takeda, K. Ishikawa, M. Ito, M. Sekine, M. Hori, T. Kaminatsui, H. Hayashi, I. Sakai, T. Ohiwa (Chapter 4)
2	Feature Profiles on Plasma Etch of Organic Films by a Temporal Control of Radical Densities and Real-Time Monitoring of Substrate Temperature	Japanese Journal of Applied Physics, Vol. 51, 016202 (2011).	H. Yamamoto, H. Kuroda, K. Takeda, K. Ishikawa, M. Ito, M. Sekine, M. Hori (Chapter 3)
3	Chemical bond modification in porous SiOCH films by H <sub>2</sub> and H <sub>2</sub> /N <sub>2</sub> plasmas investigated by in situ infrared reflection absorption spectroscopy	Journal of Applied Physics, Vol. 110, 123301 (2011).	H. Yamamoto, K. Asano, K. Ishikawa, M. Sekine, H. Hayashi, I. Sakai, T. Ohiwa, K. Takeda, H. Kondo, M. Hori (Chapter 4)

## 2. International Conferences

<i>Title</i>	<i>Journal</i>	<i>Authors</i>
1 Behaviors of H and N radicals in 100 MHz capacitively coupled plasma using H <sub>2</sub> /N <sub>2</sub> mixture gases for the organic low dielectric constant film etching	The 20th Symposium on Plasma Science for Materials, Nagoya, June 21-22, pp.95 2007.	H. Yamamoto, S. Takashima, K. Takeda, R. Kawauchi, S. Takahashi, S. Den, M. Hori
2 Etching of organic low dielectric constant film in 100MHz capacitively coupled H <sub>2</sub> /N <sub>2</sub> gases plasmas	XXVIII International Conference on Phenomena in Ionized Gases, Prague, July 15-20, pp.813-816, 2007.	H. Yamamoto, S. Takashima, K. Takeda, R. Kawauchi, S. Takahashi, S. Den, M. Sekine, M. Hori
3 Control of Organic Low-k Etching in 100MHz Capacitively Coupled H <sub>2</sub> /N <sub>2</sub> Plasma Employing a Radical Sensor	29th International Symposium on Dry Process (DPS 2007), pp. 91-92, Tokyo International Exchange Center, Tokyo, November 13-14, 2007.	H. Yamamoto, S. Takashima, K. Takeda, R. Kawauchi, S. Takahashi, S. Den, M. Sekine, M. Hori
4 Evaluation of Plasma Ashing Damages on Porous SiOCH Films by Measurement of H and N Radical Densities	61st Annual Gaseous Electronics Conference, Marriott Dallas, Dallas, Texas, USA, p93, October 13-17, 2008.	H. Yamamoto, K. Takeda, M. Sekine, M. Hori

List of papers

5	Mechanism of Plasma Ashing Damages on Porous SiOCH Films	American Vacuum Society 55th International Symposium & Exhibition, Hynes Convention Center, Boston, MA, USA, October 19-24, PS-1-FrM3, 2008.	H. Yamamoto, K. Takeda, M. Sekine, M. Hori
6	Development of Quantitative Measuring Method for Damaged Layer on Porous SiOCH Film during H <sub>2</sub> /N <sub>2</sub> Plasma Ashing	The IUMRS International Conference in Asia 2008, Nagoya Congress Center Nagoya, December 9-13, p135, 2008.	H. Yamamoto, K. Takeda, M. Sekine, M. Hori
7	Control of plasma etching process based on real-time monitoring of substrate temperature	Memorial Symposium for the Retirement of Professor Tachibana (ISPC-19 Pre-Symposium in Japan), Kyoto University, Kyoto, Japan, May 30, 2009.	H. Kuroda, H. Yamamoto, M. Ito, T. Ohta, K. Takeda, M. Sekine, M. Hori
8	Plasma Damage Mechanism of Porous SiOCH Films Evaluated by In-situ Measurement System for Film Properties and Absolute Radical-Density	XXIX International Conference on Phenomena in Ionized Gases, PA13-8, p106, Convention Center, Cancun, Mexico July 12-17, 2009.	H. Yamamoto, K. Takeda, M. Sekine, M. Hori
9	In-situ Evaluation of H <sub>2</sub> Plasma Damage on Porous SiOCH Low- <i>k</i> Films	31th International Symposium on Dry Process (DPS2009), 4-2 p129-p130, BEXCO Convention Center, Busan, Korea, Sep. 24-25, 2009.	H. Yamamoto, K. Takeda, M. Sekine, M. Hori, T. Kaminatsui, K. Yamamoto, H. Hayashi, I. Sakai, T. Ohiwa

List of papers

10	Evaluation of Ashing Plasma Damages on Porous SiOCH Films Due to Ions, Radicals, and Radiation	AVS 56th International Symposium and Exhibition, PS-TuP7, p.104, San Jose McENERY CONVENTION CENTER, Nov. 8-13, San Jose, CA, 2009.	H. Yamamoto, K. Takeda, M. Sekine, M. Hori, T. Kaminatsui, K. Yamamoto, H. Hayashi, I. Sakai, T. Ohiwa
11	Effect of CF layer on porous SiOCH low- $k$ Films during H <sub>2</sub> or N <sub>2</sub> Plasma Exposure	2nd International Symposium on Advance Plasma Science and its Application (ISPlasma2010), PA029A, Meijo University, Nagoya Japan, Mar. 7-10, 2010.	H. Yamamoto, K. Takeda, M. Sekine, M. Hori
12	Study for Damage in Porous SiOCH Film with Air Exposure After H <sub>2</sub> or N <sub>2</sub> Plasma Treatment	2nd International Symposium on Advance Plasma Science and its Application (ISPlasma2010), PA026A, Meijo University, Nagoya Japan, Mar. 7-10, 2010.	T. Suzuki, H. Yamamoto, K. Takeda, M. Sekine, M. Hori
13	Measurement of Si Wafer Temperature with Metal Thin Film during Plasma Process Using Low-Coherence Interferometer	2nd International Symposium on Advance Plasma Science and its Application (ISPlasma2010), PA032A, Meijo University, Nagoya Japan, Mar. 7-10, 2010.	H. Kuroda, H. Sugiura, H. Yamamoto, M. Ito, T. Ohta, K. Takeda, H. Kondo, K. Ishikawa, M. Sekine, M. Hori

List of papers

14	Modification of Si-O-Si Structure in Porous SiOCH Films by O <sub>2</sub> plasma	The 11th International Workshop on Advanced Plasma Processing and Diagnostics, Ramada Jeju Hotel, Jeju, Korea, July 8-9, 2010.	H. Yamamoto, K. Takeda, K. Ishikawa, K. Kondo, M. Sekine, M. Hori
15	Modification of Si-O-Si Structure in Porous SiOCH Low- <i>k</i> Films with Ions, Radicals, and VUV Radiation in O <sub>2</sub> Plasma	63rd Annual Gaseous Electronics Conference and 7th International Conference on Reactive Plasmas, Paris, France, October 4-8, 2010.	H. Yamamoto, K. Asano, K. Takeda, K. Ishikawa, K. Kondo, M. Sekine, M. Hori
16	Mechanism of Modification in Si-O-Si Structure in Porous SiOCH Low- <i>k</i> Films by H <sub>2</sub> /N <sub>2</sub> plasma	AVS 57th International Symposium and Exhibition, Albuquerque CONVENTION CENTER, Albuquerque, U.S.A, Oct. 17-22, 2010.	H. Yamamoto, K. Takeda, K. Ishikawa, H. Kondo, M. Sekine, M. Hori, T. Imamura, H. Hayashi, I. Sakai, T. Ohiwa
17	Observation of 193-nm Photoresist Surface Exposed to Etching Plasma Employing C <sub>5</sub> HF <sub>7</sub> Gas Chemistry	International Symposium on Dry Process, Tokyo Institute of Technology, Tokyo, Nov.11-12, 2010.	H. Yamamoto, Y. Miyawaki, K. Takeda, K. Ishikawa, H. Kondo, M. Sekine, M. Hori, A. Ito, H. Matsumoto

## List of papers

18	In Situ Analysis of Plasma-Induced Modification on Porous SiOCH Films	2011SSDM, WINC AICHI, C-9-2, Sep. 27-30, 2011.	K. Asano, H. Yamamoto, Y. Miyawaki, K. Takeda, H. Kondo, K. Ishikawa, A. Yamazaki, A. Ito, H. Matsumoto, M. Sekine, M. Hori
19	In Situ Analysis of Plasma-Induced Modification on Porous SiOCH Films	2011SSDM, WINC AICHI, C-9-2, Sep. 27-30, 2011.	H. Yamamoto, K. Asano, K. Ishikawa, K. Takeda, H. Kondo, M. Sekine, M. Hori

### 3. Research Project

- International Training Program (Program for incubating young researchers on plasma nanotechnology materials and device processing, conducted by Japan Society for the Promotion of Science) in University of California, Los Angels, USA, from June to December, 2011.

### 4. Awards

- **JSAP encouraging prize**  
68th Fall Meeting 2007, Japan Society of Applied Physics, 6a-ZA-16, p.202, Hokkaido Institute of Technology, Japan, Sep. 4-8 2007.
- **DPS 2009 Award for the Young Researcher**  
31th International Symposium on Dry Process, 4-2 p129-p130, BEXCO Convention Center, Busan, Korea, Sep. 24-25, 2009.